学位論文

J/ψ production in p-Pb collisions at $\sqrt{s_{NN}} = 5.02$ TeV
(核子あたり重心系衝突エネルギー5.02 TeVでの陽子鉛衝突
におけるJ/ψ生成)

平成28年12月博士（理学）申請

東京大学大学院理学系研究科

物理学専攻　林　真一

J/ψ production in p-Pb collisions at $\sqrt{s_{NN}} = 5.02$ TeV

ShinIchi Hayashi

Dissertation for the Degree of Doctor of Science

Department of Physics
Graduate School of Science
University of Tokyo

Abstract

Quantum chromodynamics predicts quark deconfinement and the transition to strongly interacting matter, quark gluon plasma (QGP), at extremely high temperature and density. Since the dissociation of J/ψ in the QGP is expected due to Debye screening of color charges, suppression of the J/ψ yield is considered as one of the strong signatures of QGP formation.

Relativistic heavy ion collisions are a unique tool for studying the properties of the QGP. Strong suppression of the J/ψ yield was observed in Au–Au collisions at $\sqrt{s_{NN}} =$ 200 GeV by the PHENIX experiment in the Relativistic Heavy Ion Collider (RHIC) at Brookhaven National Laboratory. The J/ψ yields measured by the ALICE experiment at the Large Hadron Collider (LHC) in the European Organization for Nuclear Research (CERN) were also suppressed in Pb–Pb collisions at $\sqrt{s_{NN}} = 2.76$ TeV. In addition, non-negligible suppression of the J/ψ yield was observed in d–Au collisions at $\sqrt{s_{NN}} = 200$ GeV at RHIC. Suppression in d–Au collisions is thought as normal nuclear matter effects such as gluon shadowing and nuclear absorption. The understanding of normal nuclear matter effects in heavy ion collisions is essential in the discussion of the QGP effects.

This thesis presents the measurement of inclusive J/ψ production in p–Pb collisions at $\sqrt{s_{NN}} = 5.02$ TeV at the ALICE central barrel detector. The main aim of this analysis is to investigate the normal nuclear matter effects on J/ψ production in relativistic heavy ion collisions. Normal nuclear matter effects are expected to be relevant in heavy ion collisions at the LHC. The inclusive J/ψ nuclear modification factor ($R_{\rm pPb}$) at mid-rapidity ($-1.37 < y < 0.43$) was measured as a function of the transverse momentum $p_{\rm T}$. The results show significant suppression of the J/ψ yield around 1.5–4.5 GeV/c. The coherent parton energy loss model describes the dependence of the measured $R_{\rm pPb}$ on the rapidity y and $p_{\rm T}$. The y dependence of J/ψ $R_{\rm pPb}$ calculated by gluon shadowing models are similar to that of the measured $R_{\rm pPb}$.

The nuclear modification factor from normal nuclear matter effects in Pb–Pb collisions is approximated by the convolution of the nuclear modification factor in p–Pb collisions. In order to estimate the QGP effects in Pb–Pb collisions, the surviving fraction (S_{AA}) is introduced, which is the ratio between measured R_{AA} and expected R_{AA} by normal nuclear matter effects. The measured J/ψ S_{AA} is significantly less than unity at high $p_{\rm T}$. This result is consistent with the color screening effect in the QGP. At low $p_{\rm T}$ (< 4.5 GeV/c), clear enhancement of the J/ψ $S_{AA} > 1$ is observed. This enhancement suggests that a large amount of J/ψ is regenerated in the heavy ion collisions at LHC energies.

Contents

List of Figures

List of Tables

Chapter 1

Introduction

1.1 Quantum Chromodynamics (QCD)

Quantum Chromodynamics (QCD) is a local SU(3) gauge theory and describes the strong interaction of quarks and gluons. The Lagrangian of QCD is expressed by

$$L_{QCD} = \bar{\psi}_q^i (i\gamma^\mu (D_\mu)_{ij} - m_q \delta_{ij}) \psi_q^j - \frac{1}{4} F_{\mu\nu}^a F_a^{\mu\nu}, \tag{1.1}$$

where ψ_q^i is the quark field with color index i, γ^μ is a Dirac matrix, m_q is the quark mass. $F_{\mu\nu}^a$ is the gluon field strength tensor with gluon color index a. $(D_\mu)_{ij}$ is the covariant derivative of QCD expressed by

$$(D_\mu)_{ij} = \delta_{ij}\partial_\mu - i g_s t_{ij}^a A_\mu^a, \tag{1.2}$$

where g_s is the strong coupling constant, and A_μ^a is gluon field with gluon color index a. The strong running coupling constant $\alpha_s = g_s^2/4\pi$ can be expressed as a function of the momentum transfer (Q):

$$\alpha_s(Q^2) = \frac{12\pi}{(33 - 2n_f) ln(Q^2/\Lambda_{QCD}^2)}, \tag{1.3}$$

where n_f is the number of quark flavors, $\Lambda_{QCD} \sim 200$ MeV is the typical QCD scale. If $Q^2 >> \Lambda_{QCD}^2$ (short-range interaction), α_s becomes small. This feature is called ‘‘asymptotic freedom”. Figure 1.1 shows the α_s measurements as a function of Q [1].

1.2 Quark Gluon Plasma (QGP)

In QCD, quarks and gluons are confined in color-singlet hadrons at low energy (‘‘quark confinement”). Due to the asymptotic freedom, the coupling of QCD is expected to become weak at high temperatures. It is anticipated that the confinement may be broken in high density matters or at high temperatures and the phase transition to a deconfined state called quark-gluon plasma (QGP) occurs. It is thought that the phase transition to QGP in heavy ion collisions at the Large Hadron Collider (LHC) described in the next

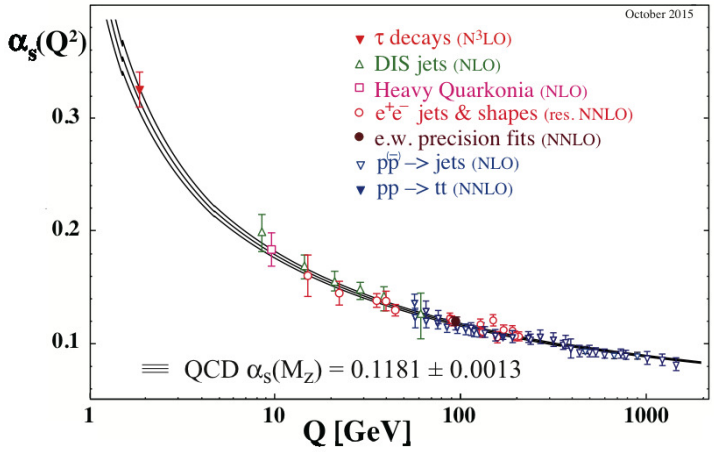

Figure 1.1: Summary of measurements of α_s as a function of the Q. The respective degree of QCD perturbation theory used in the extraction of α_s is indicated in brackets (NLO: next-to-leading order, NNLO: next-to-next-to leading order, NNLO: NNLO matched with resumed next-to-leading logs, N^{3}LO:next-to-NNLO) [1].

section is not a first order phase transition but a crossover where there is no clear separation of phases but the thermodynamic properties change gradually around the critical temperature T_c [2]. Figure 1.2 shows the results of the (2+1) lattice calculations on the pressure ($3p/T^4$), energy density(ϵ/T^4), and entropy density ($3s/4T^3$) as a function of temperature when the chemical potential μ is zero [3]. According to this calculation, T_c is expected to be 154 $\pm$ 9 MeV. Below T_c, the lattice QCD shows reasonable agreement to the hadron resonance gas model (HRG) which is assumed all hadrons or hadron resonance states contribute to the thermodynamics as non-interacting particles. Above T_c, the estimations of HRG lie along the lower edge of the lattice predictions and show discrepancies from the lattice calculation as the temperature rises. The results of the lattice calculation gradually reach the Stefan-Boltzmann limit. It implies that the interaction of gluons and quarks in the QGP still remains.

1.3 Relativistic Energy Heavy Ion Collisions

Relativistic heavy ion collisions are thought as a unique tool to create the QGP in the laboratory. For example, the initial energy density of Pb–Pb collisions at LHC calculated by the Bjorken formula is $\epsilon_0 \sim 20$ GeV/fm^3 which is much higher than the expected QGP threshold ϵ_c (~ 1 GeV/fm^3) [4]. Therefore it is believed that the QGP is created in relativistic heavy ion collisions.

The first experiment of the relativistic heavy ion collisions was performed at Bevalac in Lawrence Berkeley in the middle of 1970's. It was a fixed-target experiment with the energy per nucleon of 2 A GeV. In the 1980's, the experiments at the Alternating Gradient Synchrotron (AGS) in Brookhaven National Laboratory (BNL) and Super Proton Synchrotron (SPS) in European Organization for Nuclear Research (CERN) were started with the beam energy per nucleon of $\sim$ 14 A GeV and $\sim$ 160 A GeV, respectively. The

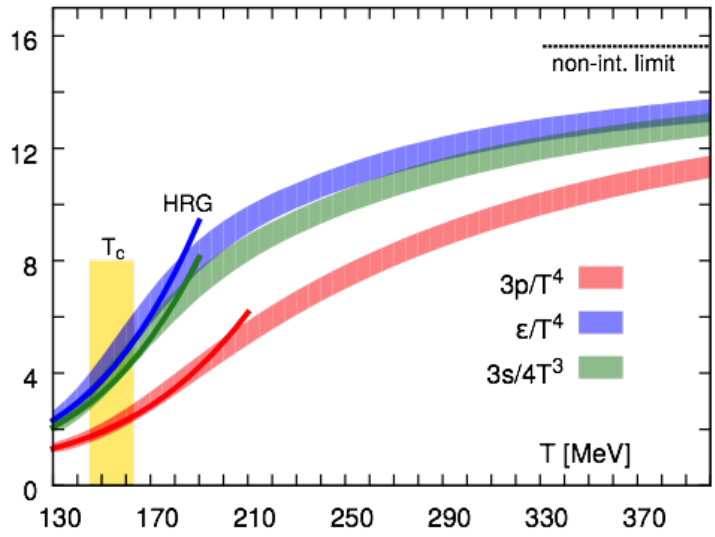

Figure 1.2: Calculated result of lattice QCD on the energy density, entropy density, and pressure as a function of temperature T [3].

Relativistic Heavy Ion Collider (RHIC) in BNL is the first collider for the relativistic heavy ion collisions. The Large Hadron Collider (LHC) in CERN provides heavy ion collisions since 2010.

Figure 1.3 shows a schematic view of the space-time evolution of heavy ion collisions [5]. It is necessary to understand the space-time evolution of heavy-ion collisions to study the QGP formation. The space-time evolution of heavy ion collisions can be separated into the initial stage, pre-equilibrium stage, equilibrium stage (QGP) and the QGP expansion, hadronic gas phase. It is assumed that the space-time evolution depends only on the proper time $\tau = \sqrt{t^2 - z^2}$ at high energy limit.

Initial Stage

When the nuclei collide at τ =0, a large number of nucleon-nucleon collisions occur in the overlap region of incident nuclei. It is non-trivial that heavy-ion collisions can be described by the superposition of nucleon-nucleon collisions due to the existence of normal nuclear effects as described in Chapter 2. The system is not thermalized at this points.

Pre-equilibrium stage

After initial collisions, a large amount of color flux tubes are generated between passing nuclei along the beam axis. This state is called "Glasma" [6]. Due to their instability, they decay into partons and the system reaches the local equilibrium at the formation time $\tau = \tau_0$. The exact τ_0 value is still unknown but it is estimated to be at least shorter than 1 fm/c [7].

Equilibrium stage (QGP) and expansion of the QGP

Once the system becomes thermalized, the expansion of the system can be described by relativistic hydrodynamics. The system cools down and if the temperature is around T_c, hadrons start to be created and the system is dominated by them.

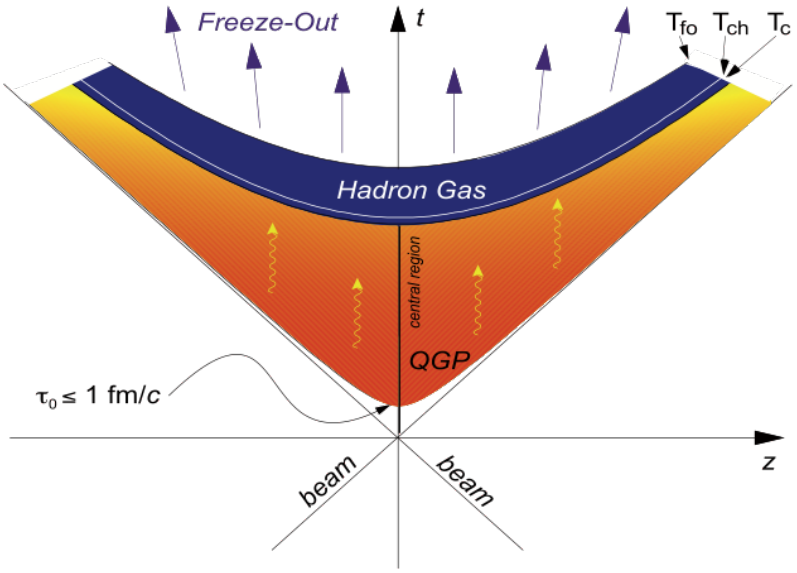

Figure 1.3: Space and time evolution in relativistic heavy ion collisions. The z-axis expresses the beam direction. τ_0 is the formation time of the QGP. T_c, T_{ch} ,and T_{fo} denote critical temperature, chemical freezeout temperature, and kinematical freezeout temperature, respectively [5].

Hadron gas phase

As the temperature of hadron gas decreases, the inelastic scattering of hadrons eventually ceases and the hadron yields become fixed. This temperature is called the chemical freezeout temperature T_{ch}. Finally the elastic scattering of hadrons ceases. This temperature is called the kinetic freezeout temperature T_{fo}, where the momentum distributions of hadrons are fixed..

The comparison between the experimental results and hydrodynamic calculations indicates that the system expands collectively with small shear viscosity to entropy density ratio (η/s) close to the lower bound $1/4\pi$ [7]. It implies that the partons in the QGP interact strongly and the mean free path is sufficiently short compared to the system size.

1.4 Objective and Organization of Thesis

J/ψ has been considered as one of the golden probes to discuss the formation of the QGP. As described in Chapter 2, attraction between c and $\bar{c}$ quarks is reduced by color Debye screening in the QGP and thus J/ψ is not formed in the QGP. In addition to the color screening effect in the QGP, normal nuclear matter effects such as gluon shadowing play a role to modify the J/ψ production in heavy ion collisions. Understanding of the normal nuclear matter effects is mandatory in understanding of the QGP effects to the J/ψ production in heavy-ion collisions. In this thesis, J/ψ production in p–Pb collisions at the LHC is measured and normal nuclear effects to the J/ψ production are discussed.

The organization of this thesis is as follows. In Chapter 2, the physical background related to this thesis is summarized. In Chapter 3, the LHC complex and the detector setup of the ALICE experiment is described. In Chapter 4, the analysis of $J/\psi \to e^+e^-$ in p–Pb collisions at $\sqrt{s_{NN}}$ =5.02 TeV is explained. In Chapter 5, experimental results and their interpretation are discussed. The conclusion of this thesis is then presented in Chapter 6.

1.5 Major Contributions

As one of the members in ALICE collaboration, the author carried out data taking of the ALICE experiment. In addition, the major contributions of the author are following.

- Installation, commissioning, and operation of the Transition Radiation Detector (TRD).

- Study of the trigger efficiency of the electron triggers with TRD in p–Pb collisions.

- Dielectron analysis in p–Pb collisions described in this thesis.

Chapter 2

Physical Background

2.1 J/ψ production process

J/ψ was discovered in p+Be$\rightarrow e^+e^-X$ at AGS and e^+e^- annihilation at SPEAR in Stanford Linear Accelerator Center (SLAC) in 1974 [9, 10]. J/ψ is a resonance state of $c\bar{c}$ and J/ψ mass is 3.0969 GeV/c^2 slightly higher than the charm quark pair mass. J/ψ has spin=1 without the orbital angular momentum.

Production of J/ψ can be classified into two processes. The first process is the creation of $c\bar{c}$ and the second is the formation of J/ψ from $c\bar{c}$ pairs. Since the mass of charm quarks is large enough compared to $\Lambda_{QCD} \sim 200$ MeV, $c\bar{c}$ production can be described by pertubative QCD calculations.

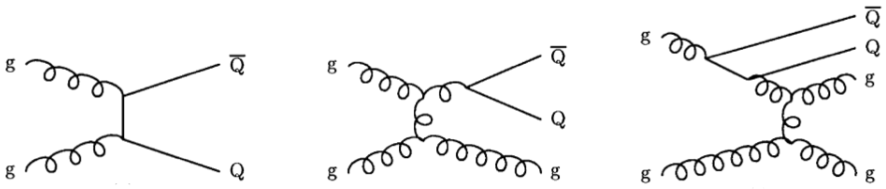

Figure 2.1: Feynman diagrams of $c\bar{c}$ production. From left to right, they express gluon fusion, gluon splitting, and flavor excitation, respectively.

Figure 2.1 shows Feynman diagrams of the main $c\bar{c}$ production at LHC energies [11]. The leading order process of $c\bar{c}$ production is gluon fusion. In this process, gluons from each nucleus interact and produce $c\bar{c}$. The next-leading order process is the gluon splitting, where scattered gluons split into $c\bar{c}$ pairs. Another next-leading order process is flavor excitation, where an off-shell quark produced by the virtual gluon splitting is scattered with a gluon in the other nucleus. Figure 2.2 shows the calculated cross section of $c\bar{c}$ production and the contribution of each process in pp collisions as a function of the collision energy [11].

Several models have been developed to describe J/ψ formation from $c\bar{c}$ pairs such as the color singlet model (CSM), color evaporation model (CEM), and Non-Relativistic QCD (NRQCD) [12–15]. However, for the moment, no model describes J/ψ production cross section as a function of the transverse momentum and polarization simultaneously.

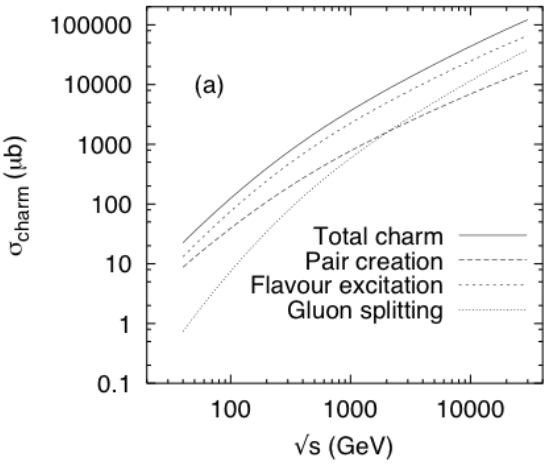

Figure 2.2: Total cross section of $c\bar{c}$ in pp collisions as a function of $\sqrt{s}$. The contribution from pair creation, flavor excitation, and gluon splitting are shown separately [11].

2.2 J/ψ production in Relativistic Heavy Ion Collisions

Compared to pp collisions, J/ψ undergoes the following effects in heavy ion collisions.

Color screening
When temperature in QGP is higher than the dissociation temperature, J/ψ is not formed since attraction between charm and anti-charm quarks are screened.

Regeneration in QGP or phase boundary
Since the number of $c\bar{c}$ at the RHIC and LHC energies is large in heavy ion collisions, J/ψ can be formed in QGP or phase boundary from uncorrelated $c\bar{c}$ (each of the pairs is produced in different nucleon-nucleon collisions.)

Modification of gluon PDF in nuclei
It is known that the gluon yield in nuclei is smaller than that in a free proton scaled by the atomic number at small Bjorken-x. This is called gluon shadowing. Therefore, simple atomic number A scaling of J/ψ production from pp collisions to heavy ion collisions is not preserved.

Cronin effect
It is known that the momentum spectra in p–A collisions become harder compared with that in pp collisions. This is called Cronin effect. This is due to the multiple scattering of incident partons in the nucleus.

Break up and energy loss in nuclei
J/ψ or pre-resonance $c\bar{c}$ state is destructed by the collisions with spectator nucleons, which suppresses the J/ψ production. This depends on the relative time scale of $c\bar{c}$ creation ($1/m_c$), J/ψ formation (0.3–1 fm/c) and crossing time of two colliding

nuclei. The charm quarks may interact in the nucleus and lose their energies, which changes the J/ψ yields.

Color screening is explained in Section 2.3. J/ψ regeneration is described in Section 2.4. The normal nuclear matter effects are summarized in Section 2.5.

2.3 Color Screening in QGP

Matsui and Satz proposed the suppression of J/ψ production as one of the strong evidence of the QGP formation [16]. The mechanism is based on the Debye screening observed in the electromagnetic plasma. At zero temperature, the QCD potential between the quark and anti-quark is expressed as

$$V_{QCD}(r) = -\frac{4}{3}\frac{\alpha_s(r)}{r} + \sigma r, \tag{2.1}$$

where r is the distance between the quark and anti-quark and σ is the QCD string tension, α_s is the gauge coupling constant of QCD described in Section 1.1.

Figure 2.3 shows the free energy of color singlet quark anti-quark pairs(F(r, T)) calculated by (2+1) lattice QCD [17]. The asymptotic value (F(∞, T)) corresponding to the energy needed to separate the quark anti-quark pair decreases with increasing temperature.

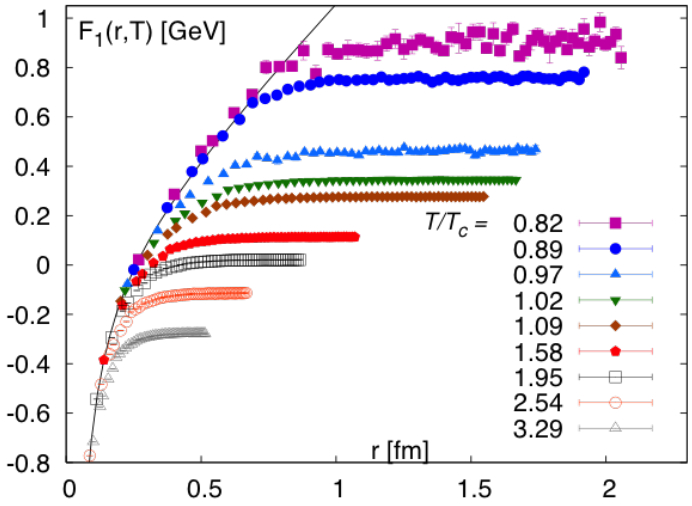

Figure 2.3: Color singlet quark-antiquark free energy as a function of quark separation calculated in (2+1) lattice QCD at different temperatures [17].

As the temperature increases, many free colored partons are generated and occupy the deconfined medium. The potential of the quark anti-quark pairs is modified from Coulomb-like potential to Yukawa potential:

$$V_{QCD}(r) = -\frac{4}{3}\frac{\alpha_s}{r}e^{-\frac{r}{\lambda_D(T)}}, \tag{2.2}$$

where $\lambda_D(T)$ is the Debye length of the color screening and becomes smaller as temperature increases. According to lattice calculations, the second term of Eq. 2.1 becomes smaller as temperature increases as below [18]:

$$\sigma/\sigma_0 = \sqrt{1 - \frac{T}{T_c}}, \tag{2.3}$$

where σ_0 is the string tension at $T = 0$. At the deconfined phase ($T > T_c$), the second term in Eq. 2.1 should become zero.

Lattice calculations and potential models have been adopted to estimate the dissociation temperature of each quarkonium. Due to the different binding energy, dissociation of quarkonium occurs sequentially towards high temperatures. Table 2.1 shows the summary of dissociation temperature T_d in units of T_c for each quarkonium calculated by the potential models [19].

State	J/ψ	$\chi_c(1P)$	$\psi(2S)$	$\Upsilon(1S)$	$\chi_b(1P)$	$\Upsilon(2S)$	$\chi_b(2P)$	$\Upsilon(3S)$
T_d/T_c	2.1	1.16	1.12	≥ 4.0	1.76	1.60	1.19	1.17

Table 2.1: Dissociation temperature in unit of T_c calculated using a potential model [19].

2.4 J/ψ Regeneration

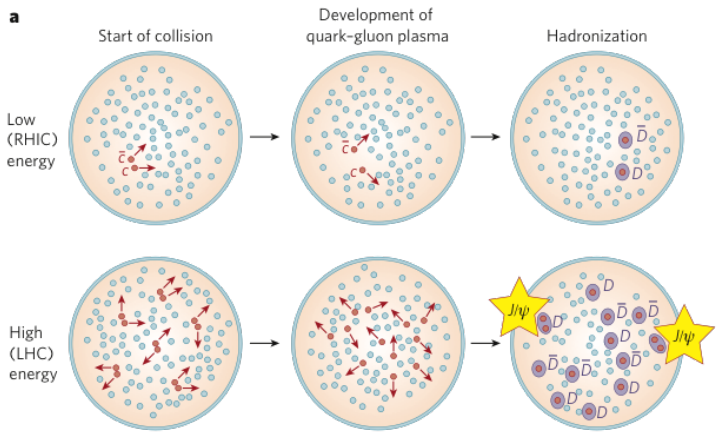

Figure 2.4: Schematics of J/ψ regeneration in heavy ion collisions at RHIC and LHC [20].

The expected number of $c\bar{c}$ quarks created in heavy ion collisions at the LHC, RHIC and SPS is about 60, 10, 0.2 as shown in Table 2.2, respectively. The yield of charmonium from regeneration depends on the ratio of the number of light quarks and charm quarks. Production of $c\bar{c}$ is scaled by the number of inelastic nucleon-nucleon collisions (N_{coll}) while production of light hadrons is scaled by the number of nucleons that exist in the overlap region of incident nuclei (N_{part}) in heavy ion collisions. Therefore, the estimated

Experiment	SPS	RHIC	LHC
$\int dN_{cc}/d\eta\ d\eta$	0.2	10	60
$dN_{ch}/d\eta$	450	650	1500

Table 2.2: Expected the number of $c\bar{c}$ and charged particles in central heavy ion collision at SPS, RHIC, and LHC.

number of regenerated J/ψ is scaled by (N_{coll}^2/N_{part}). The details of the collision geometry of high energy nucleus-nucleus collisions are summarized in Appendix A. Since N_{coll} grows faster than N_{part} as the impact parameter goes to zero (central collisions), regeneration of J/ψ is more pronounced in more central collisions. At the LHC, where abundant $c\bar{c}$ are created, J/ψ is possibly formed by the regeneration process from uncorrelated $c\bar{c}$ pairs, where c and $\bar{c}$ are created in different nucleon-nucleon collisions. Figure 2.5 shows the numerical calculation of $dN_{J/\psi}/dy$ as a function of N_{part} [21]. The rapid increase with N_{part} shows the quadratic dependence of the number of $c\bar{c}$ with N_{part}.

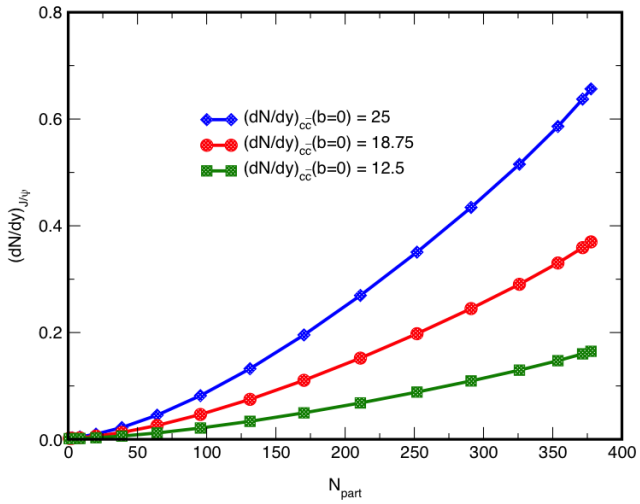

Figure 2.5: Calculation of regeneration model for J/ψ production as a function of N_{part} at LHC in three $c\bar{c}$ multiplicities [21].

2.5 Normal Nuclear Matter Effects in Relativistic Heavy Ion Collisions

2.5.1 Modification of Parton Distribution Function inside Nuclei

The cross section of the hard process between nucleon A and nucleon B is factorized as

$$\sigma_{AB} = \Sigma_{a,b} \int dx_1 \int dx_2 f^A(x_1) f^B(x_2) \sigma(a_1 + b_2), \tag{2.4}$$

where f^A and f^B are the parton distribution function (PDF). $\sigma(a_1+b_2)$ is the cross section of partonic subprocess between the partons in A and B. x is a longitudinal momentum fraction of partons. In 2→1 process, the relation of x, rapidity y, and energy is expressed by

$$x_{1,2} = \frac{m_T}{\sqrt{s}} e^{\pm y}. \tag{2.5}$$

In 2→2 process, the relation of x, rapidity, and energy is expressed by

$$x_1 = \frac{m_T}{\sqrt{s}}(e^{y_1} + e^{y_2}), \quad x_2 = \frac{m_T}{\sqrt{s}}(e^{-y_1} + e^{-y_2}), \tag{2.6}$$

where m_T is the transverse mass $m_T = \sqrt{m^2 + p_{\mathrm{T}}^2}$ and $\sqrt{s}$ is the collision energy per nucleon-nucleon collision in the center-of-mass system. PDF is mainly obtained from the results of deep inelastic scattering (DIS) and the calculated cross section using perturbative QCD as a function of x and momentum transfer Q^2 [22]. Figure 2.6 shows the

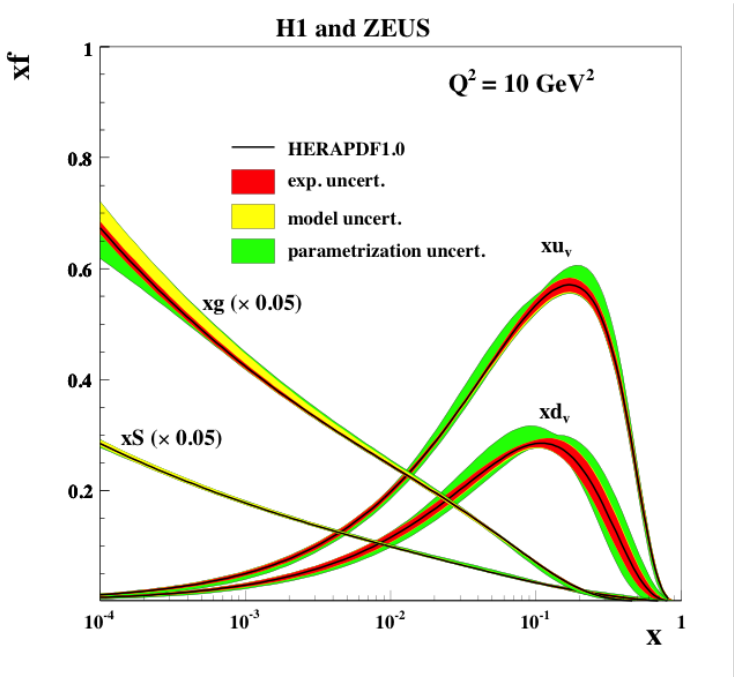

Figure 2.6: Parton distribution function measured via e-p scattering in H1 and ZEUS at HERA [23].

measured parton distribution function in protons via e–p scattering by H1 and ZEUS at HERA [23]. They observed the rapid growth of the gluon PDF toward small x. This multiple gluon production at small x is described by the BFKL equation [24].

European Muon Collaboration (EMC) group observed the modification of nuclear parton distribution function (nPDF) compared to PDF in the free proton in μ–Fe scattering in 1982 as shown in the left panel of Fig. 2.7 [30]. The right panel of Fig. 2.7 shows the ratio of the structure function in heavy nuclei and carbon. The suppression of F_2^A/F_2^C is seen toward smaller x. The nuclear modification factor of gluon PDF is introduced as

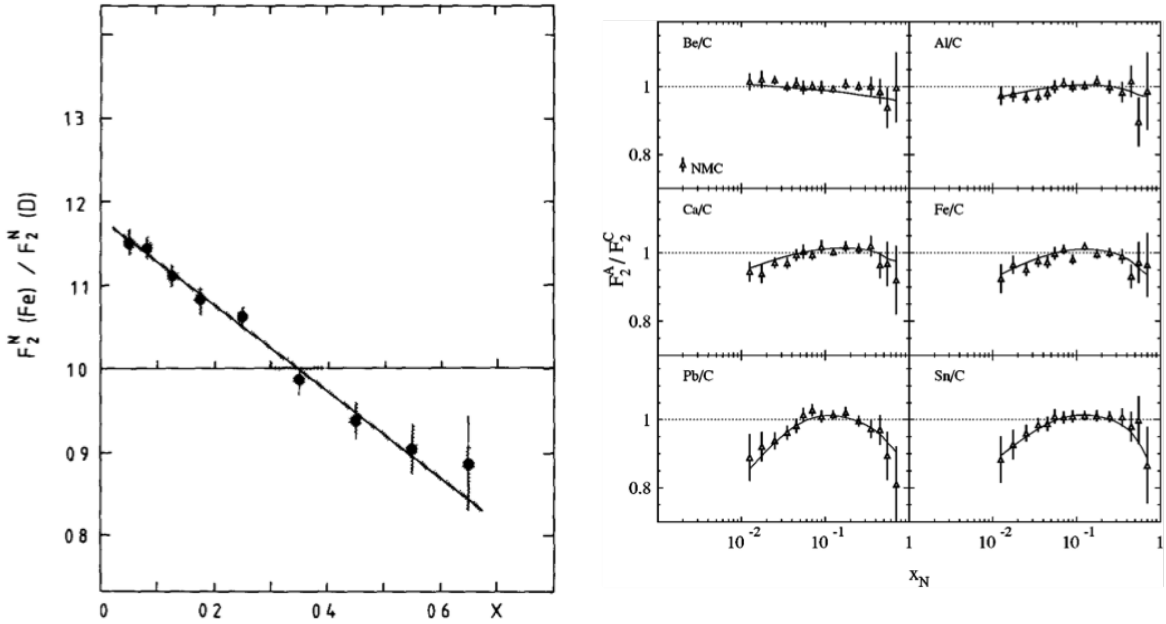

Figure 2.7: The ratio of the nucleon structure functions in iron and deuterium (Left) and heavy ions and carbon (Right) as a function of x measured by the EMC collaboration [30].

follows:

$$R_i^A(x,Q^2) = \frac{f_i^A(x,Q^2)}{Af_i^{free}(x,Q^2)}, \tag{2.7}$$

where A is the mass number of nuclei, f_i^{free} is the parton distribution function in the free proton. Figure 2.8 shows the comparison of model calculations of R_g for Pb at Q^2 =10 GeV^2. In Fig. 2.8, the region $x < 10^{-2}$ is called shadowing region where the nuclear modification factor is below 1. The region $10^{-2} < x < 0.3$ is called anti-shadowing region. The region above 0.3 is called EMC region. Figure 2.9 shows the x coverage of at the LHC, RHIC, and SPS in heavy ion collisions [83]. $c\bar{c}$ production at LHC corresponds to the order of $x \sim 10^{-4} - 10^{-3}$ [33, 83]. Therefore at the LHC energy, the gluon shadowing becomes relevant at mid-rapidity.

At further small x and small Q^2 region, gluon saturation is expected to occur [26]. As described previously in this section, gluon PDF rapidly increases at small x by gluon splitting ($g \to gg$). However, as gluon density increases, gluon fusion process ($gg \to g$) also becomes relevant and the gluon density becomes saturated. The transverse gluon density ρ is expressed by the number of gluons $xG(x,Q^2) \propto Ax^{-\lambda(Q^2)}$ divided by the transverse area πR_A^2. R_A is the atomic radius with atomic mass number A and is proportional to $A^{\frac{1}{3}}$. The cross section of gluon fusion is expressed by $\sigma_{gg\to g} \sim \alpha_s/Q^2$. Gluon saturation is expected to become relevant when the probability of $\rho\sigma_{gg\to g}$ is 1 [26]. The saturation scale Q_s is defined as the transverse momentum transfer at $\rho\sigma_{gg\to g}$ =1. Therefore, Q_s is proportional to $A^{\frac{1}{3}}x^{-\lambda}$. $\lambda \sim 0.3$ is suggested by the fits to the HERA data [27–29].

The Color-Glass-Condensate (CGC) framework is an effective field theory for the description of gluon saturation which divides the system into large x classical color field and associated small x quantum fields. Valence partons with large x act as static random

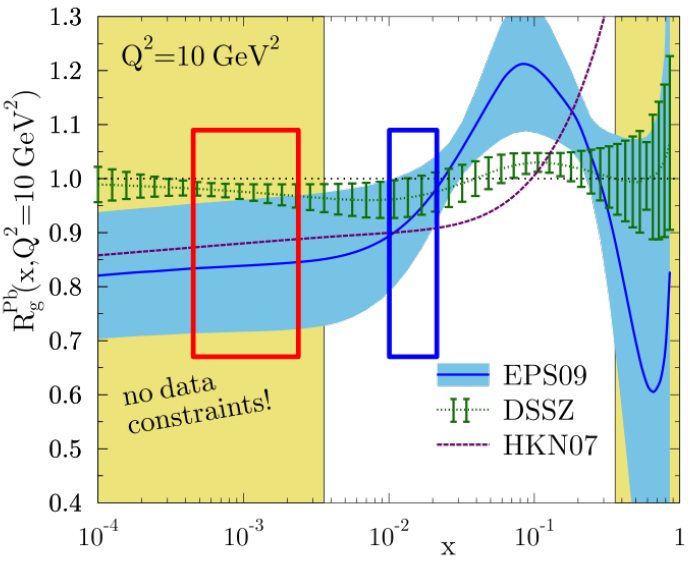

Figure 2.8: Comparison of the model calculation of the gluon nuclear modification factor inside Pb as a function of x at Q^2 =10 GeV^2 [32]. The red and blue solid squares show the x coverage of the mid-rapidity J/ψ measurements in ALICE at LHC ($|\eta| < 0.9$) and PHENIX at RHIC ($|\eta| < 0.35$), respectively.

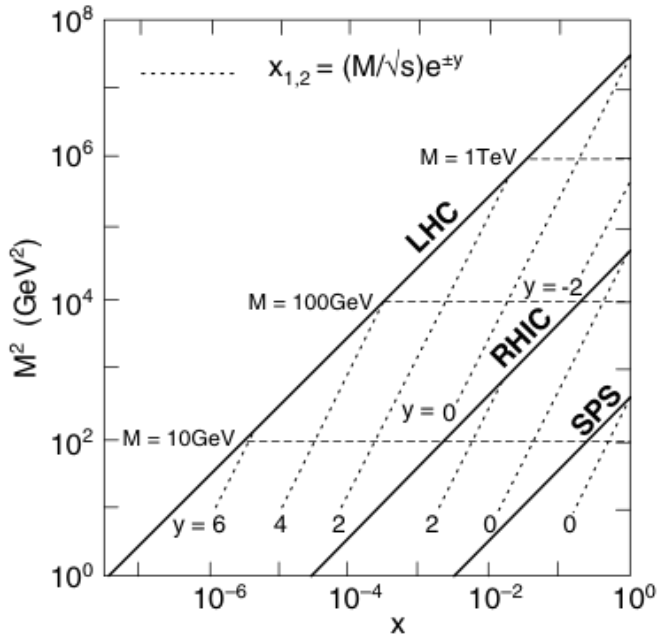

Figure 2.9: x and coverage of each experiment. The y-axis express transverse mass of the scattering processes [83].

color sources. Small x gluons are considered to be classical gauge fields induced by the valence partons and this situation obeys the Yang-Mills equation.

2.5.2 Cronin Effect and k_T Broadening

It is known that the particle yields at the moderate transverse momentum are enhanced in p–A collisions compared to pp collisions [38]. This is referred as the Cronin effect. This is due to the momentum broadening caused by the multiple rescattering of the partons in the target nucleus. The mean squared transverse momentum $\langle p_{\rm T}^2 \rangle$ depends on the production point:

$$\langle p_{\rm T}^2 \rangle_{pA}(b,z) = \langle k_T^2 \rangle_{pp} + \langle p_{\rm T}^2 \rangle \sigma_{gN} \int dz \rho_A(b,z). \tag{2.8}$$

Cronin effects can be approximated by the path length L:

$$\langle k_T^2 \rangle_{pA} = \langle k_T^2 \rangle_{pp} + a_{gN} L. \tag{2.9}$$

2.5.3 Partonic Energy Loss inside the Nucleus

Another initial state effect in heavy ion collisions is the initial state energy loss [40]. In the nuclear medium with the typical size $\sim L$, incoming partons interact with the partons in the target nucleus through the radiation of gluons. If the formation time of gluon radiation is shorter than the mean free path, the Cronin-like interaction mainly occurs and the radiation spectrum is similar to the Bethe-Heitler spectrum:

$$\omega \frac{dI}{d\omega} = \frac{N_c \alpha_s}{\pi} \{ ln(1 + \frac{\Delta q_{\rm T}^2 E^2}{M_{\rm T}^2 \omega^2}) - ln(1 + \frac{\Lambda_{QCD} E^2}{M_{\rm T}^2 \omega^2}) \}, \tag{2.10}$$

where E and $M_{\rm T}$ are the energy and transverse mass of the partons. $\Delta q_{\rm T}$ is momentum transfer and $\Delta q_{\rm T}^2 \sim \hat{q} L$ due to the momentum broadening in p–A collisions. $\hat{q}$ is called the transport coefficient. In the limit of $\Lambda_{QCD}^2 \ll \Delta q_{\rm T}^2 \ll M_{\rm T}^2$, the scaling of average energy loss $\Delta E \propto E$ is derived [41].

When the formation time is longer than the mean free path, the coherent energy loss known as the Landau-Pomeranchuk-Migdal (LPM) effect occurs. In QED, this effect suppresses medium induced bremsstrahlung radiation compared to the Bethe-Heitler process. The similar mechanism is expected in QCD process and the average energy loss is described by $\Delta E_{\rm LPM} \propto \alpha_s \hat{q} L^2$.

Furthermore, if the formation time is larger than path length L, the process is fully coherent and all scattering centers act as a source of radiation. The coherent energy loss is expressed by

$$\Delta E \propto \alpha_s N_c \frac{\sqrt{\hat{q} L}}{M_T} E \ \gg \Delta E_{\rm LPM}. \tag{2.11}$$

In case of J/ψ production, the color neutralization time of the color octet state ($\tau_{\rm octet} \ \sim 0.3$ – 1 fm/c) is expected to be larger than the perturbative time scale ($\tau_{\rm hard} \sim 1/M$). Figure 2.10 shows the quarkonium hadroproduction in the nucleus rest frame [42].

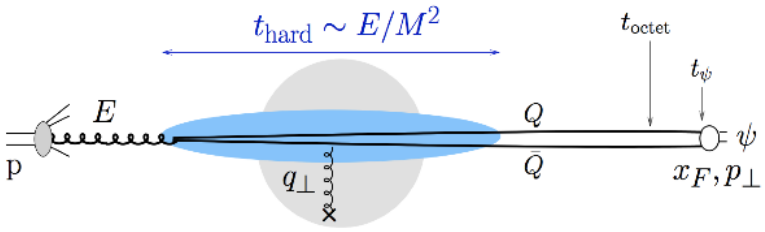

Figure 2.10: Schematic of view of quarkonium hadroproduction in the nucleus rest frame [42].

In the nucleus mass frame, quarkonium hadroproduction by $gg \to Q\bar{Q}$ looks like small angle scattering of an color charge. The hadronization time ($t_\psi \gtrsim t_{\rm octet} = \tau_{\rm octet}(E/M)$) is expected to be long enough and hadronization happens outside of the nucleus. In this situation, the medium induced coherent spectrum arises from the interference between the gluon emission in the initial and final states. The cross section of J/ψ production in p–A collisions can be written by

$$\frac{1}{A}\frac{d\sigma^{J/\psi}_{\rm pA}}{dE}(E,\sqrt{s}) = \int_0^E d\epsilon P(\epsilon)\frac{d\sigma^{J/\psi}_{pp}}{dE}(E+\epsilon,\sqrt{s}), \tag{2.12}$$

where $P(\epsilon)$ is quenching weight related to the induced gluon spectrum and it includes the transport coefficient $\hat{q}$. Figure 2.11 shows the initial energy loss calculation in p–Pb collisions at $\sqrt{s_{NN}} = 5$ TeV by F. Arleo *et al* [42]. The transport coefficient $\hat{q}$ is taken by

$$\hat{q}(x) = \frac{4\pi^2\alpha_s N_c}{N_c^2-1}\rho x G(x) \sim q_0(\frac{10^{-2}}{x})^{0.3}. \tag{2.13}$$

x dependence is considered from the HERA data described in Section 2.5.1. q_0 is the only free parameter in their calculation and $q_0 = 0.075$ GeV^2/fm is obtained from the fit to E866 p–W collision data [43]. If the modification of nPDF is not taken account, the energy loss suppresses the yield by a factor of 20% at mid-rapidity at LHC as shown in Fig 2.11.

2.5.4 Nuclear Absorption

J/ψ produced in initial parton scattering interacts with the nucleons in colliding nuclei. If the crossing time (τ_c) of $c\bar{c}$ in the target nuclei is longer than the formation time of quarkonia, quarkonia forms inside the nucleus and they interact with the nucleons. The crossing time τ_c of nucleus-nucleus collisions is calculated with

$$\tau_c = \frac{L}{(\beta_z\gamma)}, \tag{2.14}$$

where β_z is longitudinal velocity of $c\bar{c}$. If $\tau_c < \tau_f$, the effect does not play a key role as normal nuclear matter effects.

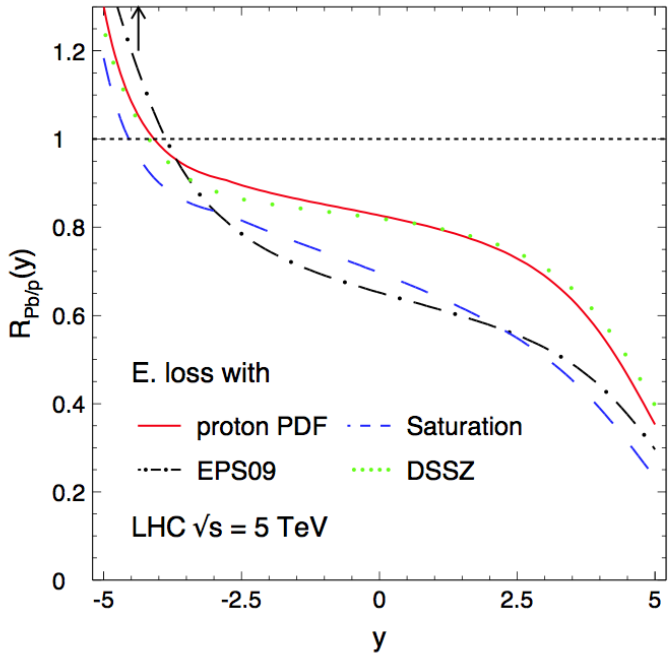

Figure 2.11: Prediction of J/ψ R_{pPb} in p–Pb collision at $\sqrt{s_{NN}} = 5$ TeV by the energy loss model calculation with 4 nPDF settings [40].

The number of J/ψ which interacts with the spectator nucleons is expressed by

$$L\rho_0\sigma_{abs}, \tag{2.15}$$

where L is the effective path length defined to be represented the number of nucleons that J/ψ interacts with through the target nuclei, ρ_0 is the normal nuclear density, and σ_{abs} is the absorption cross section. L in A-B collisions is calculated by Glauber models as follows with the impact parameter b:

$$L = \frac{1}{\rho_0}\frac{\int T_A(s)T_B(b-s)(A-1)T_A(s) + (B-1)T_B(b-s)ds}{\int T_A(s)T_B(b-s)ds}, \tag{2.16}$$

where $T_A(b)$ is expressed as the probability that a spectator nucleon in A exists on the path of J/ψ produced at b and the position along the beam direction z_A, $T_A(b) = \int_{z_A}^{\infty}\rho(b,z)dz$. The cross section of J/ψ in p-A collisions is expressed as

$$\sigma_{J/\psi,\mathrm{pA}} = \sigma_{J/\psi,pp}Ae^{-\rho_0 L\sigma_{abs}}. \tag{2.17}$$

Figure 2.12 shows the measured σ_{abs} as a function of collision energy [44]. As the collision energy increases, σ_{abs} decreases due to shorter crossing time.

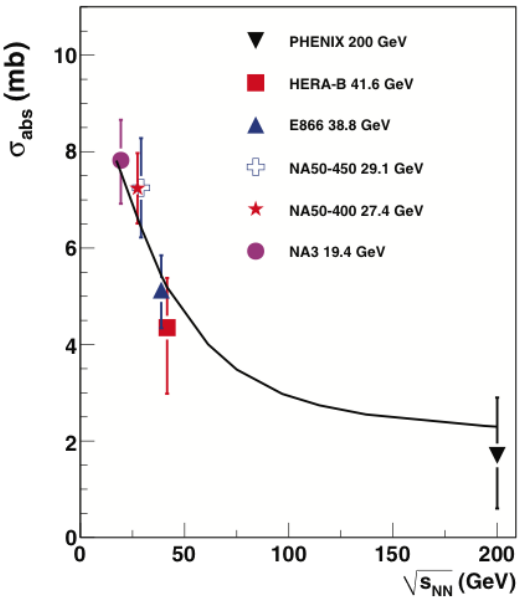

Figure 2.12: Measured σ_{abs} at $y = 0$ as a function of collision energy [44].

Experiment	System	$\sqrt{s_{NN}}$	Reference
NA38	p–Cu, U, W	19.4	[45–48]
	p–C, Al, Cu, W	29.1	[49]
	O–U, O-Cu, O-U,S-U	19.4	[50–54]
NA50	p–Be, Al, Cu, Ag, W	27.4	[55, 56]
	Pb–Pb	17.3	[57–63]
NA60	In–In	17.3	[64]

Table 2.3: The collision system and energy of charmonium experiments at SPS.

2.6 Previous Measurements of J/ψ Production in p(d)–A and A–A collisions

2.6.1 SPS Results

J/ψ has been measured at the Super Proton Synchrotron (SPS) in CERN in S-U, Pb–Pb, and In-In collisions at $\sqrt{s_{NN}}$ = 19.4, 17.3, and 17.3 GeV, respectively, as summarized in Table. 2.3.

The left panel of Fig. 2.13 shows the ratio of measured yields to the Drell-Yan process as a function of path length in p–A and A–A collisions at NA38, NA50, NA51. Drell-Yan yields are taken as the reference since the yields are scaled by N_{coll} [62]. p–A results show the common trend, which is understood as the normal nuclear matter effects. From this dependence, the nuclear absorption cross section σ_{abs} of J/ψ was determined to be $\sigma_{abs} = 4.2 \pm 0.5$ mb. The right panel of Fig. 2.13 shows the ratio of measured cross section

of J/ψ and the expected yield with the normal nuclear matter effects as a function of path length L in Pb–Pb collisions at $\sqrt{s_{NN}}$ = 17.3 and 19.4 GeV at NA38, and NA50, respectively [63]. The results show the clear suppression of the J/ψ yields in heavy ion collisions at large L. The suppression is more pronounced for the weakly-bound state ψ‘. Figure 2.14 shows the ratio of measured yield to the expected yield in In-In collisions at

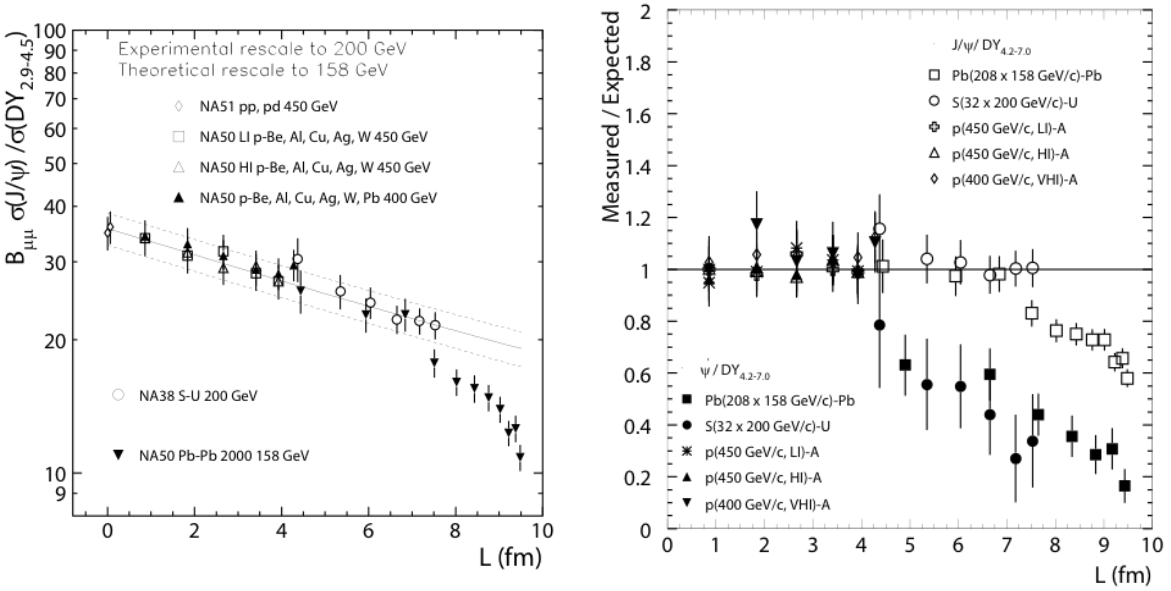

Figure 2.13: The ratio of the measured J/ψ yields to Drell-Yan process as a function of path length in p–A and A–A collisions at NA38, NA50 and NA51 (Left) and the ratio of the measured yields to the expected yields of J/ψ and $\psi^{'}$ as a function of path length in A-A collisions at NA38, NA50 and NA5 [62, 63].

NA60 and Pb–Pb collisions at NA50 at $\sqrt{s_{NN}}$ = 17.3 GeV as a function of N_{part} [64]. In large N_{part} (central) events, significant suppression is observed in both Pb–Pb and In-In collisions above $N_{part} > 80$.

Figure 2.15 shows the path length dependence of mean squared transverse momentum $\langle p_{\mathrm{T}}^2 \rangle$ [60]. $\langle p_{\mathrm{T}}^2 \rangle$ increases with mass number A which is understood as the Cronin effect. The results are fitted using the Cronin parametrization and a_{gN} =0.081 ± 0.004 and 0.078 ± 0.006 at $\sqrt{s_{NN}}$ = 17.3 and 19.4 GeV, respectively.

2.6.2 E866 at Tevatron

E866 at Tevatron in Felmi National Accelerator Laboratory (FNAL) has a wide Feynman-x coverage at $-0.1 < x_F < 0.93$. Feynman-x is defined as the longitudinal momentum transfer fraction x_1 and x_2 in the projectile and the target, respectively:

$$x_F = x_1 - x_2. \tag{2.18}$$

E866 evaluates the nuclear matter effects with parameter α defined as

$$\sigma_{AB}^{J/\psi} = \sigma_{NN}^{J/\psi}(AB)^{\alpha}, \tag{2.19}$$

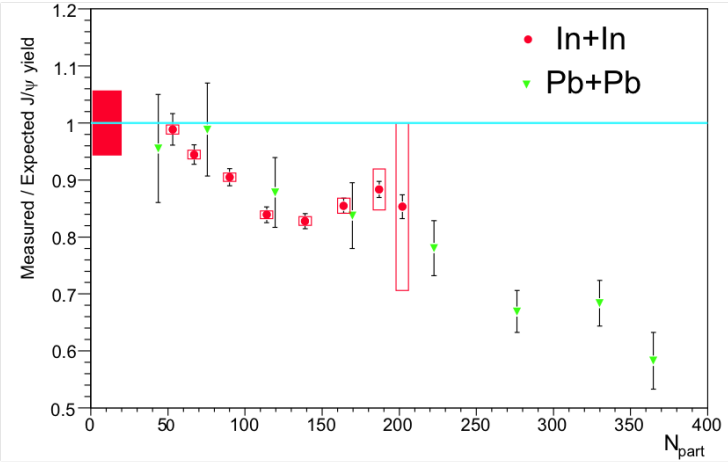

Figure 2.14: The ratio of the measured yields to expected yields from the normal nuclear matter effects as a function of N_{part} in Pb–Pb and In-In collisions [64].

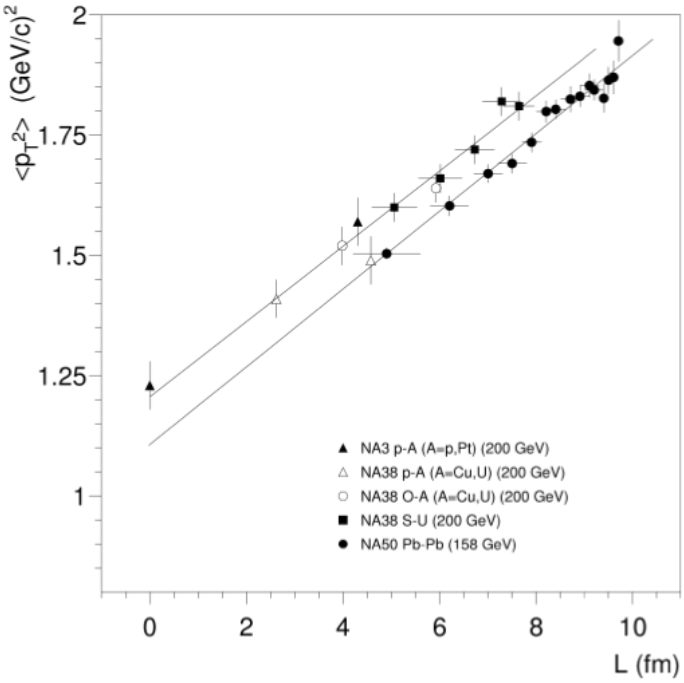

Figure 2.15: The mean squared transverse momentum $\langle p_{\mathrm{T}}^2 \rangle$ of J/ψ in p-A and A-A collisions [60].

where A and B are the mass number of colliding nuclei. $\sigma_{AB}^{J/\psi}$ is the J/ψ cross section in A–B collisions and $\sigma_{NN}^{J/\psi}$ is the J/ψ cross section in nucleon-nucleon collisions. Figure 2.16 shows the measured α as a function of x_F in p–A (p–Fe, p–W) collisions at $\sqrt{s_{NN}} = 38.8$ GeV. E866 observed J/ψ suppression at large x_F region in p–Fe and p–W collisions at

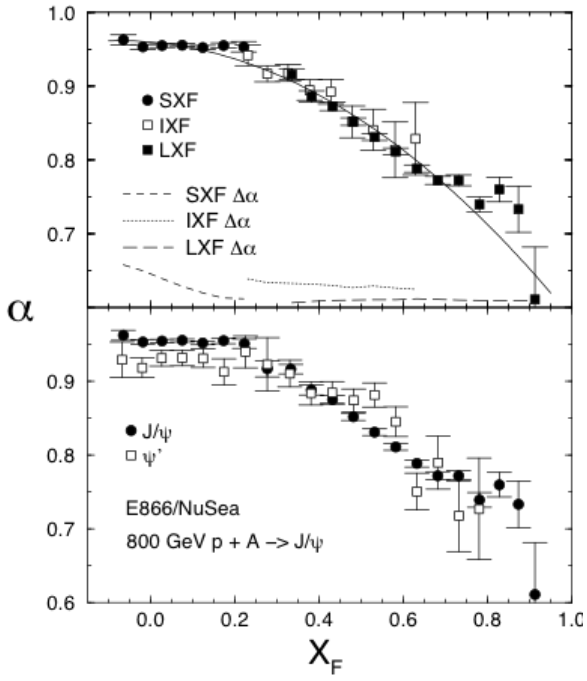

Figure 2.16: x_F dependence of α on J/ψ production for three different data sets (Top) and x_F and comparison between J/ψ and ψ (Bottom) at $\sqrt{s_{NN}}$ = 38.8 GeV [43].

$\sqrt{s_{NN}}$ = 38.8 GeV, while α is 0.96 ± 0.01 at low x_F. This suppression at large x_F might be described by the coherent energy loss in the nucleus [40].

2.6.3 RHIC

d–Au Collisions

The left panel of Fig. 2.17 shows the comparison of the nuclear modification factor $R_{\rm dAu}$ of the J/ψ production between the measured results and the calculations based on nuclear shadowing and gluon saturation at $\sqrt{s_{NN}}$ =200 GeV [69]. $R_{\rm dAu}$ is defined as

$$R_{\rm dAu} = \frac{Y_{\rm dAu}}{\langle N_{coll}\rangle Y_{pp}}, \tag{2.20}$$

where $Y_{\rm dAu}$ and $Y_{\rm pp}$ are the J/ψ yields in d–Au and pp collisions, respectively. The results show the suppression of J/ψ production in the whole measured rapidity region. A shadowing+nuclear absorption model describes y dependence. The right panel of Fig. 2.17 shows the comparison of J/ψ $R_{\rm dAu}$ between experimental data from RHIC and the energy loss model calculation with various nPDF assumptions in d–Au collision at $\sqrt{s_{NN}}$ =200 GeV [42]. Within the uncertainty of nPDF, the energy loss model shows reasonable agreement at mid-rapidity and forward rapidity.

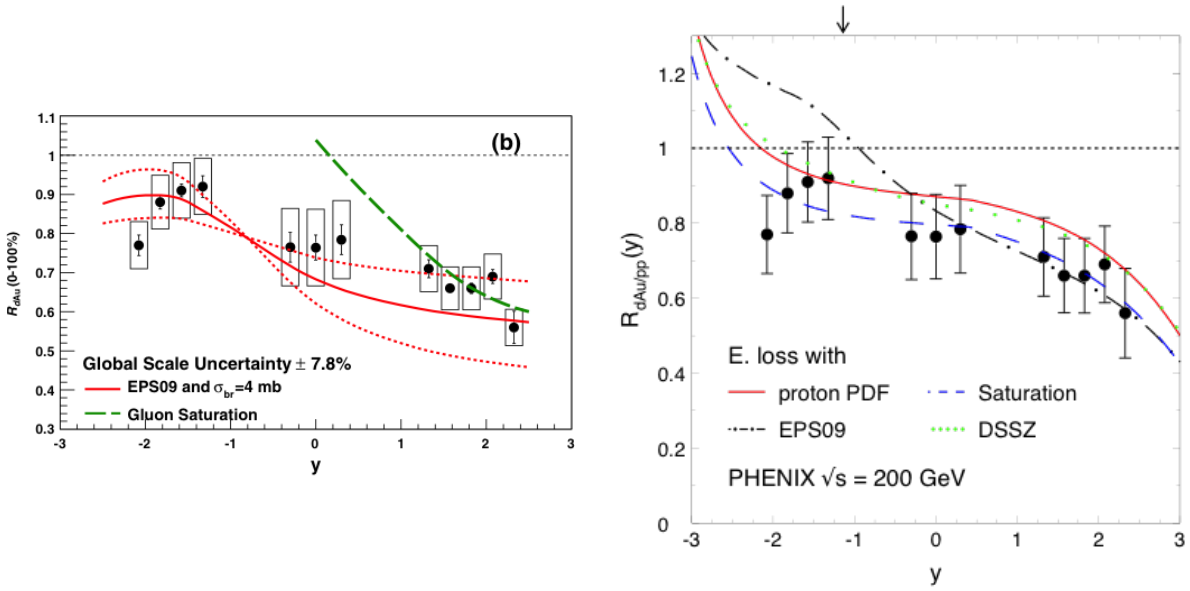

Figure 2.17: J/ψ production in d–Au at $\sqrt{s_{NN}}$ =200 GeV/c measured by PHENIX at RHIC and model comparison with the NLO calculation with EPS09 nPDF and gluon saturation model (Left). Comparison of J/ψ production between experimental data from RHIC and that from the energy loss model calculation with various nPDF assumptions in d–Au collisions at $\sqrt{s_{NN}}$ =200 GeV (Right) [69, 70].

Heavy Ion collisions

Figure 2.18 shows the nuclear modification factor of J/ψ at mid-rapidity and forward rapidity in Au–Au collisions at $\sqrt{s_{NN}}$ =200 GeV [71]. The nuclear modification factor in A-A collisions (R_{AA}) is defined as

$$R_{AA} = \frac{Y_{\mathrm{AA}}}{\langle N_{coll} \rangle Y_{pp}}, \tag{2.21}$$

where Y_{AA} and Y_{pp} are the J/ψ yields in A-A and pp collisions, respectively. The results show the strong suppression of J/ψ in Au–Au collisions at both mid-rapidity and forward rapidity. The lower panel of Fig. 2.18 shows the ratio of forward/mid nuclear modification factor. At N_{part} >100, the J/ψ production at forward rapidity shows stronger suppression than that at mid-rapidity in Au–Au collisions. The measured R_{AA} is affected not only QGP effects but also by non-negligible normal nuclear matter effects. One of the possible explanation for the stronger suppression at forward rapidity is due to the stronger normal nuclear matter effects.

In order to estimate the contribution of the normal nuclear matter effects in J/ψ R_{AA}, d–Au data is used [73, 74]. The rapidity dependent absorption cross section $\sigma_{abs}^{J/\psi}$ is extracted by fitting with EKS98 and nDSg shadowing models as shown in the left panel of Fig. 2.19 [74]. Since there is a significant difference between the impact parameter dependence of R_{pAu} and R_{dAu} mainly due to the smearing caused by the finite size of the deuteron, R_{pAu} is calculated using EKS98 and nDSg shadowing parametrization obtained

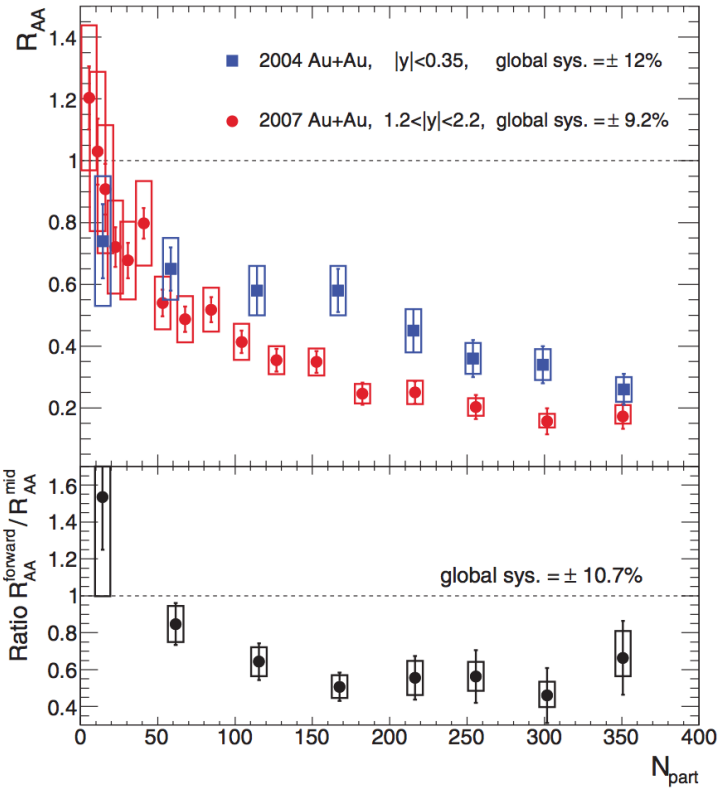

Figure 2.18: N_{part} dependence of the nuclear modification factor of J/ψ at mid-rapidity and forward rapidity (Upper) and the ratio of the nuclear modification factor of J/ψ between forward rapidity and mid-rapidity [71].

from $R_{\rm dAu}$ [75].

R_{AA} from normal nuclear matter effects ($R_{AA,\rm init}$) is estimated by the Glauber calculation of Au–Au collisisions using the rapidity dependent absorption cross sections and the centrality dependent $R_{\rm pAu}$. For each nucleon-nucleon collisions, impact parameter b_1 and b_2 are determined with respect to each target nucleus and then $R_{\rm pAu}(b_1, y) \times R_{\rm pAu}(b_2, -y)$ is calculated. After processing all events, $R_{AA,\rm init}$ is obtained with the number of generated events N_{ev},

$$R_{AA,\rm init} = \frac{\sum_{i=0}^{N_{ev}} R_{\rm pAu}(b_1, y) \times R_{\rm pAu}(b_2, -y)}{N_{ev}} \tag{2.22}$$

The right panel of Fig. 2.19 shows the estimated normal nuclear matter R_{AA} in Au–Au collisions at $\sqrt{s_{NN}} = 200$ GeV.

Figure 2.20 shows S_{AA} which is defined by R_{AA} divided by the normal nuclear matter R_{AA} as a function of the initial energy density ϵ_0 and the formation time τ_0 for RHIC and SPS data [72]. After consideration of the normal nuclear matter effects, the results of both forward rapidity and mid-rapidity show the same monotonic suppression as a function of $\epsilon\tau$. Furthermore hydro+J/ψ model calculation describes the PHENIX data well with the J/ψ melting temperature= $2T_c$ as shown in the left panel of Fig. 2.21 [76]. The understanding and determination of the normal nuclear matter from the measured

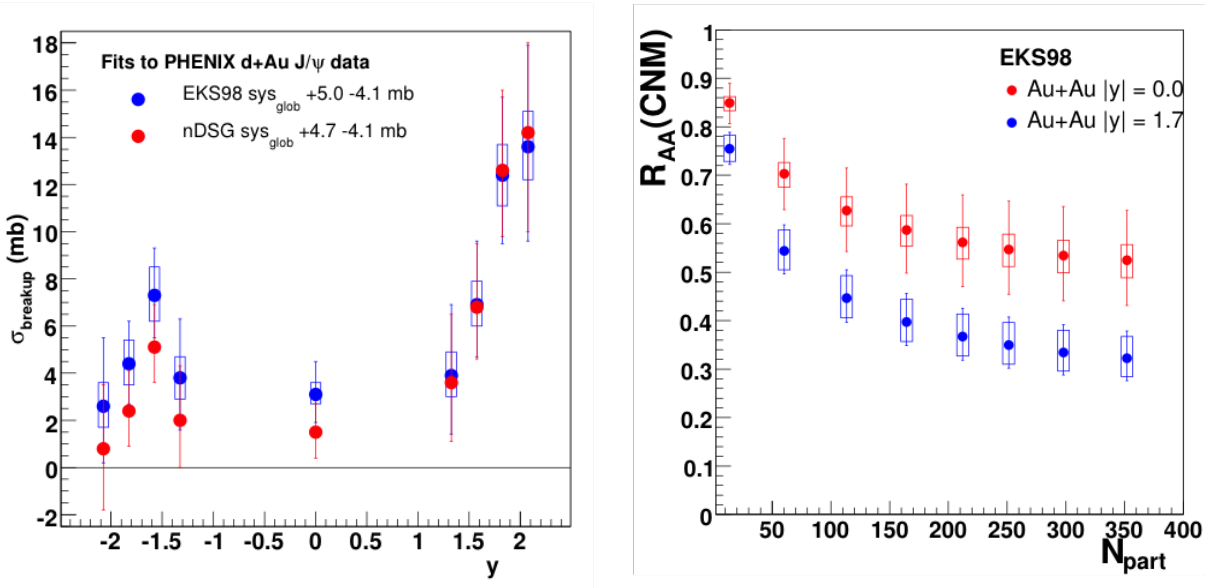

Figure 2.19: Rapidity dependent absorption cross section in d–Au collisions at $\sqrt{s_{NN}}$ =200 GeV(Left) and normal nuclear matter R_{AA} in Au–Au collisions estimated from d–Au data at $\sqrt{s_{NN}}$ =200 GeV with EKS98 parametrization (Right) [74].

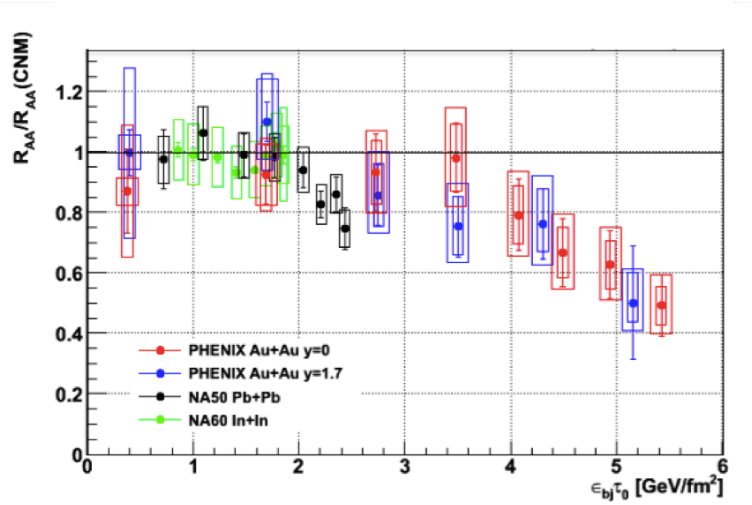

Figure 2.20: J/ψ S_{AA}) of RHIC and SPS data as a function of $\tau_0\epsilon_0$ [72].

d–Au results allow this quantitative model comparison.

2.6.4 LHC measurements

Since the collision energy of LHC is higher than RHIC, stronger suppression due to the color screening is expected. Figures 2.22 show the measured J/ψ R_{AA} as a function of the charged particle multiplicity at mid-rapidity and forward rapidity at RHIC and LHC [81]. Less suppression at LHC was observed at both mid-rapidity and forward rapidity. The

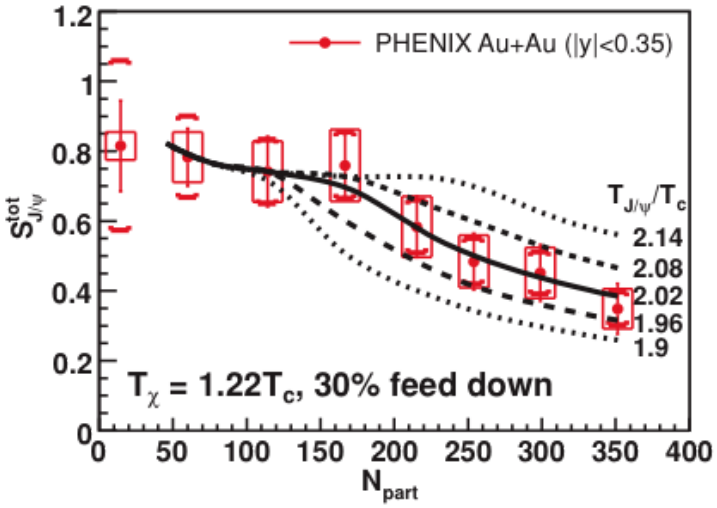

Figure 2.21: Comparison of the J/ψ S_{AA} and the hydrodynamic calculation including the melting effects of quarkonium in Au–Au collisions at RHIC [76].

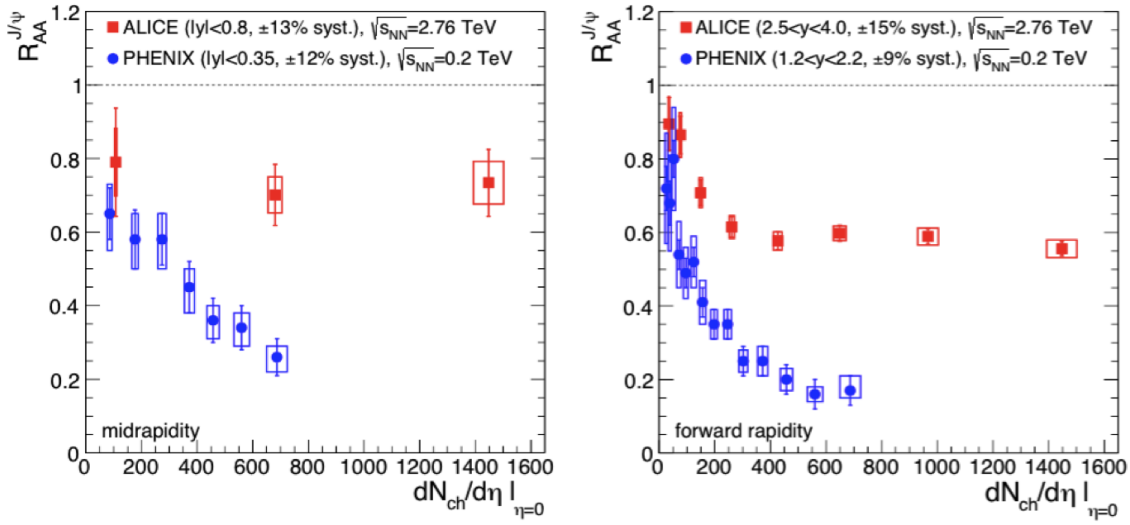

Figure 2.22: J/ψ R_{AA} as a function of the charged particle multiplicity at mid-rapidity (Left) and forward rapidity (Right) in Pb–Pb collisions at $\sqrt{s_{NN}}$ = 2.76 TeV and Au–Au $\sqrt{s_{NN}}$ = 200 GeV [81].

investigation of the normal nuclear matter effects at LHC is crucial in understanding the less suppression at the LHC energy.

Figure 2.23 shows the measured J/ψ R_{AA} as a function of $p_{\rm T}$ at mid-rapidity and forward rapidity at RHIC and LHC [78,79]. At higher $p_{\rm T}$, R_{AA} is compatible to the RHIC result. On the other hand, a large enhancement is observed above 4 GeV/c. The J/ψ regeneration picture gives a reasonable explanation to this enhancement. The transport model calculation, which considers all collision stages including both color screening and J/ψ regeneration, is in agreement with the ALICE result. To quantify the effects from

regeneration, the normal nuclear matter at the LHC energy have to be understood.

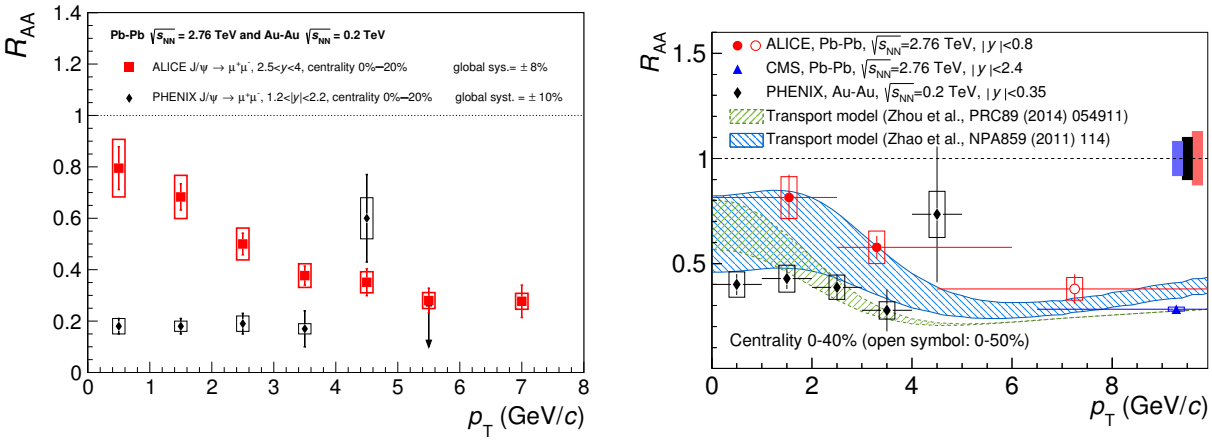

Figure 2.23: J/ψ R_{AA} as a function of the charged particle multiplicity at mid-rapidity (Left) and forward rapidity (Right) in Pb–Pb collisions at $\sqrt{s_{NN}}$ = 2.76 TeV and Au–Au $\sqrt{s_{NN}}$ = 200 GeV [78, 79].

2.7 Normal Nuclear Matter Effects at LHC

Due to the large γ factor at LHC, the crossing time of $c\bar{c}$ in the nuclear matter is expected to be $\sim 10^{-2}$ fm/c and this is much shorter than the $c\bar{c}$ formation time. Therefore the nuclear absorption might be small or negligible at LHC energy. Modification of the nPDF is expected to be more crucial compared to the RHIC measurements since the LHC measurements cover small x regions (10^{-4}–10^{-3}). Gluon saturation is expected to be seen at forward rapidity. Cronin effect is also expected to seen in the LHC measurements. The model calculation of the initial state energy loss in the nucleus predicts 20% suppression of the J/ψ yield in p–Pb collisions.

In order to understand the normal nuclear matter effects at LHC energy, the experimental studies of J/ψ production in p–Pb collisions are crucial. The motivation of this thesis is the investigation of normal nuclear matter effects in p–Pb collisions. To discuss normal nuclear matter effects, the nuclear modification factor is introduced as

$$R_{\rm pPb} = \frac{Y_{\rm pPb}}{\langle N_{coll} \rangle Y_{\rm pp}}, \tag{2.23}$$

where $\langle N_{coll} \rangle$ is the average number of binary nucleon-nucleon collisions in p–A and A–A collisions and $Y_{\rm pPb}$ and $Y_{\rm pp}$ are yields of J/ψ in p–Pb and pp collisions, respectively. Deviation from unity of $R_{\rm pPb}$ implies the existence of nuclear matter effects. The normal nuclear matter effects described in this chapter are sensitive to x, Q, and path length. Therefore the systematic measurements such as collision energy, rapidity y, $p_{\rm T}$, and the impact parameter dependence provide key information to understand the nuclear matter effects in p–A and A–A collisions.

Chapter 3

Experimental Setup

The data analyzed in this thesis is p–Pb collisions at $\sqrt{s_{NN}} = 5.02$ TeV at the Large Hadron Collider (LHC) collected with the ALICE detectors in 2013. LHC is a high energy hadron collider for pp, p–Pb, and Pb–Pb collisions located at CERN.

In this chapter, the experimental setup for the J/ψ measurement is explained. Most of the parts of the detector performance is summarized in the ALICE Physics Report I, II and Performance of the ALICE Experiment at the CERN LHC [33, 83, 84].

3.1 The Large Hadron Collider (LHC)

LHC is currently the largest particle accelerator in the world. It is located around the border between Switzerland and France and its circumstance is 27 km. This tunnel was used for the Large Electron-Positron Collider (LEP). LHC can accelerate various hadrons with 16 radio-frequency (RF) accelerating cavities and over 1600 superconducting magnets. LHC accelerates protons and lead ions up to 7 TeV and 2.75 TeV/nucleon, respectively.

LHC hosts the four main experiments, ATLAS, CMS, LHCb, and ALICE. These experiments focus on various aims of high energy particle and nuclear physics. ATLAS, CMS, and ALICE collected the data of p–Pb and Pb–Pb collisions during Run1 (2009 - 2013) and provide various insights into the QGP physics. LHCb took p–Pb collision data in 2013 and has a plan to collect heavy ion collision data from Run2 (2016-).

Figure 3.1 shows the schematics view of the CERN accelerator complex [85]. Protons are accelerated by a linear accelerator LINAC2. Before injected into the Proton Synchrotron (PS), the booster accelerates them up to 1.4 GeV. They are sent to PS and the Super Proton Synchrotron (SPS) sequentially and accelerated up to 450 GeV. Then they are transferred to LHC and accelerated up to 7 TeV. Lead ions are generated by heating a highly purified lead sample up to around 550°C. At this stage, Pb^{27+} is dominantly generated. They are accelerated via LINAC3 and passed through the carbon foil which strips them to Pb^{+54}. They are also accelerated via Low Energy Ion Ring (LEIR) before injected into PS up to 72 MeV per nucleon. PS accelerate them to 5.9 GeV per nucleon and they are transferred into the foil again and fully stripped. These fully stripped ions are accelerated at SPS up to 177 GeV and sent to the LHC rings. Lead ions are further accelerated and delivered to the interaction points of the four main experiments. During

Run1, pp collisions at $\sqrt{s}$ = 900 GeV, 2.76 TeV, 7 TeV, and 8 TeV, p–Pb collisions at $\sqrt{s_{NN}}$ = 5.02 TeV and Pb–Pb collisions at $\sqrt{s_{NN}}$ = 2.76 GeV were provided by LHC.

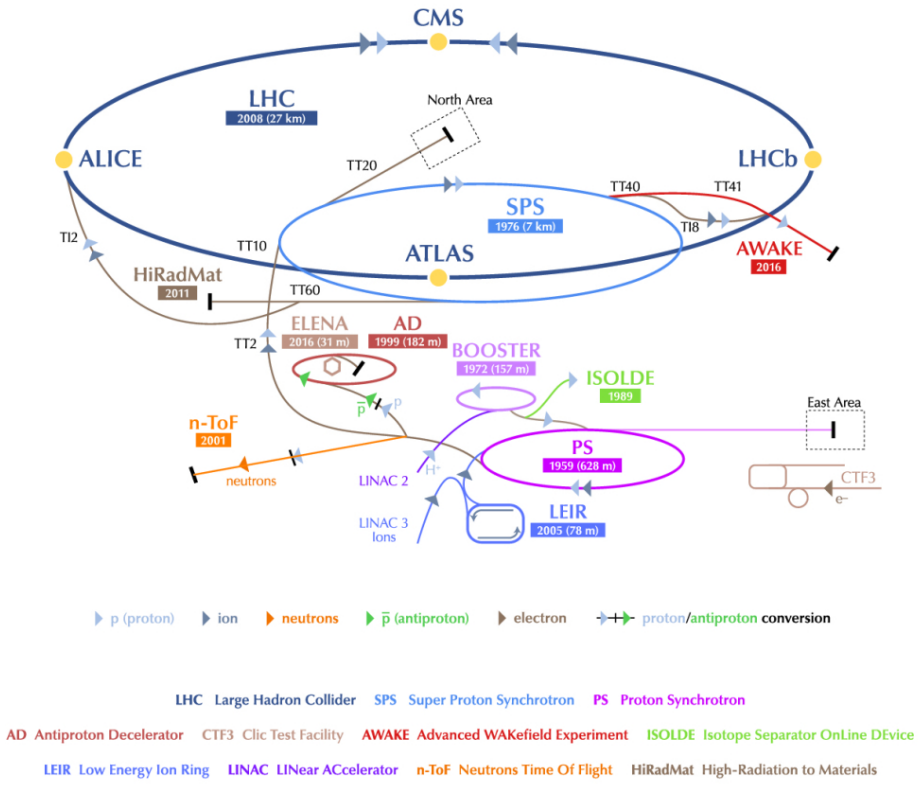

Figure 3.1: Schematics of the CERN accelerator complex [85].

3.2 Overview of the ALICE Detectors

A Large Ion Collider Experiment (ALICE) is one of the major experiments at LHC and is dedicated for heavy ion collisions.

Figure 3.2 shows the schematics of the ALICE detectors. In order to cope with high particle multiplicities in heavy ion collisions (up to $dN/d\eta \sim 8000$) and cover a wide momentum range with excellent particle identification, various detectors with high granularity and good PID performance in specific momentum ranges are installed in ALICE. The acceptance and main technology of each detector is summarized in Table 3.1. The details of the detectors related to this thesis are described from the next section.

In this thesis, the global coordinate system is defined as shown in Fig. 3.3. It is a right-handed coordinate system with the Z-axis parallel to the beam direction. The positive

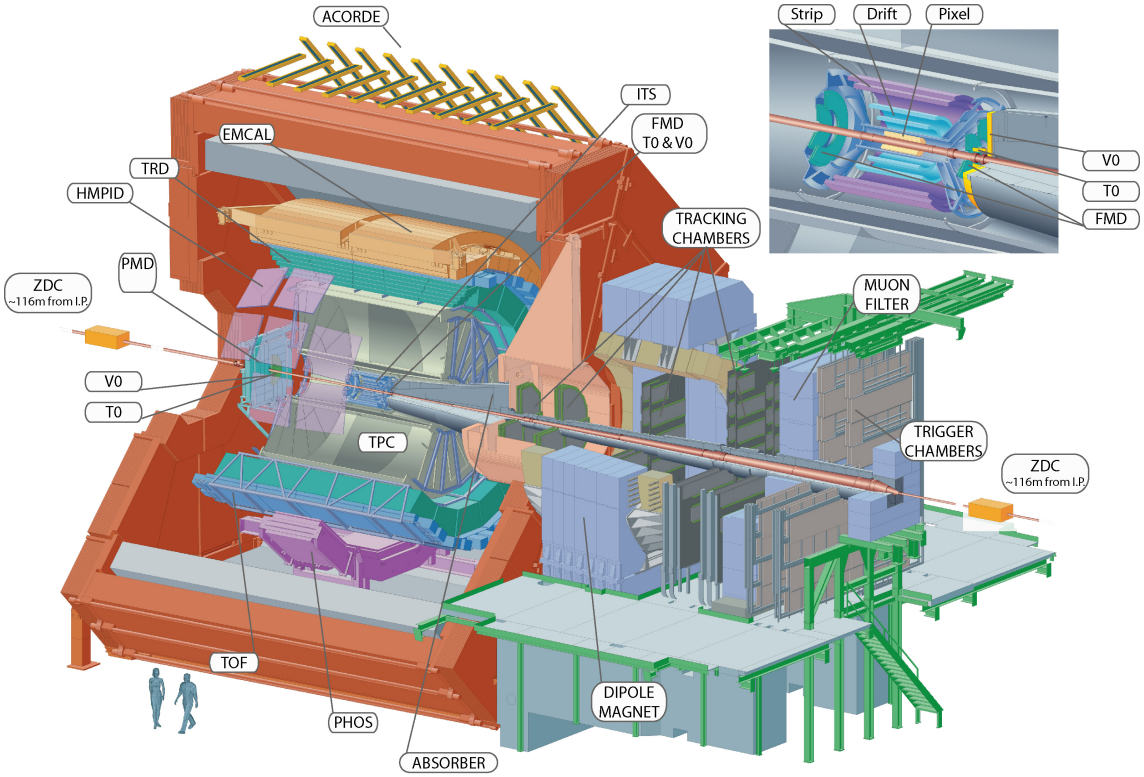

Figure 3.2: Schematics of ALICE detectors [84].

Detector	η coverage	Position	ϕ coverage	Technology	Main Purpose
ITS					
SPD	$\|\eta\|$ <2.0	r = 3.9 cm	full	Si pixel	tracking, vertexing
SPD	$\|\eta\|$ <1.4	r = 7.6 cm	full	Si pixel	tracking, vertexing
SDD	$\|\eta\| < 0.9$	r = 15.0 cm	full	Si drift	tracking, low p_{T} PID
SDD	$\|\eta\| < 0.9$	r = 23.9 cm	full	Si drift	tracking, low p_{T} PID
SSD	$\|\eta\| < 1.0$	r = 38 cm	full	Si strip	tracking, low p_{T} PID
SSD	$\|\eta\| < 1.0$	r = 43 cm	full	Si strip	tracking, low p_{T} PID
TPC	$\|\eta\| < 0.9$	85 < r < 247 cm	full	Ne/Ar drift+MWPC	tracking, PID
TRD	$\|\eta\| < 0.9$	290 < r <368 cm	full	TR+Xe drift+MWPC	tracking, electron ID
TOF	$\|\eta\| < 0.9$	370 < r < 399 cm	full	MRPC	PID
EMCAL	$\|\eta\| < 0.7$	430 < r < 455 cm	80 < ϕ < 187	Pb+scintillator	photon, electron ID, jet
V0					
V0A	2.8 < η < 5.1	z = 329 cm	full	scintillator	L0, multiplicity
V0C	-3.1 < η < -1.7	z = 188 cm	full	scintillator	L0, multiplicity
T0					
T0A	4.6 < η < 4.9	z = 370 cm	full	quartz	timing, vertexing
T0C	-3.3 < η < -3.0	z = -70 cm	full	quartz	timing, vertexing
MCH	-4.0< η <-2.5	$-1.4 < z < -5.4$ m	full	MWPC	muon tracking
MTR	-4.0< η <-2.5	$-17.1 < z < -16.1$ m	full	RPC	muon trigger

Table 3.1: Summary of acceptance and main technology for subdetectors in ALICE [84].

Z-axis is the opposite direction of the Muon arm, called 'A-side'. 'C-side' is defined as the opposite side of A-side.

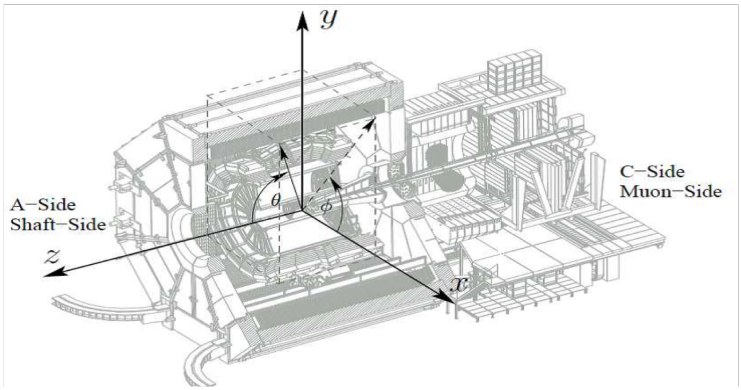

Figure 3.3: Global coordinate of ALICE detectors [33].

3.3 ALICE Global Detectors

3.3.1 V0 Detector

The V0 detector is a scintillation detector mainly used for minimum bias trigger decision and determination of event characteristics. It is composed of V0A in A-side and V0C in C-side. The V0A is located 340 cm away from the interaction point and covers $2.8 < \eta <$ 5.1. The V0C is installed 90 cm from the interaction point and covers -3.1 $< \eta <$ -1.7. They have 4 and 8 segments in the r and ϕ directions, respectively as shown in Fig. 3.4.

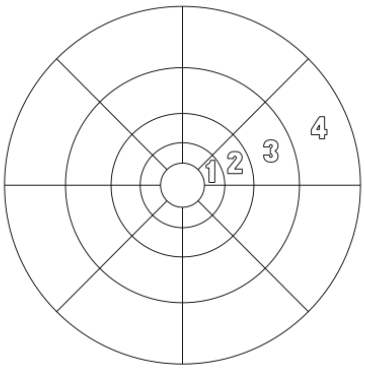

Figure 3.4: Segmentation of V0 detector [83].

The event centrality and the event plane are estimated via measurements of the charged particle multiplicity in each segment of V0. Figure 3.5 shows the distribution of the V0A amplitude in p–Pb collisions. The amplitudes of the V0 detector are proportional to the charged particle multiplicities [86]. The red line in Fig. 3.5 shows the result of the NDB-Glauber fit [87–90]. The event centrality is determined by the percentile of this distribution. The timing resolution of V0 is about 1 ns which enables the rejection of background events caused by beam-gas and beam-halo interactions.

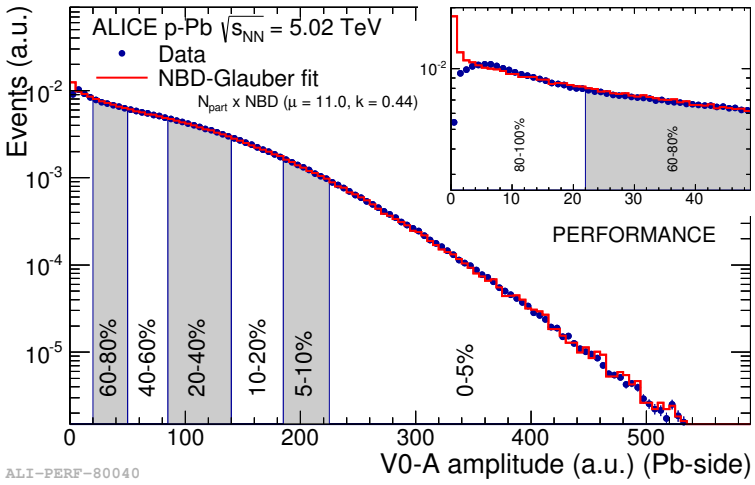

Figure 3.5: V0A multiplicity distribution in p–Pb collision at $\sqrt{s_{NN}}$ =5.02 TeV (Pb-going side) [86].

3.3.2 T0 Detector

The T0 detector is arrays of Cherenkov counters to measure collision time with high precision. The time resolution achieves 40 ps and 25 ps in pp and Pb–Pb collisions. The collision time is used as the reference time for TOF detector. T0 is also used for the determination of primary vertex positions with a precision of about 1.2 cm in pp collisions.

3.4 Detectors in the ALICE Central Barrel

The main tracking detectors in the central barrel are ITS, TPC, and TRD. The magnetic field in the central barrel is 0.5 T.

3.4.1 Inner Tracking System (ITS)

The Inner Tracking System (ITS) is the closest detector to collision points. Figure 3.6 shows the layout of ITS. ITS consists of 6 layers of silicon detectors, two Silicon Pixel Detectors (SPD), two Silicon Drift Detectors (SDD), and two Silicon Strip Detectors (SSD). SPD consists of hybrid silicon pixels with thickness of 200 μm and pixel size of 50 μm ($r\phi$) $\times$ 425 μm (z). SDD consists of a 300 μm thick layer of homogeneous high-resistivity silicon wafers. SSD consists of double-sided silicon micro-strip sensors. The strip pitch is 95 μm and the relative p-n side stereo angle is 35 mrad. ITS cover the full azimuthal acceptance and the pseudo-rapidity coverage of SPD, SDD, and SSD is $|\eta| < 2.0$, $|\eta| < 0.9$, and $|\eta| < 0.9$, respectively. The typical features of each layer are summarized in Table. 3.2.

Figure 3.7 shows an example of ITS hits and track reconstruction in pp collisions at $\sqrt{s_{NN}}$ = 900 GeV [92]. The main purpose of ITS is to determine the position of the

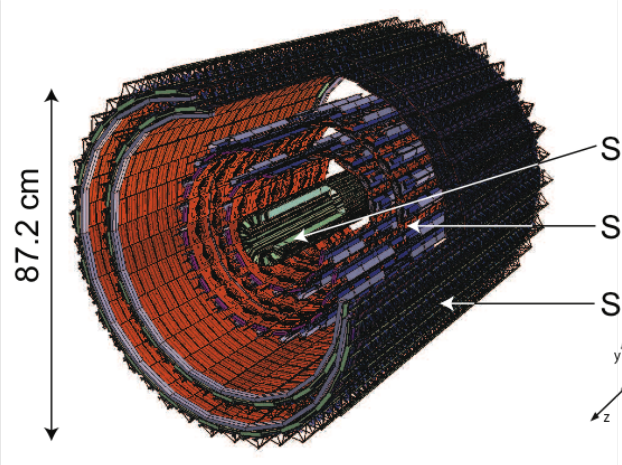

Figure 3.6: Schematics of ITS layout [91].

Layer	Detector Type	Radius (cm)	Length (cm)	$\Delta r\phi$ (μm)	ΔZ (μm)
1	SPD	3.9	28.2	12	100
2	SPD	7.6	28.2	12	100
3	SDD	15.0	44.4	35	25
4	SDD	23.9	59.6	35	25
5	SSD	38.0	86.2	20	830
6	SSD	43.0	97.8	20	830

Table 3.2: Detector type and general features of each layer of ITS [91].

primary vertex and secondary decay vertex. The offline track reconstruction is done in conjunction with the TPC. Offline track reconstruction is described in Section 3.6.

SDD and SSD can provide the information on specific energy loss dE/dx in SDD which follow the Bethe-Bloch formula and ITS dE/dx is used for the particle identification at relatively low momentum below 1 GeV/c.

3.4.2 Time Projection Chamber (TPC)

The Time Projection Chamber (TPC) is a large gaseous detector. TPC is used as the main tracker in the central barrel of ALICE. TPC is designed to satisfy the following specifications:

- dE/dx resolution: better than 5%.
- Relative p_{T} resolution: better than 1% at $p_{\mathrm{T}} = 1$ GeV/c and 2.5% at $p_{\mathrm{T}} = 4$ GeV/c.
- Two track resolution capability capability of separating tracks with a relative momentum difference < 5 MeV/c.

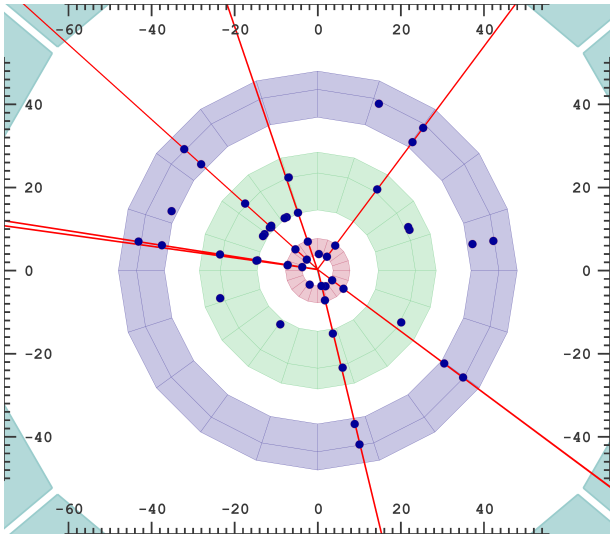

Figure 3.7: ITS hits of first proton-proton collision at $\sqrt{s_{NN}}$ =900 GeV. The navy points show the hit on ITS and the red lines show the reconstructed tracks [92].

Figure 3.8 shows the schematics of TPC. It consists of a large cylindrical a gas volume with 85 cm inner radius and 250 cm outer radius. The length of the chamber is 500 cm along with the z-axis. The gas volume is 88 m^3 and filled with Ne/CO_2 or Ar/CO_2. Ne/CO_2 (90%/10%) gas mixture was filled in the TPC during Run1.

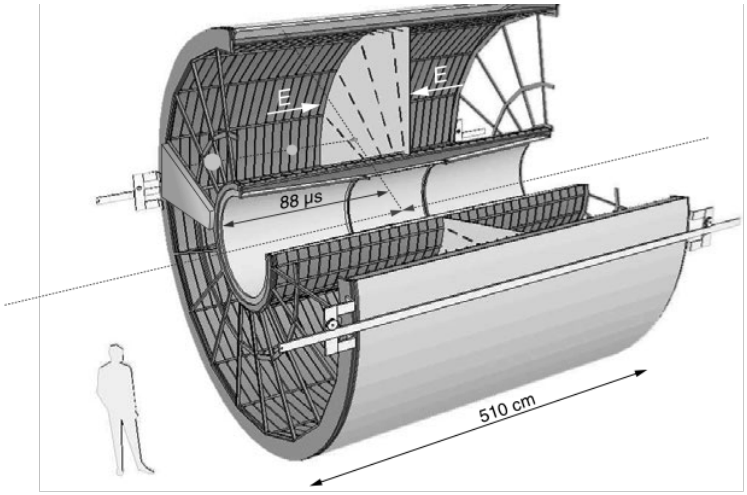

Figure 3.8: Schematics of TPC layout [93].

The electric field in the drift volume is 400 V/cm. The maximum drift time is 90 μs. The primary electrons ionized by the interaction of charge particles inside the active volume drift toward the end-plane. Figure 3.9 shows the schematics of the TPC readout. The gating grid of the readout chamber is usually closed. When TPC accepts L1 trigger in 6.5 μs after a collision, the gating grid is open. Primary charges are multiplied by the Multi-Wire Proportional Chambers (MWPCs) with gas gain 7000-8000. Readout signals

are induced on the pad-planes. The analog signals are processed by preamplifier and

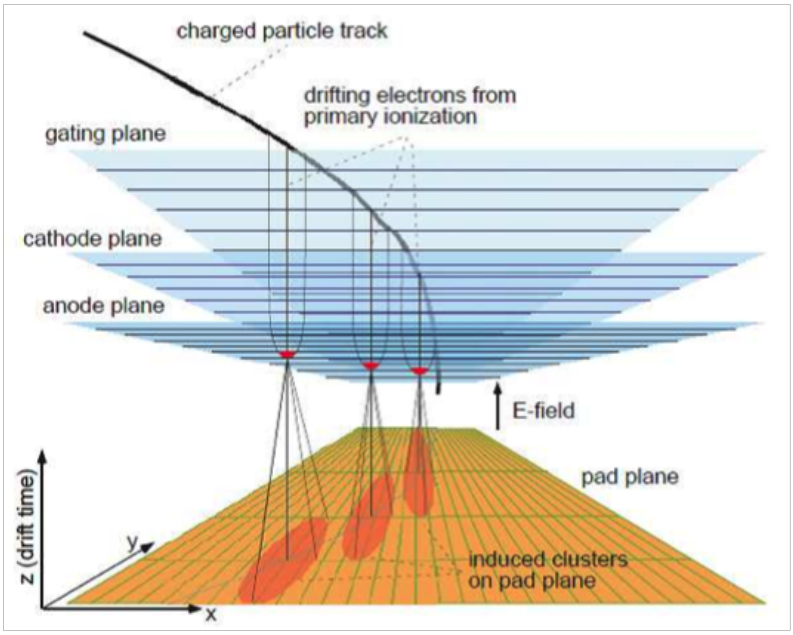

Figure 3.9: Schematics of readout chambers of TPC [93].

shaper (PASA) chip and are digitized by 10-bit pipelined-ADC with 10 MHz sampling [95].

3.4.3 Transition Radiation Detector (TRD)

The main purpose of the Transition Radiation Detector (TRD) is to provide electron identification in wide momentum range and charged particle tracking in the central barrel. The pion rejection factor at 90% electron efficiency is 100 above 1 GeV/c.

TRD covers the full azimuthal acceptance with 18 super modules. The pseudo-rapidity coverage is $|\eta| < 0.9$. The super module is divided into 5 stacks along the η direction. Each stack consists of 6 layers of polypropylene fiber mat as radiator+MWPC as shown in Fig. 3.10. MWPC is operated in Xe/CO_2 to absorb transition radiation from the radiator. In Run1, 13 super modules are installed and operational.

Charged particles with Lorentz factor of $\gamma > 800$ generates transition radiation in the TRD. Therefore, electrons and pions can be separated from 1 to 100 GeV/c. Xe has a good absorption length for transition radiation photons ($E_{TR} \sim 10$ keV) as shown in Fig. 3.11 and transition radiation photons are sufficiently absorbed in the readout chamber.

The left panel of Fig. 3.12 shows the schematics of the readout chamber. The readout chamber is operated at the drift field = 700 V/cm and the drift velocity reaches 1.5 cm/μs. The drift length is 3 cm. The signals are readout with PASA and TRAP (Tracklets Processor) chip on the Multi-Chip Module (MCM) mounted on the Readout Board (ROB). ROB is located behind the back-plane of chamber.

The sampling frequency of 10-bits ADC in TRAP is 10 MHz and the number of time bins is 22–24. The right panel of Fig. 3.12 shows the pulse height for electrons and pions [94]. The signals contain specific energy loss for each species via ionization and the

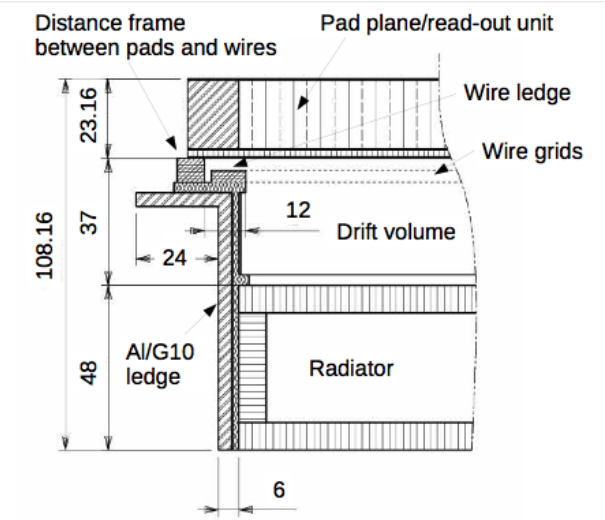

Figure 3.10: The corss section of the TRD chamber [94].

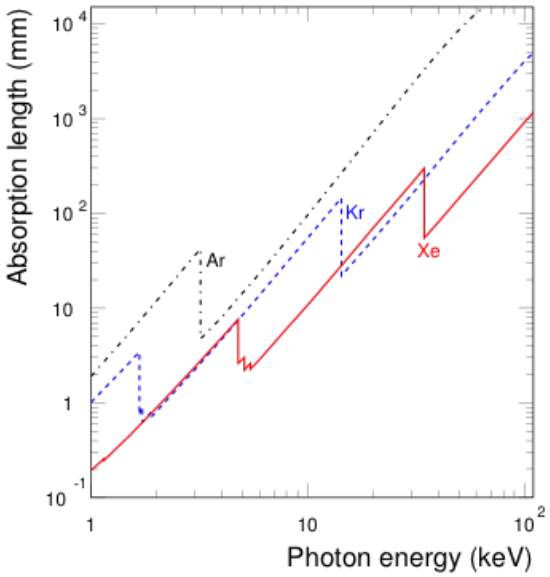

Figure 3.11: Absorption length for gases [94].

contribution of the transition radiation photons for electrons. The contribution of the transition radiation photons localizes at the latter time bins. The digital filtering such as non-linearity, pedestal filter, gain correction, and tail cancellation is done in the MCM.

Figure 3.13 shows the performance plots of electron/pion separation using TRD [84]. In the LQ1D method, the electron likelihood is calculated as a function of inclusive charge sum. The LQ2D method is based on the electron likelihood calculation as a function of charge sum in the earlier time bins and that in the later time bins. Since the signals of transition radiation localize in the later time window, better electron/pion separation can be obtained compared to the LQ1D method. The right panel of Fig 3.13 shows the pion

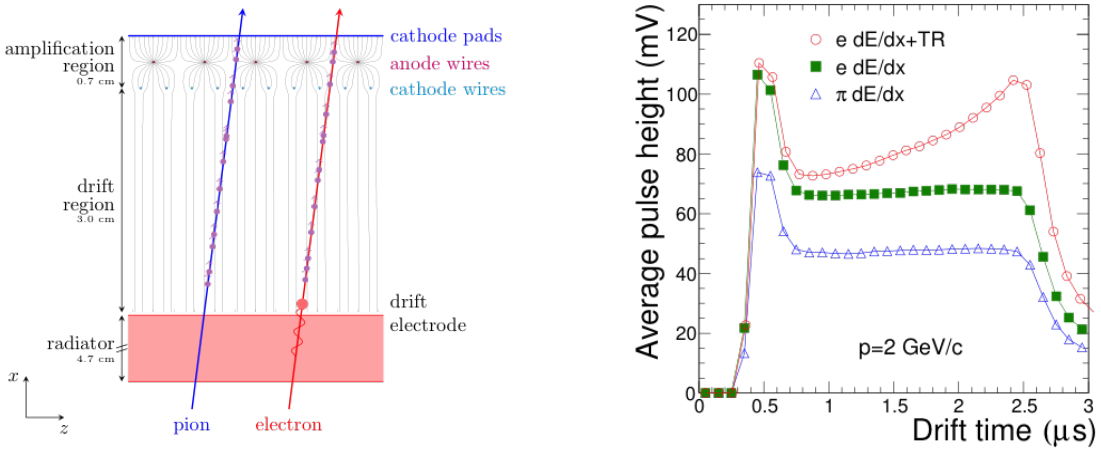

Figure 3.12: Left: Schematics of the readout chamber of TRD. Left: Average pulse height as a function of the drift time for pions and electrons. The signal of transition radiation photons contribute to the latter time bins [94].

efficiency at 90% electron efficiency using several methods. The pion rejection can reach 100 at $p_{\mathrm{T}} = 2$ GeV/c by LQ2D.

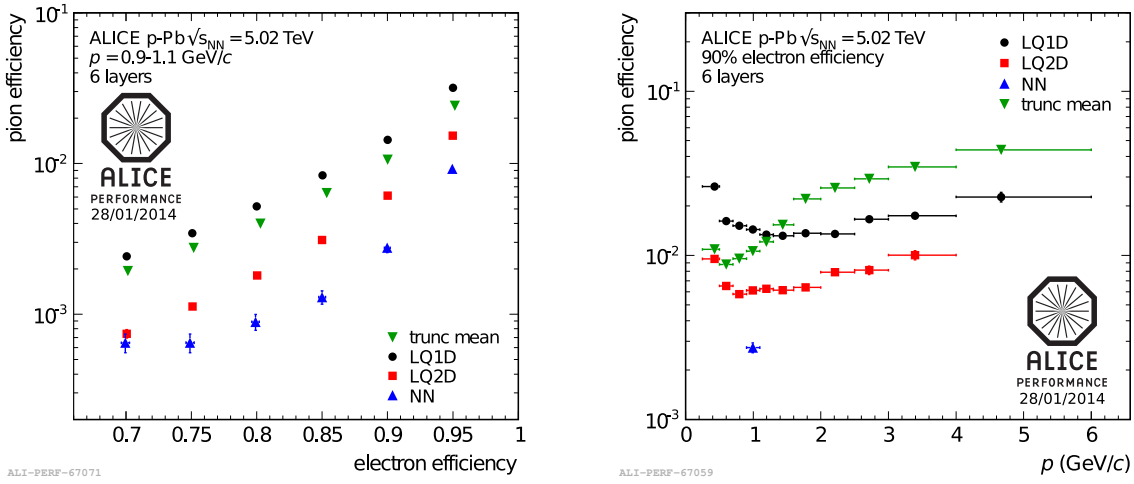

Figure 3.13: Left Panel: Electron Efficiency vs Pion Efficiency with TRD PID in p–Pb collision at $\sqrt{s_{NN}} = 5.02$ TeV. Right Panel:Pion Efficiency at the electron efficiency = 90 % with TRD PID as a function of transverse momentum in p–Pb collision at $\sqrt{s_{NN}} =$ 5.02 TeV [84] .

3.4.4 Time-Of-Flight detector (TOF)

The Time-Of-Flight detector (TOF) is used for the particle identification of pions, kaons, protons, and electrons at $p_{\mathrm{T}} < 3.0$ GeV/c. Figure 3.14 shows the layout of TOF. It is located at radius of 3.8 m and covers the full azimuthal acceptance and $|\eta| < 0.9$ with 18 super modules in ϕ.

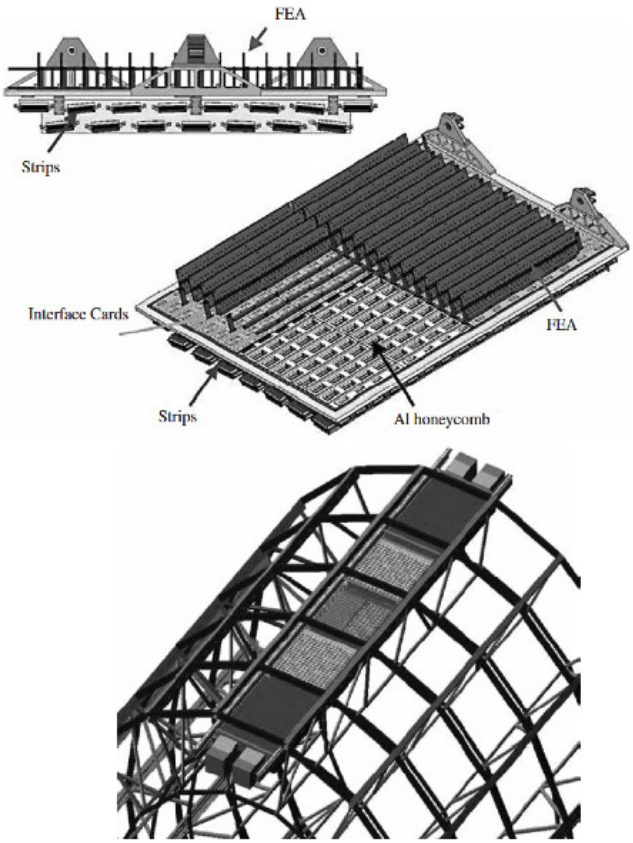

Figure 3.14: Schematics of Super modules of TOF and detail of one TOF module of aluminium honeycomb plane [96].

Figure 3.15 shows the schematics of Multi-gap Resistive Plate Chamber (MRPCs) for TOF. The chamber is divided into two stacks on each side of the central anode. Each stack has five gas gaps of 250 μm to keep high and uniform electric field. When charged particles transverse the chambers, an avalanche of electrons occurs immediately. The avalanche electrons are readout with the pad of 2.5×3.5 cm^2 arranged in two rows. The time resolution of TOF achieves 40 ps. The start time of Time-Of-Flight is determined by the T0 detector. Considering other uncertainties, the arrival time of charged particles can be measured with the time resolution less than 100 ps.

3.5 Vertexing

Primary vertices are determined by two steps. First estimation of primary vertices is performed using hits on the SPD detector. Pairs of SPD hits in inner and outer layers which have close azimuthal angles (< 0.01 rad) are selected as SPD tracklets and they have to cross the cylindrical fiducial region where the interaction point is expected to be located (inside the beam pipe). After a cut on the distance of closest approach (DCA)

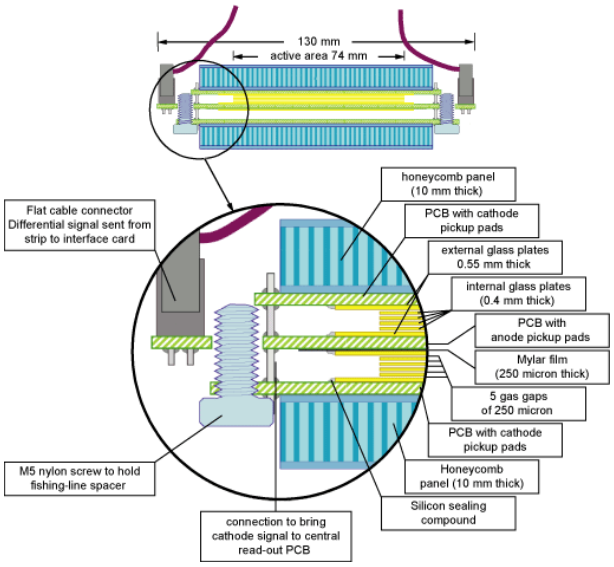

Figure 3.15: Schematics of MRPCs for TOF [96].

between the to tracklets ($DCA < 1$ mm), a center position of all pairs of tracklets (pre-vertex) are calculated. The following value is calculated for all selected tracklets whose DCA to the pre-vertex are within 1mm:

$$d_i = \sum_{x=(X,Y,Z)} \frac{x_i - x_0}{\sigma_{x_i}}, \tag{3.1}$$

where x_0 is an expected 3-D position of a vertex, x_i and σ_{x_i} are a 3-D position and resolution of tracklets, respectively. The position of the primary vertex with SPD is determined by the position which minimizes the value of D $= \sum_i d_i^2$. SPD is operated in the magnetic field but the bend before the SPD is negligible. This vertex is used for the offline track reconstruction described in the next section.

The final positions of primary vertices are recalculated with reconstructed tracks using ITS and TPC. The 3-D position of primary vertices are calculated as the central positions among selected track pairs by the closest approach. Figure 3.16 shows the finding efficiency and the position resolution of the primary vertex reconstruction with reconstructed tracks as a function of the charged particle multiplicity.

3.6 Tracking System of Charged Particles with the ALICE Detectors

Track reconstruction in the central barrel is performed using clusters found in each detector along the trajectory of charged particles. The track reconstruction follows three steps as shown in Fig. 3.17. The start points of the tracking are the most outer clusters in the TPC where the track density is relatively lower than that in inner detectors. TPC provides 159 clusters for each track candidate. Tracks are reconstructed using Kalman-Filter

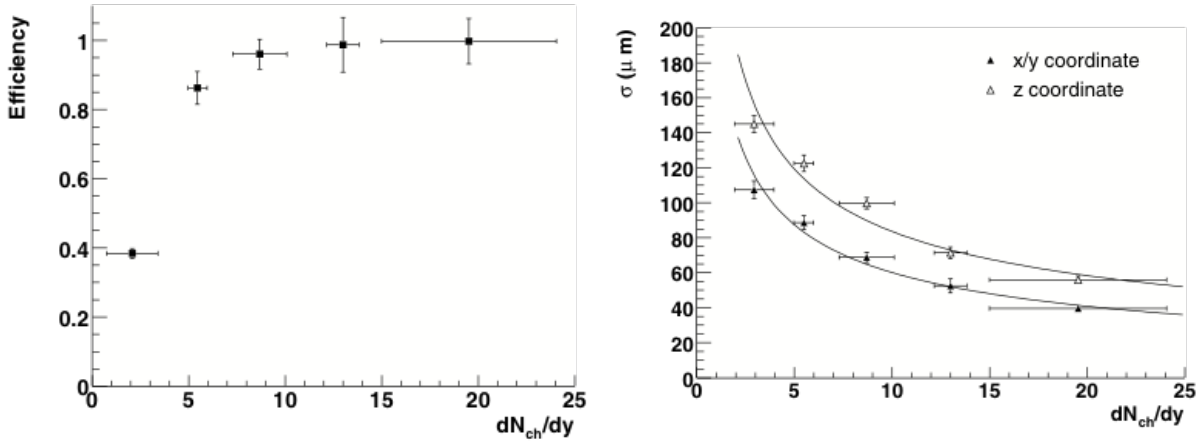

Figure 3.16: Efficiency (Left) and position resolution (Right) of the primary vertex with 3-D method in case of pp collisions [97].

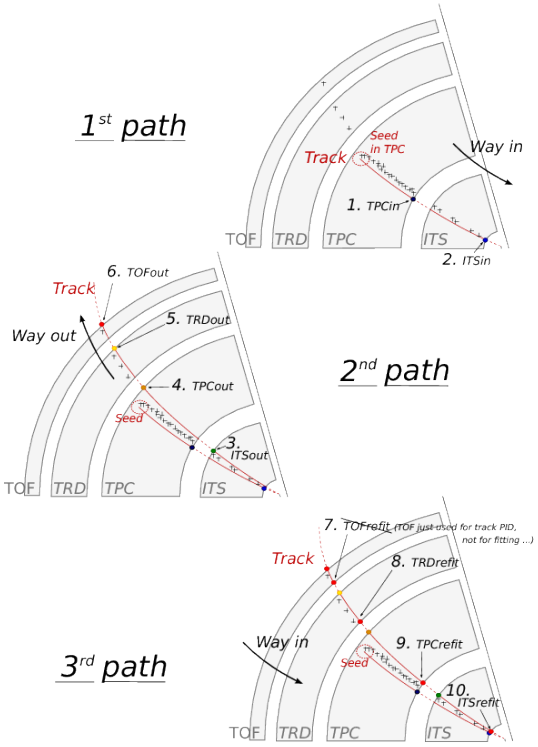

Figure 3.17: Principles of tracking for an ALICE event, showing the three successive paths allowing to build a track and refine its parameters. Numbers ranging from 1 to 10 mention the bits that are activated in case of success during the propagation of the Kalman filter at the considered stage [99].

algorithm inward. The track state vector is chosen as

$$x^T = (y, z, C, tan\lambda, \eta), \tag{3.2}$$

where y, z are local positions in the TPC, C is coverture and λ is dip angle between a track and a pad plane as shown Fig. 3.18. This process is done from high momentum

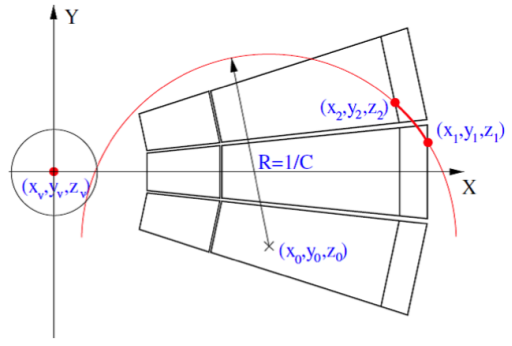

Figure 3.18: Local coordinate system for one sector of TPC.

candidates because these tracks can be found more precisely compared to low momentum tracks. After the propagation to the most inner ITS layer, propagation is re-done from ITS to TPC using Kalman-Filter. This propagation is also extended to TRD, TOF, and EMCAL when hits in these detectors exist. Finally, the propagation called 'refit' is done from outward to ITS to determine track positions.

Figure 3.19 shows the finding efficiency of TPC tracks in pp and Pb–Pb collisions [84]. The reconstruction efficiency is unchanged in pp and Pb–Pb collisions.

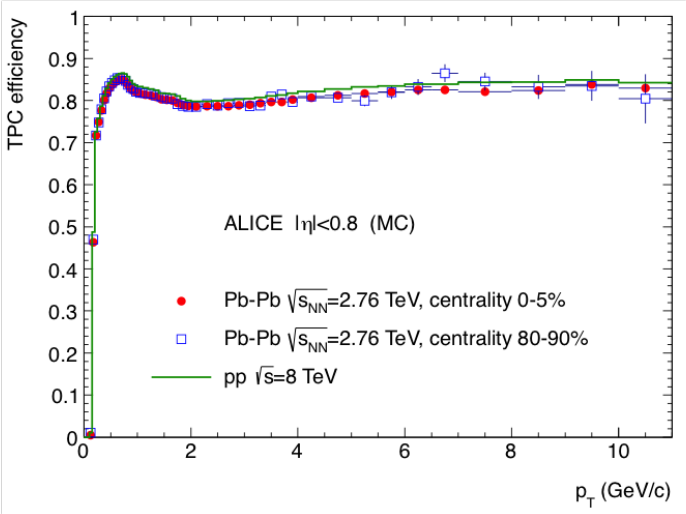

Figure 3.19: TPC track finding efficiency in pp and Pb–Pb collisions [84].

Figure 3.20 shows the transverse momentum resolution of reconstructed tracks in p–Pb collisions [84]. The y-axis is defined as follows:

$$\frac{\sigma_{p_{\mathrm{T}}}}{p_{\mathrm{T}}} = p_{\mathrm{T}}\sigma_{1/p_{\mathrm{T}}}. \tag{3.3}$$

With ITS hits, the momentum resolution can be improve significantly. The impact parameters of reconstructed tracks can also be determined precisely using ITS. The resolution of the impact parameters is below 50 μm at $p_{\mathrm{T}} > 1$ GeV/c.

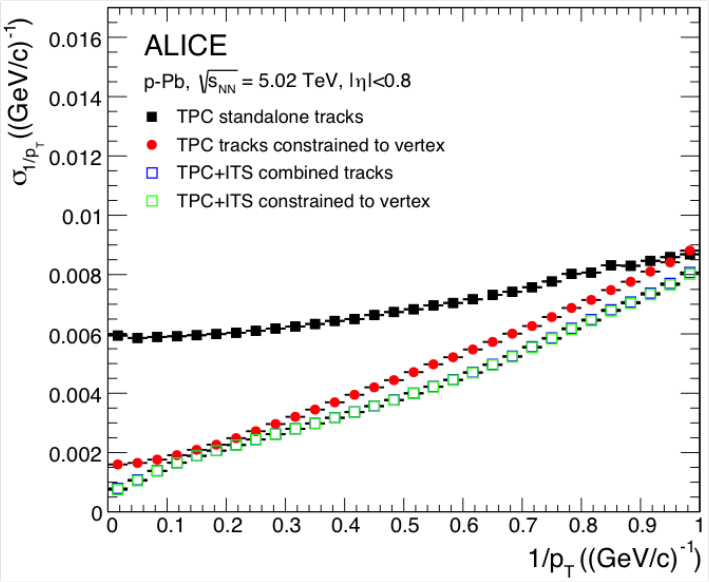

Figure 3.20: Inverse momentum resolution in p–Pb collisions at $\sqrt{s_{NN}}$ =5.02 TeV [84].

3.7 Particle Identification in ALICE

ALICE uses various detectors and techniques in wide momentum range to identify particle species. The main technique of the particle identification is specific energy loss (dE/dx) of charged particles deposited in the detectors such as ITS, TPC and TRD. The mean deposited energy loss in detectors can be described by the Bethe-Bloch formula:

$$-\langle\frac{dE}{dx}\rangle = \frac{4\pi}{m_e c^2}\frac{nz^2}{\beta^2}(\frac{e^2}{4\pi\epsilon_0})^2[ln(\frac{2m_e c^2\beta^2}{I(1-\beta^2)}) - \beta^2] \tag{3.4}$$

where e is the elementary charge, m_e is the electron mass, n is the number density of electrons in the target material, z is the charge of the particle, and I is the average ionization potential of the target atom.

TOF is useful to separate proton and kaon up to 3 GeV/c by measuring the flight time of particles. EMCAL helps electron and photon identification with their deposited energy.

3.7.1 TPC PID

The key information for the particle identification in ALICE is the TPC dE/dx. Figure 3.21 shows the TPC dE/dx distribution as a function of reconstructed momentum in p–Pb collisions [84]. In order to reduce the Landau fluctuation of the TPC dE/dx and

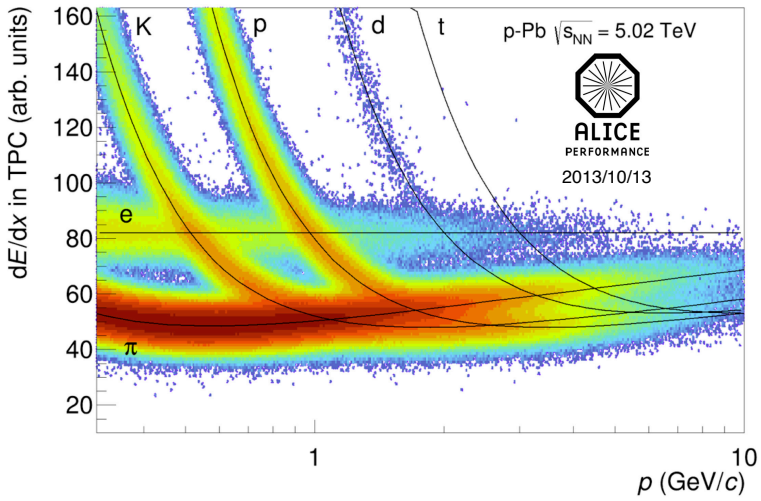

Figure 3.21: TPC dE/dx vs reconstructed momentum in p–Pb collision at $\sqrt{s_{NN}}$ =5.02 TeV [84].

achieve better performance of particle separation, truncated means of the TPC dE/dx are taken. 20–30% largest clusters are rejected in dE/dx calculation. The truncated mean distribution of the TPC dE/dx can be approximated to the Gaussian and the resolution reaches below to 5% for cosmic ray as shown in Fig. 3.22 [98].

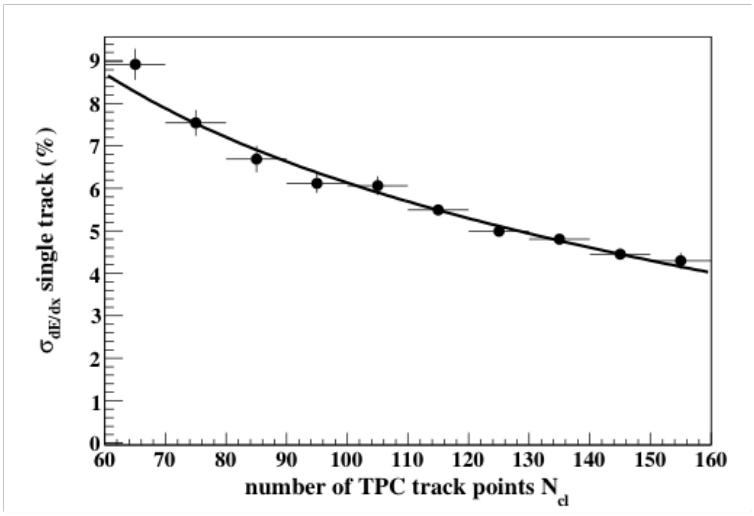

Figure 3.22: TPC dE/dx resolution with cosmic rays as a function the number of TPC hits [98].

3.8 Trigger System in ALICE

All communication on trigger information between subsystems is done via the Central Trigger Processor (CTP) with the TTC protocol [100, 101]. Figure 3.23 shows the block diagram of CTP [101]. CTP provides the trigger information and LHC timing signal (BC and Orbit) to subdetectors, and it also accept trigger signals from subdetectors.

The trigger scheme in ALICE consists of three steps called Level-0 (L0), Level-1 (L1), and Level-2 (L2) trigger. L0 trigger inputs from fast subdetectors such as V0, T0, EMCAL, and the muon arm are delivered into CTP within 900 ns after a collision. L0 triggers are issued by the CTP, and then L0 accept signals are sent to the subdetectors after 1.2 μs after a collision,

If each subdetector which contributes to L1 trigger receives a L0 accept signal, calculations for the L1 issue are performed and L1 contributions are sent to CTP. L1 triggers are issued after 6.5 μs from an interaction. If L1 triggers are accepted, raw data of subsystems is transferred to the multi event buffers.

L2 triggers are issued about 100 μs after the decision of L0 triggers, which is determined by the drift time of TPC. If L2 triggers are issued, the data is transferred from the event buffers in each subdetector to DAQ.

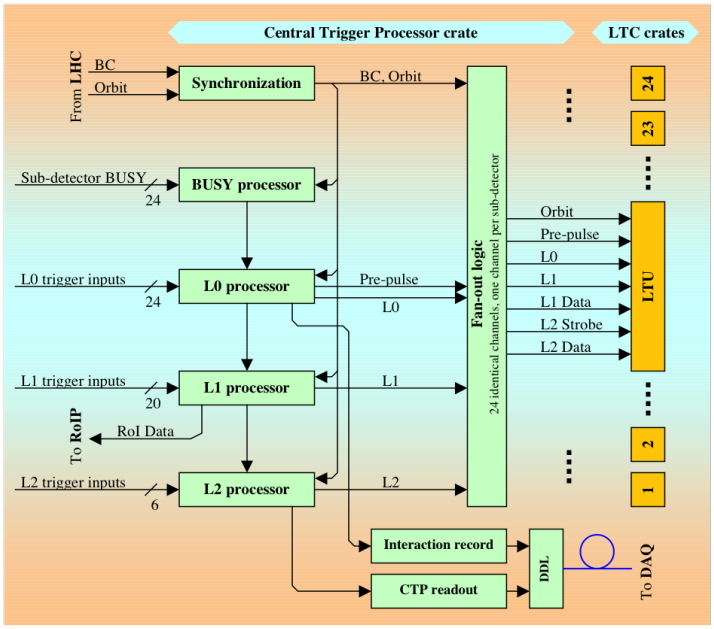

Figure 3.23: Block diagram of CTP [101].

3.9 Run Condition and Data Set

ALICE collected p–Pb collision data in two conditions, 'p–Pb' and 'Pb–p'. 'p–Pb' collisions are defined as a collision that Pb travels from C-side. On the other hand, 'Pb-p' collisions are defined that Pb is delivered from A-side. Due to the asymmetric energy of

colliding protons (4 TeV) and leads (1.58 TeV per nucleon), rapidity of the Center-of-Mass system is slightly shifted in the direction of Pb-going (~ 0.465).

Table 3.3 shows the run conditions in p–Pb collisions in Run1. The average collision rates were 10 kHz for the minimum bias data taking and 100 kHz for the rare triggered data taking. Figure3.24 shows the integrated luminosity of p–Pb collision collected by the ALICE detectors during Run1 [84]. The integrated luminosity of the TRD triggered data in p–Pb collisions is 1.4 nb^{-1}. It corresponds to 20 times larger statistics than the current minimum bias data (~ 0.067 nb^{-1}).

Parameters	Value
Proton Energy	4 TeV
Pb Energy	1.58 TeV
Protons per bunch	2×10^{10}
Pb ions per bunch	2×10^{8}
Peak Luminosity	1×10^{29} s^{-1}cm^{-2}
β^*	0.8
Transverse width	150 μm
Longitudinal emittance	6 cm
Number of Interacting Bunch	≤ 338
Collision frequency of LHC	112.45 kHz
Bunch spacing	200 ns

Table 3.3: Typical beam parameters for p–Pb collision in LHC Run1.

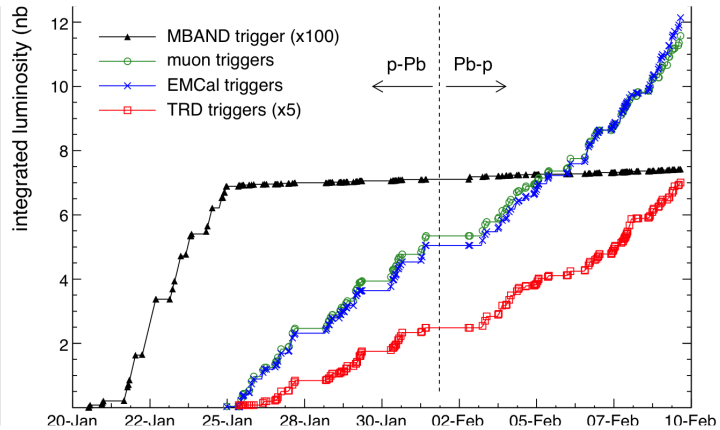

Figure 3.24: Integrated luminosity in p–Pb collisions at $\sqrt{s_{NN}}$ =5.02 TeV collected with ALICE in 2013 [84].

Chapter 4

Data Analysis

The main objective of this analysis is to extract J/ψ spectrum in the mid-rapidity region of p–Pb collisions. The analysis is performed using the minimum bias data of p–Pb collisions at $\sqrt{s_{NN}} = 5.02$ TeV. J/ψ measurements are performed in the ALICE central barrel using the dielectron (electron-positron pair) decay channel. ITS and TPC are the main devices used for vertexing, track reconstruction, and electron identification.

The invariant cross section of J/ψ production is calculated as follows:

$$\frac{1}{2\pi p_{\mathrm{T}}}\frac{d^2\sigma_{J/\psi}}{dp_{\mathrm{T}}dy} = \frac{1}{2\pi p_{\mathrm{T}}}\frac{1}{BR(J/\psi \to e^+e^-)} \times \frac{N_{J/\psi,raw}}{\int Ldt \times \epsilon \times \Delta y \Delta p_{\mathrm{T}}}, \tag{4.1}$$

where $N_{J/\psi,raw}$ is the number of reconstructed J/ψ and ϵ is the detection efficiency of J/ψ. Δp_{T} and Δy are the bin width of transverse momentum p_{T} and rapidity y, respectively, and $\int Ldt$ is the integrated luminosity of the analyzed data.

Comparisons of J/ψ production in p–Pb collisions and pp collisions is crucial for the understanding of nuclear matter effects. These effects are quantified by the nuclear modification factor (R_{pPb}) defined as

$$R_{\mathrm{pPb}}(p_{\mathrm{T}}) = \frac{\dfrac{d^2Y_{J/\psi,\mathrm{pPb}}}{dp_{\mathrm{T}}dy}}{< T_{\mathrm{pPb}} > \times \dfrac{d^2\sigma_{J/\psi,\mathrm{pp}}}{dp_{\mathrm{T}}dy}}, \tag{4.2}$$

where $Y_{J/\psi,\mathrm{pPb}}/dp_{\mathrm{T}}dy$ is the invariant yield of J/ψ in p–Pb collisions expressed as

$$\frac{d^2Y_{J/\psi,\mathrm{pPb}}}{dp_{\mathrm{T}}dy} = \frac{d^2\sigma_{J/\psi}}{dp_{\mathrm{T}}dy}\frac{1}{\sigma_{\mathrm{pPb}}}, \tag{4.3}$$

where σ_{pPb} is the cross section of p–Pb collisions. T_{pPb} is called the "nuclear thickness function" and is expressed as

$$T_{\mathrm{pA}}(b) = \int dz \rho_A(b,z) = \frac{\langle N_{coll} \rangle}{\sigma_{\mathrm{pp}}}, \tag{4.4}$$

where b and z are the impact parameter and the position in the nuclei along the beam direction of the p–Pb collisions, respectively. $\rho_A(b,z)$ is the nuclear density of nuclei with

mass number A. The thickness function is understood as the number of nucleons in the region where the incident proton passes through the nucleus and is normalized to satisfy $\int T_{\rm pA} db = \rm A$. The value of $\langle T_{\rm pPb} \rangle$ is estimated with Glauber model calculations and found to be 0.0983 ± 0.0035 mb^{-1} [104]. If there are no nuclear matter effects, $R_{\rm pPb}$ is equal to 1.

The following analysis steps are taken to calculate the invariant cross section of J/ψ in the p–Pb collisions:

1. **Event selection and luminosity determination**

2. **Electron identification**
   After the event selection, charged particles are reconstructed by ITS and TPC and electrons are identified by the energy deposition in the TPC.

3. **Pair analysis based on invariant mass analysis**
   After the electrons and positrons are identified, the invariant mass is calculated for all combinations of unlike-sign pairs (e^+e^-):

$$m_{ee} = \sqrt{(E_{e^+} + E_{e^-})^2 - (\vec{p_{e^+}} + \vec{p_{e^-}})^2}, \tag{4.5}$$

   where $E_{e^+} = \sqrt{m_e^2 + |\vec{p_{e^+}}|^2}$ and $E_{e^-} = \sqrt{m_e^2 + |\vec{p_{e^-}}|^2}$ are the energies of electrons and positrons calculated using the electron mass m_e, and the reconstructed momentum of the electrons ($\vec{p_{e^+}}$) and positrons ($\vec{p_{e^-}}$), respectively.

4. **Subtraction of background pairs from unlike-sign pairs**
   In order to extract the number of reconstructed J/ψ signals, background subtraction is required. The main source of the background is combinatorial pairs from completely uncorrelated electron-positron pairs. In order to evaluate the combinatorial background, the event mixing technique is adopted. Overall background including correlated pairs is subtracted by the mixed pairs normalized by the side-band region.

5. **Acceptance and efficiency corrections.**
   Acceptance and efficiency are evaluated using Monte-Carlo (MC) simulations.

In this chapter, the event selection is discussed first in Section 4.1. Section 4.2 describes the run quality check. Sections 4.3 and 4.4 describe how the electron samples are reconstructed and selected. The conversion rejection is discussed in Section 4.5. The raw signal extraction of J/ψ is discussed in Section 4.6 and acceptance and efficiency correction is explained in Section 4.7. The extraction of the pp reference is also discussed in Section 4.9.

4.1 Event Selection

4.1.1 Minimum Bias Event Selection

Minimum bias events are triggered using information from V0, T0, and SPD. In this analysis, the criterion for a minimum bias trigger is coincidence of the hits in both of V0A

and V0C. In order to exclude beam-gas and beam-halo collisions, the timing information of V0 and T0 are utilized.

The primary vertex is reconstructed as described in Section 3.5. In this analysis, the minimum number of tracks, which contributed to the determination of the primary vertex, is required to be

- $N_{contribute} > 1$

Additionally, it is necessary for the Z-position of the primary vertex to be within 10 cm from the interaction point to maintain uniformity in the acceptance and reconstruction performance.

- $|Z_{vtx}| < 10$ cm

Figure 4.1 shows the Z_{vtx} distribution of the primary vertex in the p–Pb collisions. The event selection efficiency (ϵ_{sel}) of 88.9% is calculated as the ratio of the number of events satisfying the Z_{vtx} cut to the integral of Gaussian function fitted to the Z_{vtx} distribution of the selected events. After the event selection, the number of selected events ($N_{MB,ana}$) is

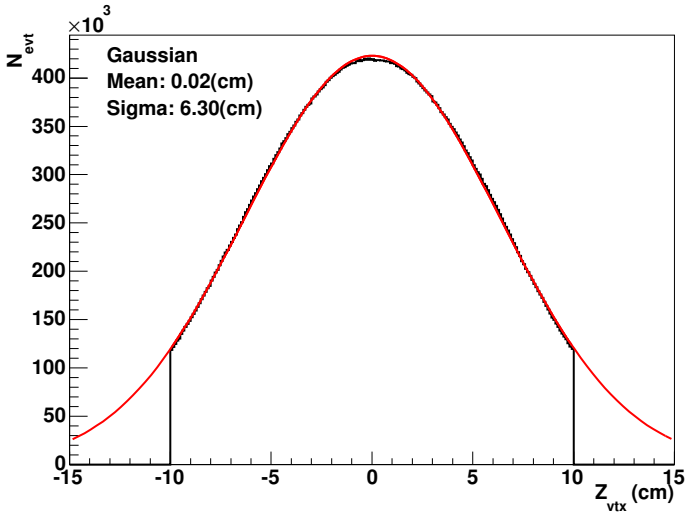

Figure 4.1: Z_{vtx} distribution of the accepted minimum bias events in the p–Pb collisions. The red line shows the result of the gaussian fitting to the data.

96 M events. The number of events for the luminosity calculation ($N^{corr}_{MB,ana}$) is calculated as $N_{MB,ana}/\epsilon_{sel}$.

The trigger cross section (σ_{V0}) is 2.09 ± 0.06 b measured with a van der Meer scan [113]. The trigger efficiency of non-single diffractive (NSD) events in p–Pb collisions is (96.4 ± 3.1)% [105]. Therefore the number of NSD events (N^{corr}_{NSD}) is expressed as $1.037 \times N^{corr}_{MB,ana}$ and the integrated luminosity of the analyzed events is calculated as follows:

$$\int Ldt = \frac{N^{corr}_{NSD}}{\epsilon_{sel} \times \sigma_{V0}} \sim 53.2\ \mu\mathrm{b}^{-1}. \tag{4.6}$$

4.2 Run Quality Check

A run quality check is performed based on the number of electron candidates per event. Figure 4.2 shows the number of electron candidates after electron identification divided by the number of analyzed events in each run for the minimum bias run periods of the $p_{\mathrm{T}} = 1$–2 GeV/c, $p_{\mathrm{T}} = 2$–4 GeV/c, and $p_{\mathrm{T}} > 4$ GeV/c bins, respectively. The electron candidates are selected with the track quality cut summarized in Table. 4.1, the TPC inclusion cut $|\mathrm{n}\sigma_{\mathrm{ele}}| < 3$, and the TPC exclusion cuts $|\mathrm{n}\sigma_{\mathrm{pi}}| > 3.5$ and $|\mathrm{n}\sigma_{\mathrm{pro}}| > 3.5$, as described in Section 4.4. To quantify the variation in the average number of electrons, the plots in Fig. 4.2 are projected on to Y-axis as shown in Fig. 4.3. The projected distributions are fitted to Gaussian function and all runs are within 5 σ from the mean points in all categories, and therefore, all runs are accepted.

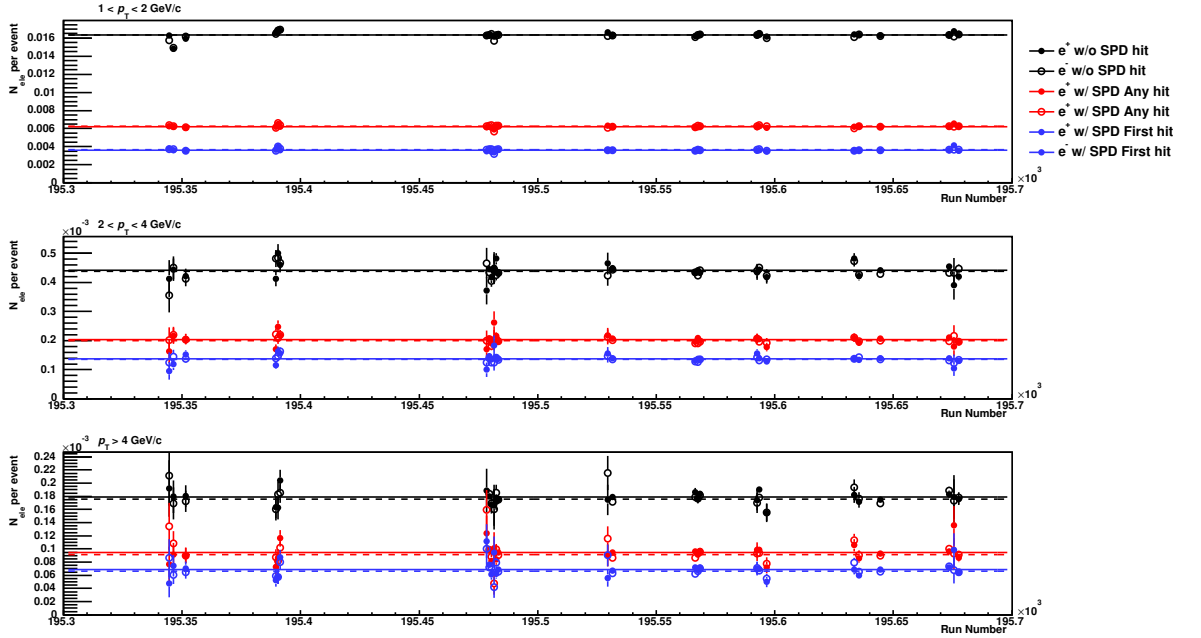

Figure 4.2: The average number of accepted electrons per event after the typical track quality and electron identification cuts are applied. From top to down, the p_{T} bins are $p_{\mathrm{T}} = 1$–2 GeV/c, $p_{\mathrm{T}} = 2$–4 GeV/c, and $p_{\mathrm{T}} > 4$ GeV/c, respectively. The black line shows the result without the SPD hit requirement. The red and blue markers show results with the requirement of the hits on at least one SPD layers ("SPD Any") and on the first layer of SPD ("SPD First"), respectively, as described in Section 4.3.

4.3 Track Selection

4.3.1 Kinematic Selection

The kinematical selection of electron p_{T} and η is studied using a single J/ψ simulation. The left panel of Fig. 4.4 shows the p_{T} distribution of leg electrons (positrons) that have

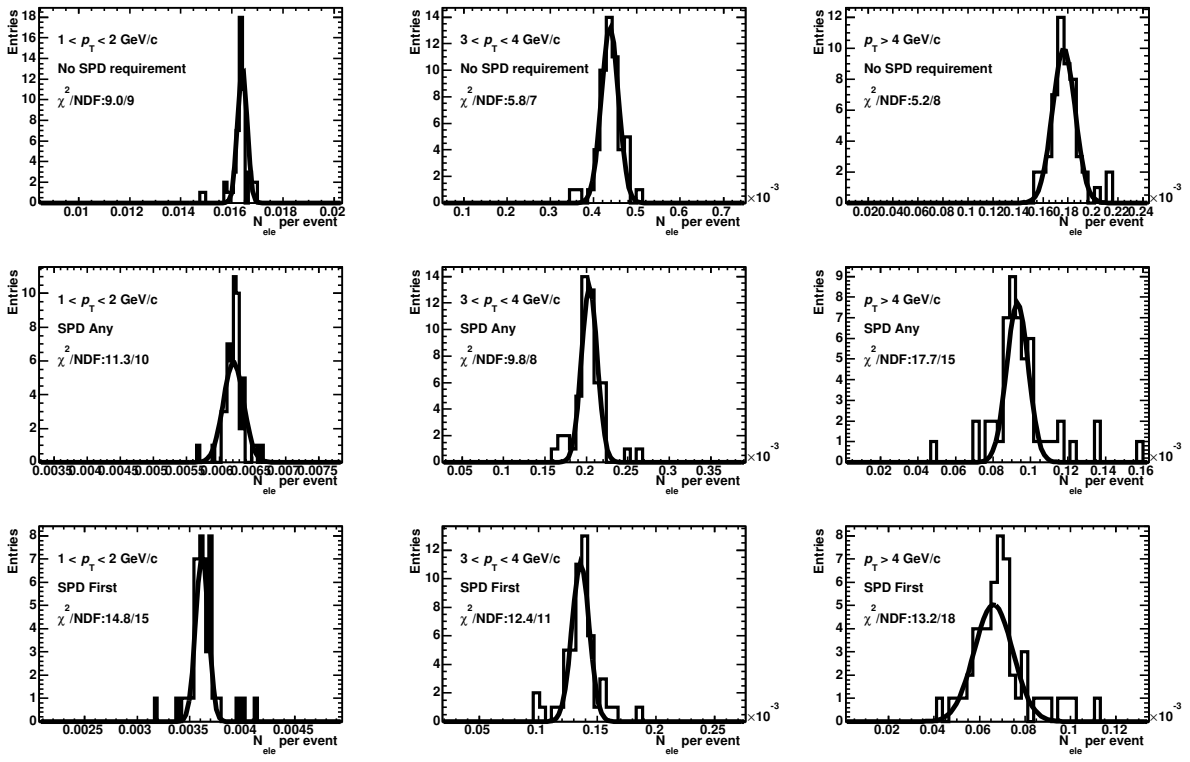

Figure 4.3: The projection of the number of accepted tracks after the typical track quality and electron identification cuts for each run and the fitted results. The results contain both electron and positron candidates.

larger p_{T} than the other leg positrons (electrons). The right panel of Fig. 4.4 shows the p_{T} distribution of leg electrons (positrons) that have lower p_{T} than the other leg positrons (electrons). Since J/ψ has an invariant mass of 3.096 GeV/c^2, both electrons and positrons have relatively high p_{T} ($\sim$ 1.5 GeV/c) with large opening angle at low mother p_{T}. At intermediate mother p_{T}, one leg electron carries a large amount of the mother momentum.

Figure 4.5 shows the inclusive electron spectrum and the expected contributions from all electron sources. At lower p_{T} below 1 GeV/c, light hadron decays and photon conversion electrons are dominant. In order to maintain a good signal to background ratio for J/ψ, the following kinematic selection is applied:

- $p_{\mathrm{T}}^{e} > 0.8$ GeV/c or 1 GeV/

  c

  .

- $|\eta^{e}| < 0.9$.

In the p_{T} differential analysis, different track and PID cuts are applied for each J/ψ p_{T} bin, which is summarized in Table 4.4, to maximize the signal significance.

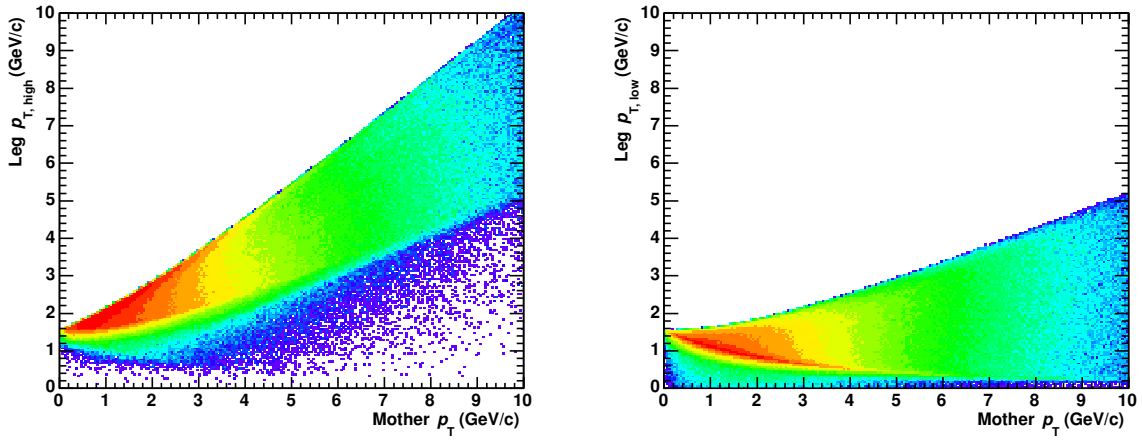

Figure 4.4: p_{T} distribution of J/ψ decay electrons with higher p_{T} (left) and lower p_{T} (right) in the Monte-Carlo simulation.

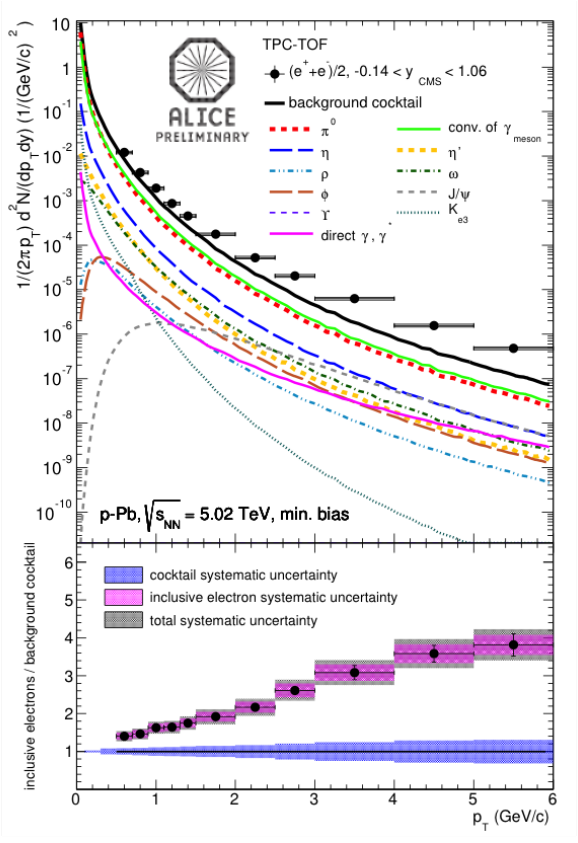

Figure 4.5: Inclusive single electron spectrum in p-Pb collisions.

Figure 4.6 shows the kinematic acceptance of J/ψ in the Monte-Carlo simulation. The

kinematic acceptance is defined by

$$\epsilon_{kin} = \frac{\text{The number of J}/\psi \text{ after leg } p_{\mathrm{T}} \text{ and } \eta \text{ cuts in } |y| < 0.9}{\text{The number of generated J}/\psi \text{ in } |y| < 0.9}. \tag{4.7}$$

The kinematical selection with $p_{\mathrm{T}}^{e} > 1$ GeV/c keeps the acceptance for J/ψ from low to high p_{T}.

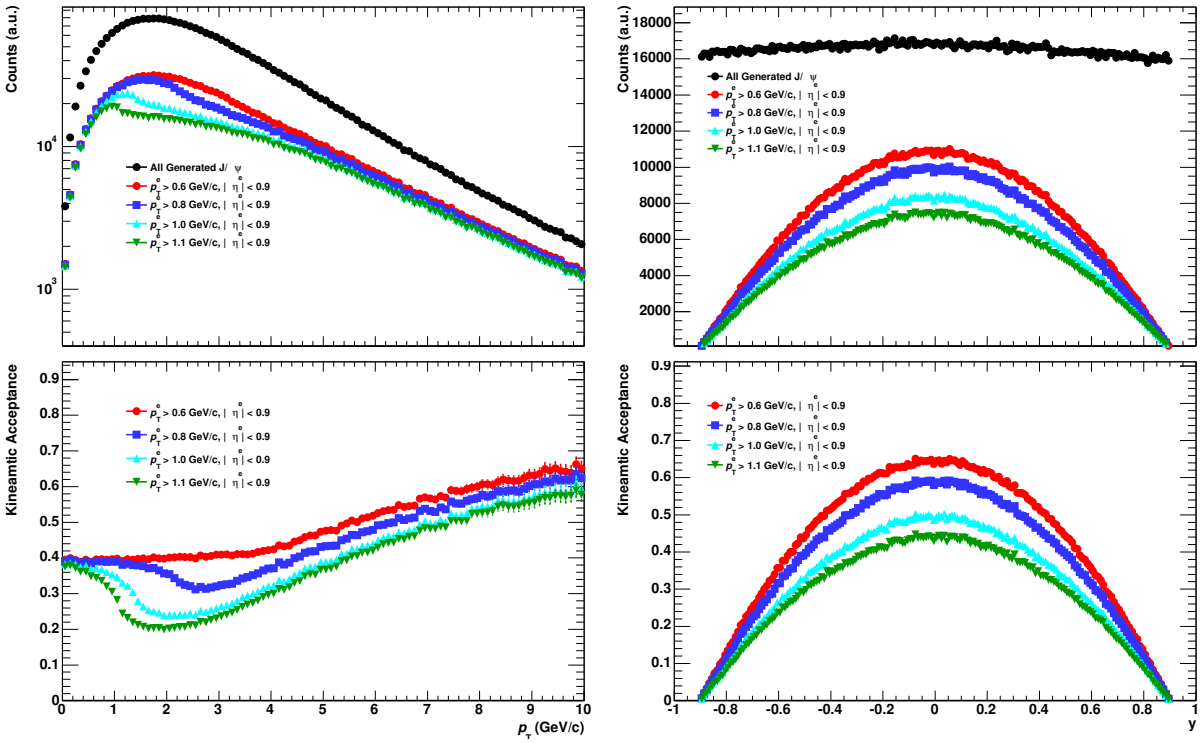

Figure 4.6: Kinematic acceptance of J/ψ as a function of p_{T} (left) and y (right) from the Monte-Carlo simulation.

4.3.2 Track Quality Cuts

Cut	Value
Minimum leg p_{T}	> 1 GeV/c
$\lvert\eta^{e}_{lab}\rvert$	< 0.9
Refit	ITS and TPC
Number of TPC clusters (TPC N_{cls})	> 70
TPC χ^2/N_{cls}	< 4
$\lvert DCA_{XY}\rvert$	< 1 cm
$\lvert DCA_{Z}\rvert$	< 3 cm

Table 4.1: Summary of cut settings for track reconstruction.

Charged tracks are reconstructed using hits in the ITS and TPC as described in Section 3.6. In order to select good track samples, ITS and TPC quality cuts are applied. All tracks are required to be re-fitted, as described in Section 3.6. Loose impact parameter cuts for the XY-plane and Z-axis are also applied ($DCA_{XY} < 1$ cm, $DCA_Z < 3$ cm). The impact parameter (DCA) is defined as the minimum distance between tracks and the primary vertex. Figure 4.7 shows the distribution of the number of TPC clusters and χ^2 between the reconstructed tracks and associated TPC clusters divided by the number of TPC clusters of the electron candidates for 1–3, 3–5, 5–8 GeV/c. They are selected by electron inclusion and pion exclusion cuts of the TPC dE/dx, as described in Section. 4.4. There are clear discrepancies between the experimental data and the

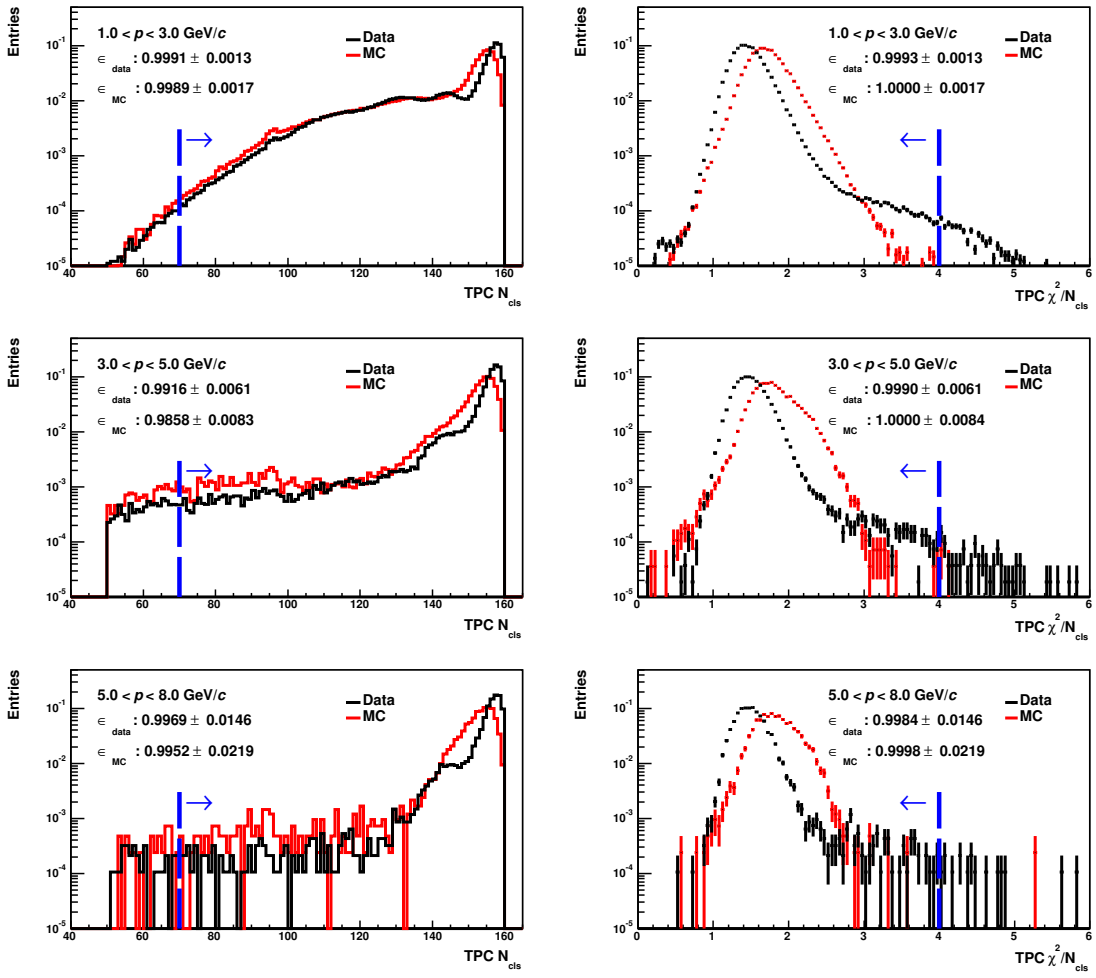

Figure 4.7: Distribution of the number of TPC clusters (left) and TPC χ^2 divided by the number of TPC clusters (right) for electron samples in three momentum ranges. The black lines denote the result of the real data; the red lines, the Monte-Carlo simulation results; and the dashed lines, the thresholds of the track selection cuts.

Monte-Carlo simulation results. However, the applied cuts are are sufficiently weak, i.e., at least 70 clusters out of a maximum 159 hits and χ^2 per TPC clusters needed to be < 4.

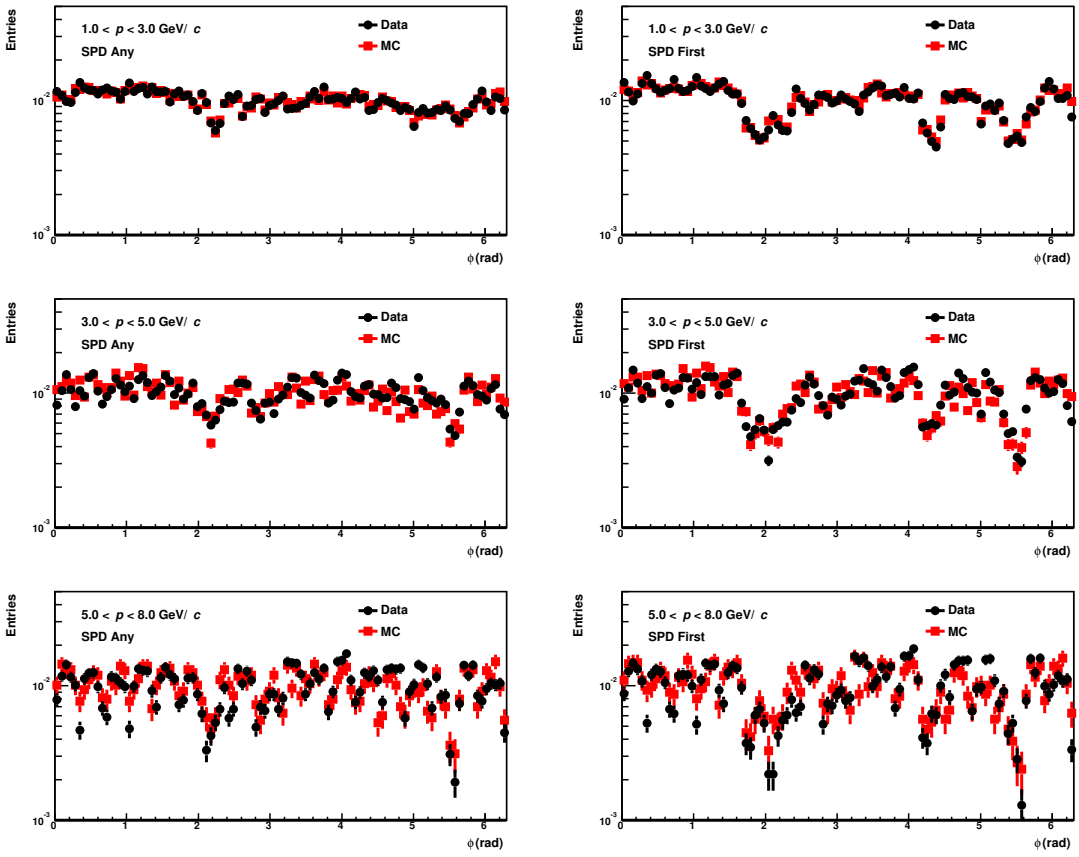

Figure 4.8: ϕ distribution of the electron samples after the "SPD Any" (left) and "SPD First" (right) requirements are included. The black and red markers show the real data and Monte-Carlo simulation results, respectively.

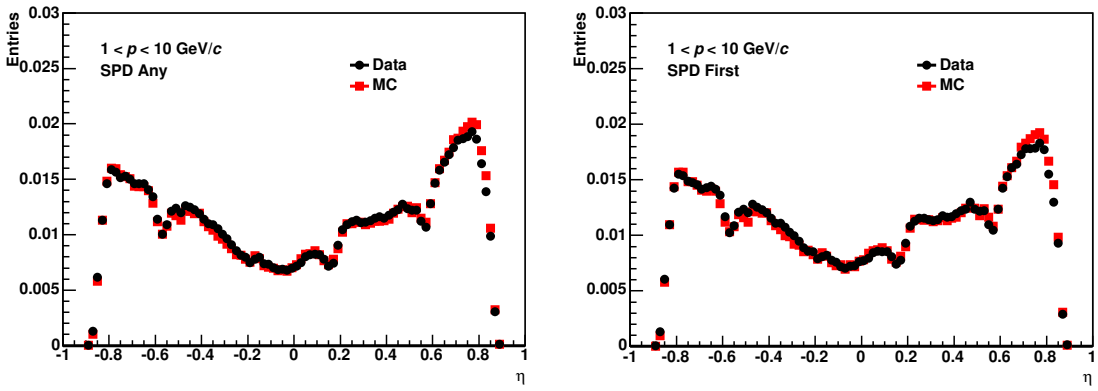

Figure 4.9: η distribution of the electron samples after the requirements "SPD Any" (left) and "SPD First" (right) are included. The black and red markers show the real data and Monte-Carlo simulation results, respectively.

For the rejection of conversion electrons, hits on the SPD layers are required since the conversion electrons generated at large radii such as at the SSD, SDD, and TPC are rejected by this condition. Figures 4.8 and 4.9 show the ϕ and η distributions of the reconstructed tracks after the "SPD Any" and "SPD First" requirements are included. "SPD Any" means that at least one hit on the SPD layers is required, while "SPD First" means that a hit on the first layer of the SPD is required. Good agreement is seen between the analyzed data and the Monte-Carlo simulation results. The "SPD First" requirement

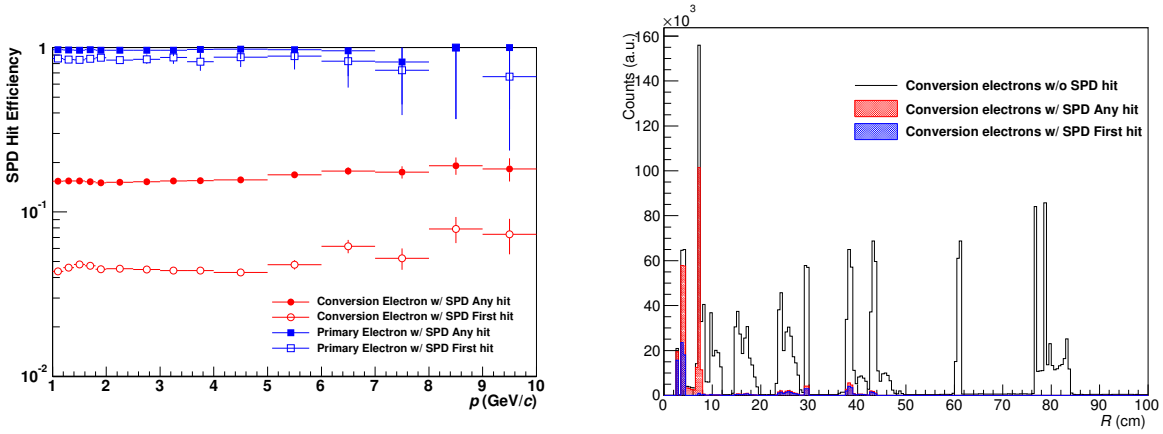

Figure 4.10: SPD hit efficiency of primary and conversion electrons (left) and decay point distribution of conversion electrons reconstructed by the V^0-finder in the Monte-Carlo simulation.

decreases the acceptance due to non-negligible inactive region in the SPD first layer as shownt Fig. 4.10 but it has an advantage that conversion electrons which are created as SDD, SSD, and TPC are efficiently rejected as shown n Fig. 4.10.

Integration time of the SPD is 100 ns, which is shorter than the averaged bunch spacing (200 ns) in p–Pb collisions and therefore, the contribution from the out-of-bunch is negligible with the SPD hit requirement. The cut settings of the SPD hit requirement are summarized in Table. 4.4 in Section 4.4.2.

4.4 Electron Identification

Detector	Momentum range (GeV/c)
ITS	$0.2 < p < 1$
TPC	$0.4 < p < 5$
TOF	$0.4 < p < 3$
TRD	$1.0 < p$
EMCAL	$2.0 < p$

Table 4.2: Typical momentum range for electron identification in the ALICE central barrel.

ALICE has many detectors such as ITS, TPC, TOF, TRD, and EMCal, for electron identification in the central barrel as summarized in Table 4.2. The mean dE/dx in the TPC obeys the Bethe-Bloch formula, as described in Section 3.7. The ALEPH TPC introduced useful parametrization of $\langle dE/dx \rangle$ [106]:

$$\langle \frac{dE}{dx} \rangle_{\text{expected}} = f(\beta\gamma) = \frac{P_1}{\beta^{P_4}} \big(P_2 - \beta^{P_4} - ln(P_3 + \frac{1}{(\beta\gamma)^{P5}}) \big), \tag{4.8}$$

where $P_1, P_2, P_3, P_4,$ and P_5 are known as ALEPH parameters. These parameters are obtained by fitting the experimental momentum-dependent TPC dE/dx distribution. TPC $n\sigma_{\text{ele}}$ is calculated as

$$\text{TPC } n\sigma_{\text{ele}} = \frac{\frac{dE}{dx}^{\text{measured}} - \langle \frac{dE}{dx} \rangle_{\text{expected}}}{\sigma_{\text{ele}}}. \tag{4.9}$$

where σ_{ele} is the resolution of TPC dE/dx for electrons.

4.4.1 Calibration of the TPC PID using Conversion Electrons

Conversion electrons can be obtained by V^0-finder in ALICE. Purity of conversion electrons is high enough to study the electron identification performance. The V^0-finder is used to reconstruct secondary decay vertices (V0) such as Λ, K^0_s, and γ. Figure 4.11 shows schematics of the V0 reconstruction. The V^0-finder calculates the minimum distances between track pairs (DCA_{pair}) to find the secondary decay pairs during track reconstruction.

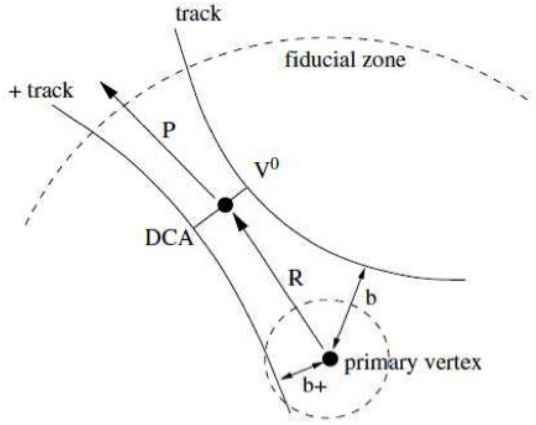

Figure 4.11: Schematics of the V0-finder.

Photon candidates are selected by applying several topological cuts as shown in Table. 4.3. Electron-positron pairs from photon conversions have small opening angle and their pair planes are perpendicular to the magnetic field. The left panel of Fig. 4.12 shows the Almenteros-Podolanski plot for V0 particles the p–Pb collisions. The x-axis is defined

as the longitudinal momentum asymmetry. The y-axis (q_T) is defined as the momentum projection of daughters with respect to the mother p_{T} direction ($p \times \sin\theta_{\mathrm{mother-daughter}}$). Conversion electrons are populated around zero because of the massless photon decays.

Cut	Value
V0 status	On-The-Fly
Minimum leg p_{T}	> 0.05 GeV/c
TPC $N_{cls}/N_{findable}$	> 0.6
R_{conv}	$5 <$ R < 180 cm
Z_{conv}	Z < 240 cm
DCA_{pair}	< 0.25 cm
Ψ_{pair}	< 0.05
$(\alpha/0.95)^2 + (q_{\mathrm{T}}/0.05)^2$	< 1
m_{ee}	< 50 MeV/c^2

Table 4.3: Summary of the conversion electron selections.

Conversion electrons can be selected with high purity ($> 98\%$) in all p_{T} regions as shown in the right panel of Fig. 4.12. The purity is extracted by a full Monte-Carlo simulation with minimum bias events from the DPMJet generator, which reproduced the charged particle multiplicity in p–Pb collisions [107].

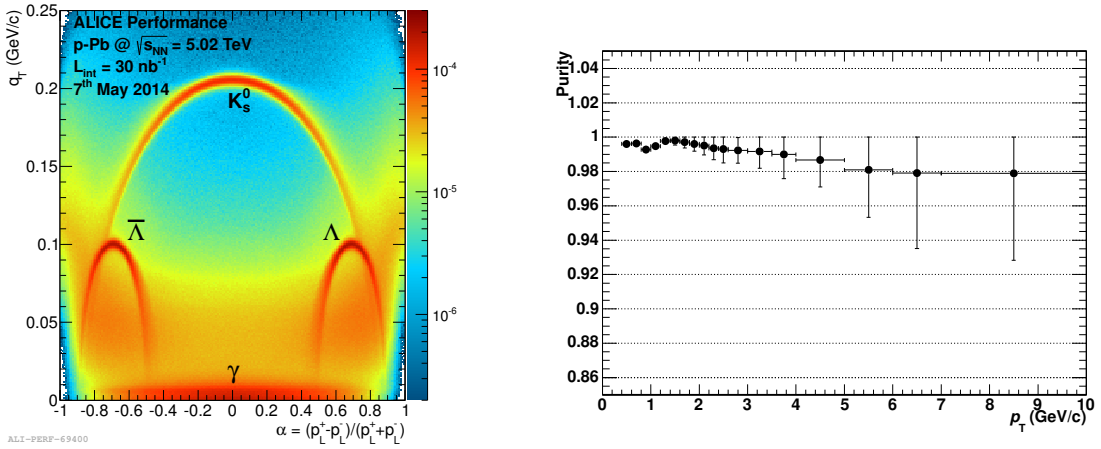

Figure 4.12: Almenteros-Podolanski plot in the p–Pb collision at $\sqrt{s_{NN}}$ =5.02 TeV (Left) and the electron purity of conversion samples extracted by the full Monte-Carlo simulation.

The left panel of Fig. 4.13 shows the η-dependence of the raw TPC dE/dx for conversion electrons. The dE/dx distribution has a strong η dependence because path length in the TPC depends on η. This η dependence is corrected in the calculation of nσ_{ele} as shown in the right of Fig. 4.13. The right panel of Fig. 4.13 shows the η-dependence of the TPC nσ_{ele} distribution after 3-D correction. Figure 4.14 shows the mean of nσ_{ele}, width of nσ_{ele}, and χ^2/NDF by Gaussian fitting of nσ_{ele} as a function of momentum for real data and MC. Good agreement between the measured data and Monte-Carlo simulation is seen.

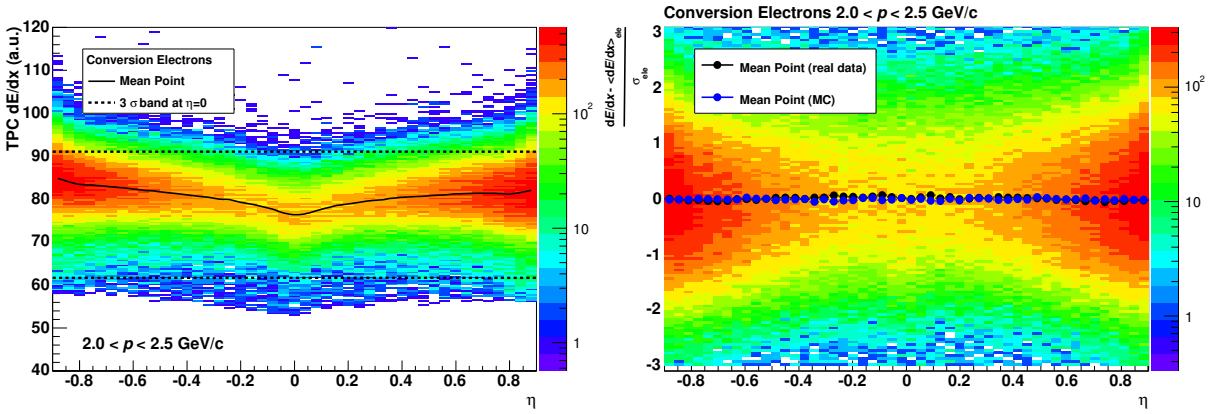

Figure 4.13: η dependence of the raw TPC dE/dx and the TPC nσ_{ele} distribution after spline correction for conversion electrons in the p–Pb collisions (left).

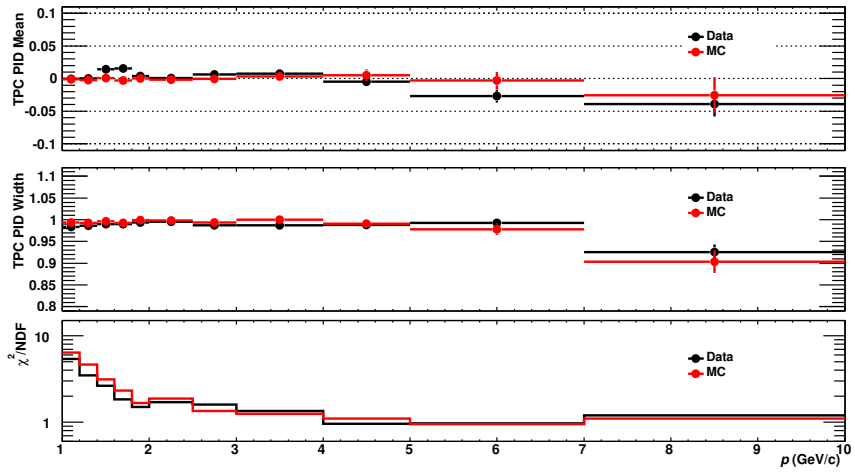

Figure 4.14: Mean, width, and χ^2/NDF of the TPC nσ_{ele} distribution of the conversion electrons. The black and red markers show the results of the analyzed data and the Monte-Carlo simulation results.

4.4.2 Cut Setting of the TPC PID

The first step in electron identification is to select all tracks with a TPC dE/dx within $|\mathrm{n}\sigma_{\mathrm{ele}}| < 3$. The left panel of Fig. 4.15 shows the TPC nσ_{ele} distribution as a function of the reconstructed momentum within $|\mathrm{n}\sigma_{\mathrm{ele}}| < 3$. Large hadron contamination from pions, protons, and deuterons exists when only the inclusion cut is applied. The proton and deuteron bands cross the electron band around 1 GeV/c and 2 GeV/c, respectively. Pions are populated around nσ_{ele} < -1 of Fig. 4.15 and electron and pion bands start to merge at high p_{T} above 4 GeV/c. Figure 4.15 shows the nσ_{ele} cut dependence of the pion contamination as a function of p. To suppress hadron contamination, pion and proton exclusion cuts are applied. The TPC dE/dx bands of pions (nσ_{pi}) and protons (nσ_{pro}) are calculated in the same way as TPC nσ_{ele} with the expected curves of pions and protons. Figure 4.16 shows the TPC nσ_{ele} after applying the pion and proton exclusion

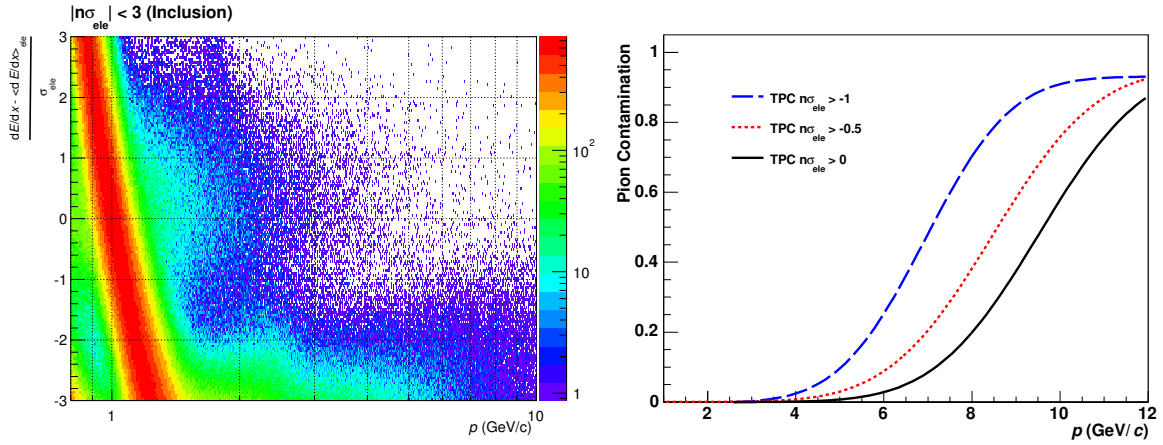

Figure 4.15: TPC n$\sigma_{\rm ele}$ distribution as function of p without hadron exclusion cuts (left) and pion contamination as a function of p with the electron inclusion cuts $\sigma_{\rm ele} > -1$, $\sigma_{\rm ele} > -0.5$, and $\sigma_{\rm ele} > 0$ (right) in the p–Pb collisions.

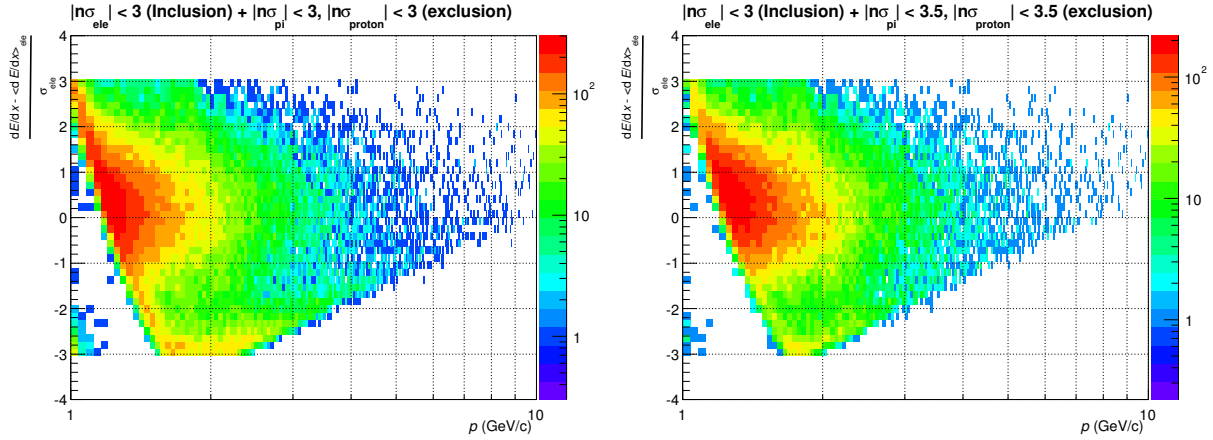

Figure 4.16: TPC n$\sigma_{\rm ele}$ distribution as function of p with $|\sigma_{\rm pi}| < 3$ and $|\sigma_{\rm pro}| < 3$ exclusion cuts (left), and $|\sigma_{\rm pi}| < 3.5$ and $|\sigma_{\rm pro}| < 3.5$ exclusion cuts (right) in the p–Pb collisions.

cuts. Hadron contamination is evaluated by fitting of the TPC n$\sigma_{\rm ele}$ distribution to the templates of each contribution. The electron template is obtained by the conversion electrons and the shape of the deuteron contribution is estimated by the full Monte-Carlo simulation. Their mean and width are fixed and the magnitudes are the only free parameters. The fitting is performed in the electron dominant region (n$\sigma_{\rm ele}$ >1) and the residual components are considered as proton and pion contributions. Examples of the template fitting are shown in Fig. 4.17 and 4.18.

Figure 4.19 shows the hadron contamination with the exclusion cuts $|{\rm n}\sigma_{\rm pi}| < 3.5$, and $|{\rm n}\sigma_{\rm pro}| < 3.5$ and TPC nσ cuts efficiency as a function of the reconstructed momentum. The inclusive hadron contamination is 11% (deuterons: 5%, pions: 4% pions, protons: 2%). Although they contribute to the combinatorial background in the invariant mass distribution of dielectrons, they can be subtracted by the event mixing technique described in the next section. Figure 4.20 shows the measured and simulated single electron iden-

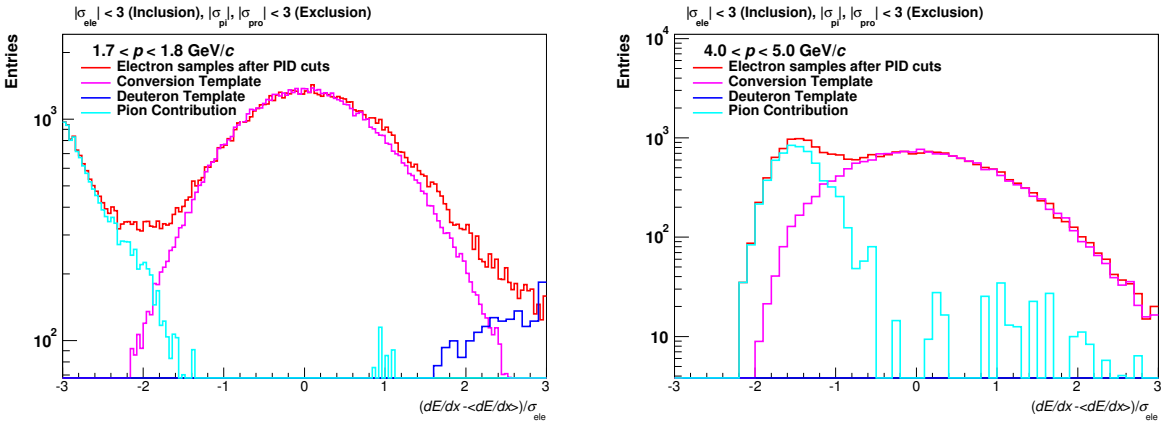

Figure 4.17: The template fitting to the TPC n$\sigma_{\rm ele}$ distributions in the range of $1.7 < p < 1.8$ GeV/c (left) and $4.0 < p < 5.0$ GeV/c (right) with $|\sigma_{\rm pi}| < 3$ and $|\sigma_{\rm pro}| < 3$ exclusion cuts.

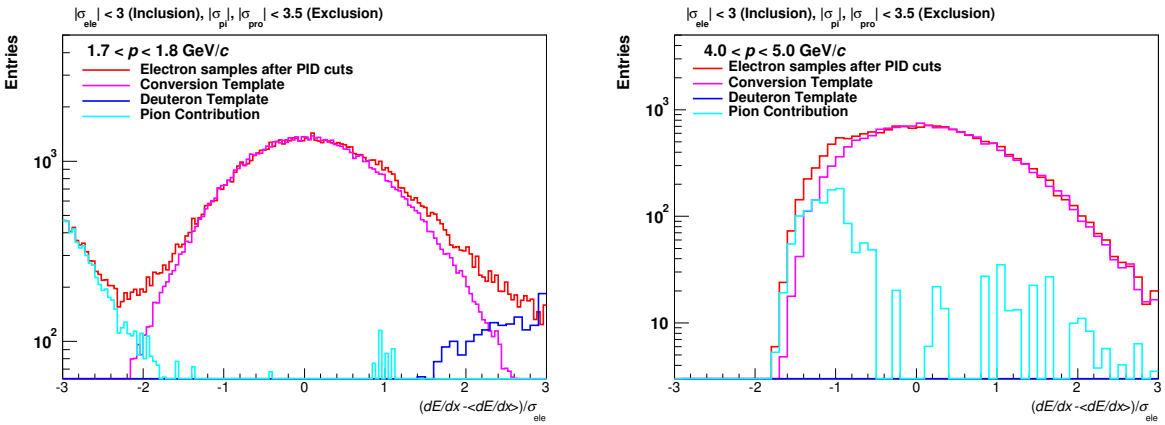

Figure 4.18: The template fitting to the TPC n$\sigma_{\rm ele}$ distributions in the range of $1.7 < p < 1.8$ GeV/c (left) and $4.0 < p < 5.0$GeV/c (right) with $|\sigma_{\rm pi}| < 3.5$ and $|\sigma_{\rm pro}| < 3.5$ exclusion cuts.

tification efficiency as a function of the reconstructed momentum for conversion electrons. Good agreement between the data and Monte-Carlo simulation results is obtained.

The main parameters to be optimized in the J/ψ signal extraction are the leg $p_{\rm T}$, the SPD hit requirement, and the TPC electron identification cuts. A combination of the following cut settings is checked:

Leg $p_{\rm T}$: 0.8, 1.0, 1.1 GeV/c

SPD hit: Any, First

TPC n$|\sigma_{\rm pi}|$ (exclusion): 2.5, 3, 3.5, 4

TPC n$|\sigma_{\rm pro}|$ (exclusion): 3, 3.5, 4

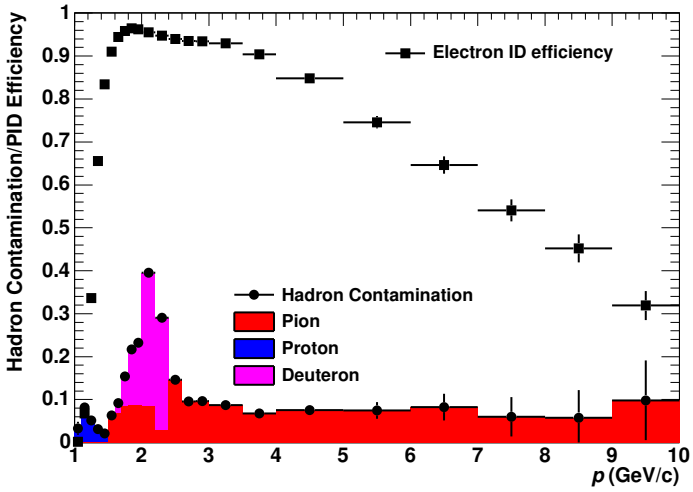

Figure 4.19: Single electron PID efficiency and hadron contamination with pion and proton exclusion cuts $|n\sigma_{pi}| < 3.5$ and $|n\sigma_{pro}| < 3.5$ in the p–Pb collisions at $\sqrt{s_{NN}}$ =5.02 TeV.

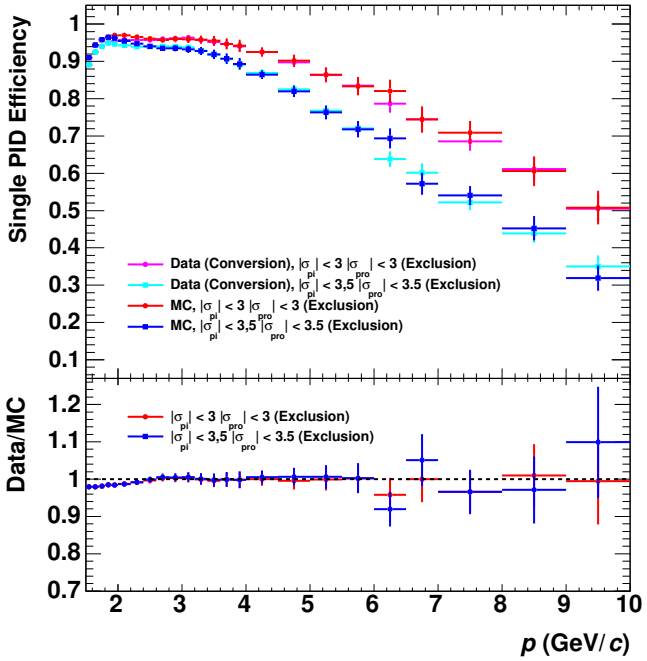

Figure 4.20: Hadron exclusion cut dependence of the single electron identification efficiency (upper) and the ratio of data to Monte-Carlo simulation results (lower) of the p–Pb collisions.

Figure 4.21 shows the signal to background ratio, significance, and χ^2/NDF of the fitting

of the shape obtained by the Monte-Carlo simulation to the reconstructed J/ψ signals in each $p_{\rm T}$ bin for each cut variation. The signal extraction of the J/ψ signals is described in Section 4.6 and the cut index is summarized in Appendix B. At lot $p_{\rm T}$, "SPD First" hit requirement improves the signal to background ratio and the significance. On the other hand, looser cuts showed higher significance as $p_{\rm T}$ increases since background is less at higher $p_{\rm T}$ even with the loose cuts. Table 4.4 shows the summary of the leg $p_{\rm T}$, SPD hit, and TPC PID cut setting.

$p_{\rm T}$ bin (GeV/c)	p_T^e cutoff (GeV/c)	SPD hit	TPC n$\sigma_{\rm pi}$	TPC n$\sigma_{\rm pro}$
0-1.5	1.0	First	3.0	3.5
1.5-3.0	1.0	First	3.5	3.5
3.0-4.5	0.8	Any	3.0	3.5
4.5-6.5	0.8	Any	3.0	3.5
6.5-10.0	1.0	Any	3.0	3.0

Table 4.4: Summary of the cut parameters.

4.5 Rejection of Conversion Electrons

Conversion electrons are the dominant source of electron samples in the whole $p_{\rm T}$ region. Requirement of the first SPD hits significantly reduces conversion electrons, especially, created at the larger radii. However, 25% of the selected electrons are still from conversions at $p_{\rm T}$ = 2 GeV/c as shown in Fig. 4.5. The V^0-finder described in Section 4.4.1 is a powerful tool to identify the conversions. The Monte-Carlo simulation shows that the V0-finder identify 70% of conversion electrons. Figure 4.22 shows e^+e^- pairs (unlike-sign pairs) and uncorrelated background estimated by the event mixing technique, as described in Section 4.6, as a function of the invariant mass with the loose (left) and the tight cuts (right) before (red) and after (black) the V^0-finder cut. At the J/ψ mass, the signal to background ratio is improved by a factor of 50% with the V^0-finder cut without lack of J/ψ signals.

4.6 Signal Extraction

The invariant mass is calculated for all combinations of electron-positron pairs after V^0-finder cuts. The background subtraction is crucial for the raw yield extraction.

4.6.1 Background Subtraction

The unlike-sign pairs around the J/ψ mass contain the following contributions:

- J/ψ signal

- Semi-leptonic decays from $c\bar{c}$ and $b\bar{b}$

- Combinatorial pairs, where both electrons and positrons are completely uncorrelated.

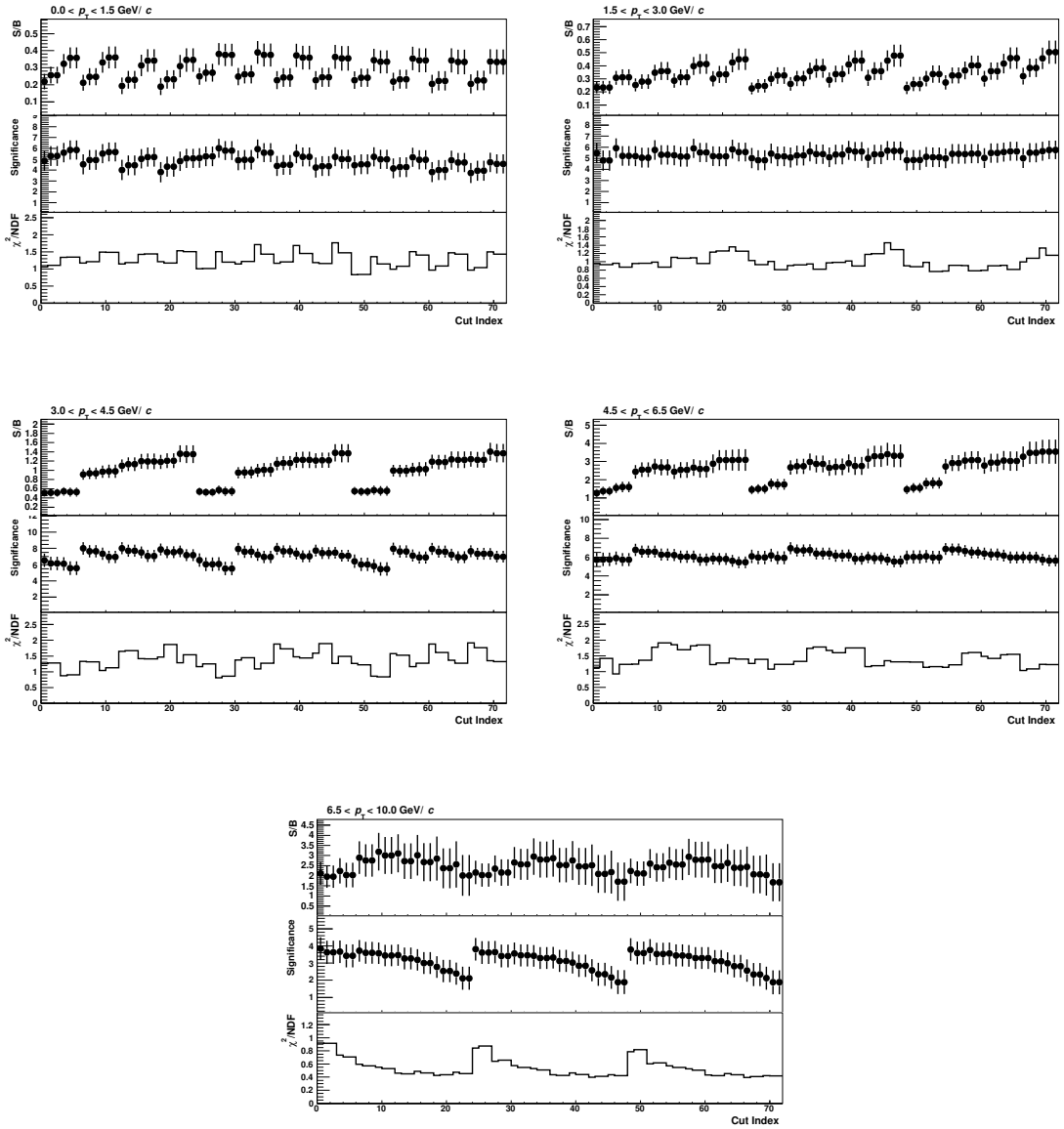

Figure 4.21: Signal to background ratio, significance, and χ^2/NDF of the fitting to the reconstructed J/ψ signals in each p_{T} bin. The cut index is summarized in Appendix B.

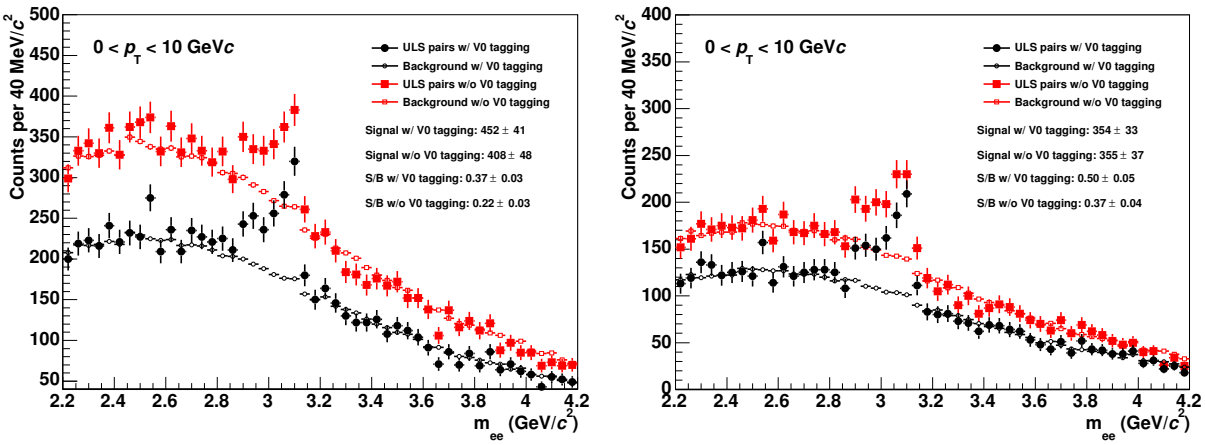

Figure 4.22: Invariant mass spectra of unlike-sign pairs and uncorrelated background pairs estimated by the event mixing before (red) and after (black) V^0-finder cuts. The spectra in the left panel is obtained by the loose cuts ("SPD any", $|n\sigma_{ele}| < 3$, $|n\sigma_{pi}| < 3$, and $|n\sigma_{pro}| < 3$) and the spectra in the right panel is obtained by the tight cuts ("SPD first", $|n\sigma_{ele}| < 3$, $|n\sigma_{pi}| < 3.5$, $|n\sigma_{pro}| < 3.5$).

- Correlated pairs from the fragmentation from jets.

The event mixing technique is used to estimate the shape of the combinatorial background. The procedure of event mixing is as follows:

1. The events that contain electron candidates are stored in the event pools. The event pools are classified according to the collision vertex and centrality (multiplicity):

$$Z_{vtx}\ (\mathrm{cm}) \ = \ \{-10, -7.5, -5, -2.5, 0, 2.5, 5, 7.5, 10\},$$
$$\mathrm{V0M\ Centrality\ (\%)} \ = \ \{0\text{–}20,\ 20\text{–}40,\ 40\text{–}60,\ 60\text{–}80,\ 80\text{–}100\}\ ,$$

   where V0M denotes the centrality of the collisions calculated by the sum of the multiplicities of both V0A and V0C. 9 (Z_{vtx}) × 5 pools have the depth of 10. If each event pool is filled by 10 events, the mixing events are calculated.

2. The invariant mass and pair p_T are calculated for all combinations of selected tracks in the event mixing pool with same Z_{vtx} and multiplicity classes.

3. After event mixing, the corresponding event pool, which is used in procedure 2 is cleaned up (i.e. all stored events are deleted), and the next event processing is started following procedure 1.

Like-sign pairs (e^+e^+, e^-e^-) in the same events include not only the combinatorial background but also correlated background like jet pairs and pairs from $b\bar{b} \to bb$ or $\bar{b}\bar{b} \to ee+X$. Figure 4.23 shows the comparison of the shapes between the like-sign method and the event mixing pairs. Both the like-sign and event mixing pairs are normalized by the side-band yield of unlike-sign pairs (2–2.5, 3.2–3.7 GeV/c^2). The estimated backgrounds

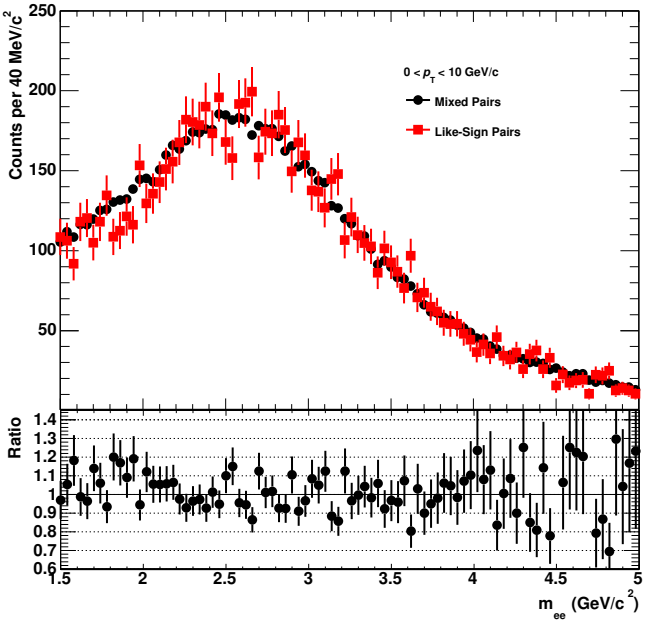

Figure 4.23: Like-sign background and event mixing pairs in the p–Pb collisions (upper) and the ratio of the number of entries between like-sign pairs and event mixing pairs.

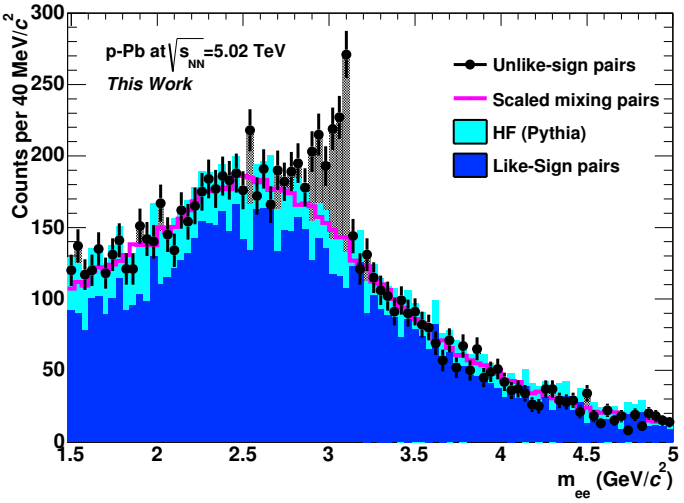

Figure 4.24: p_{T}-integrated unlike-sign pairs, mixing pairs scaled by the side-band yield, and sum of the like-sign pairs and the correlated heavy quark decay pairs estimated by the PYTHIA.

using the like-sign and mixed like-sign pairs show good agreement within 20%, which comes from the statistical uncertainty of the like-sign pairs.

Figure 4.24 shows the inclusive unlike-sign pairs, mixing background normalized by the side-band yields, and the like-sign pairs with the correlated heavy quark decay pairs

as a function of the invariant mass. The correlated heavy quark pairs are estimated by the PYTHIA with the $\sigma_{cc} = 6.9$ mb [108, 109]. The momentum smearing and single electron efficiency are estimated from Monte-Carlo simulations and they are applied to the pairs from PYTHIA to take into account the detector response. Since mixed unlike-sign pairs are consistent with the like-sign pairs + correlated heavy flavor decays, the mixed unlike-sign pairs are used as the background estimator in this analysis.

The line shape of the J/ψ mass is estimated using Monte-Carlo simulation to take into account the momentum resolution and the Bremsstrahlung effect. The left panel of Fig. 4.25 shows $(p_{\rm true} - p_{\rm rec})/p_{\rm true}$ as a function of $p_{\rm rec}$, where $p_{\rm true}$ is the true momentum that electrons have originally when they are generated from the event generator and $p_{\rm rec}$ is the reconstructed electron momentum, respectively. The right panel of Fig. 4.25 shows the input and reconstructed J/ψ mass distributions integrated over $p_{\rm T}$, where $J/\psi \to e^+e^-$ and $J/\psi \to e^+e^-\gamma$ are included.

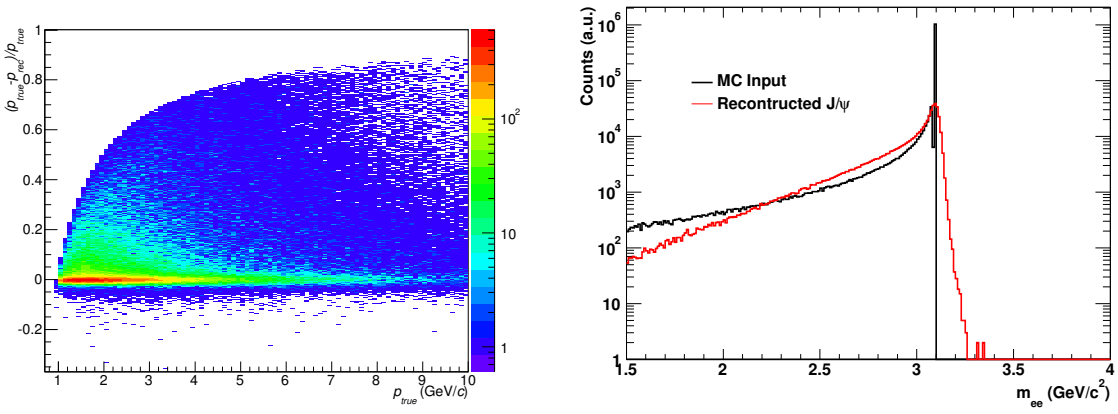

Figure 4.25: Difference between the reconstructed p and true p of single electrons (left) and the comparison of the reconstructed J/ψ mass shape to the MC input mass.

Figure 4.26 shows the $p_{\rm T}$-integrated unlike-sign pairs after background subtraction by mixed unlike-sign pairs. The red solid line shows the fitting result of the signal shape using the line shape obtained from MC. The subtracted mass distribution is in good agreement with the line-shape from MC.

In order to evaluate the systematic uncertainties of the background subtraction, three subtraction methods are applied to take into account the uncertainties of the normalization and background mass shape:

Event mixing scaled by the side bands

The mixing pairs are simply normalized by the yield in the side band region (2.0–2.5, 3.2–3.7 GeV/c^2).

Simultaneous fitting of signal and background

The signal shape is estimated from full Monte-Carlo calculation and the background shape is estimated by the event mixing technique. Background normalization and integral of J/ψ yields are obtained by fitting the mass spectrum from 2 to 4 GeV/c^2.

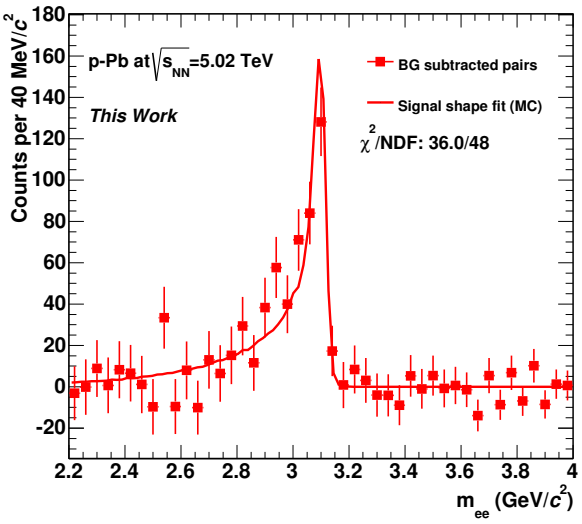

Figure 4.26: Unlike-sign, mixing background, and background subtracted yield. The red solid line is the signal line shape fit.

Different normalization and another fitting procedure

Firstly, mixied unlike-sign pairs are normalized by the like-sign pairs and unlike-sign pairs are subtracted by these scaled mixed unlike-sign pairs. The subtracted yield contained mainly J/ψ signals and correlated $c\bar{c}$ and $b\bar{b}$ pairs. The subtracted yield is fitted by the signal function obtained by full Monte-Carlo simulation and the exponential function:

$$f_{\mathrm{HF}}(m_{ee}) = p_0 e^{-(p_1 m_{ee})^{p_2}} \tag{4.10}$$

At the lowest p_{T} bin, the background shape from heavy quark decays is not exponential because of the leg p_{T} cutoff. Therefore, the power low component is added to the exponential function:

$$f_{\mathrm{HF}}(m_{ee}) = p_0 m_{ee}^{n} e^{-(p_1 m_{ee})^{p_2}} \tag{4.11}$$

Figure 4.27 shows the expected background spectra from heavy quark decays obtained from PYTHIA. The exponential fitting by Eq. 4.10 and Eq. 4.11 shows reasonable agreement. After the subtraction of the exponential component, raw J/ψ signals are obtained.

Figures 4.28, 4.30, and 4.32 show the unlike-sign pairs and the backgrounds using the above three methods. Figures 4.29, 4.31, and 4.33 show the background subtracted yield and the fitting results using the line-shapes from MC from above three methods..

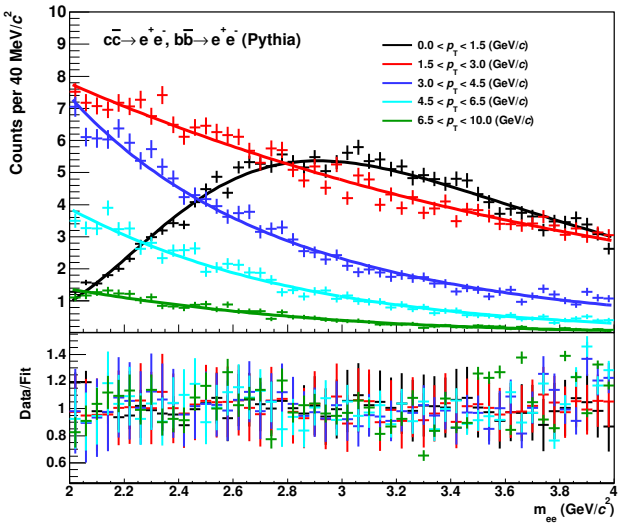

Figure 4.27: Expected background spectra from heavy quark decays obtained by PYTHIA. The solid lines show the results of the fitting. The bottom panel shows the ratio of the data to the fitting function.

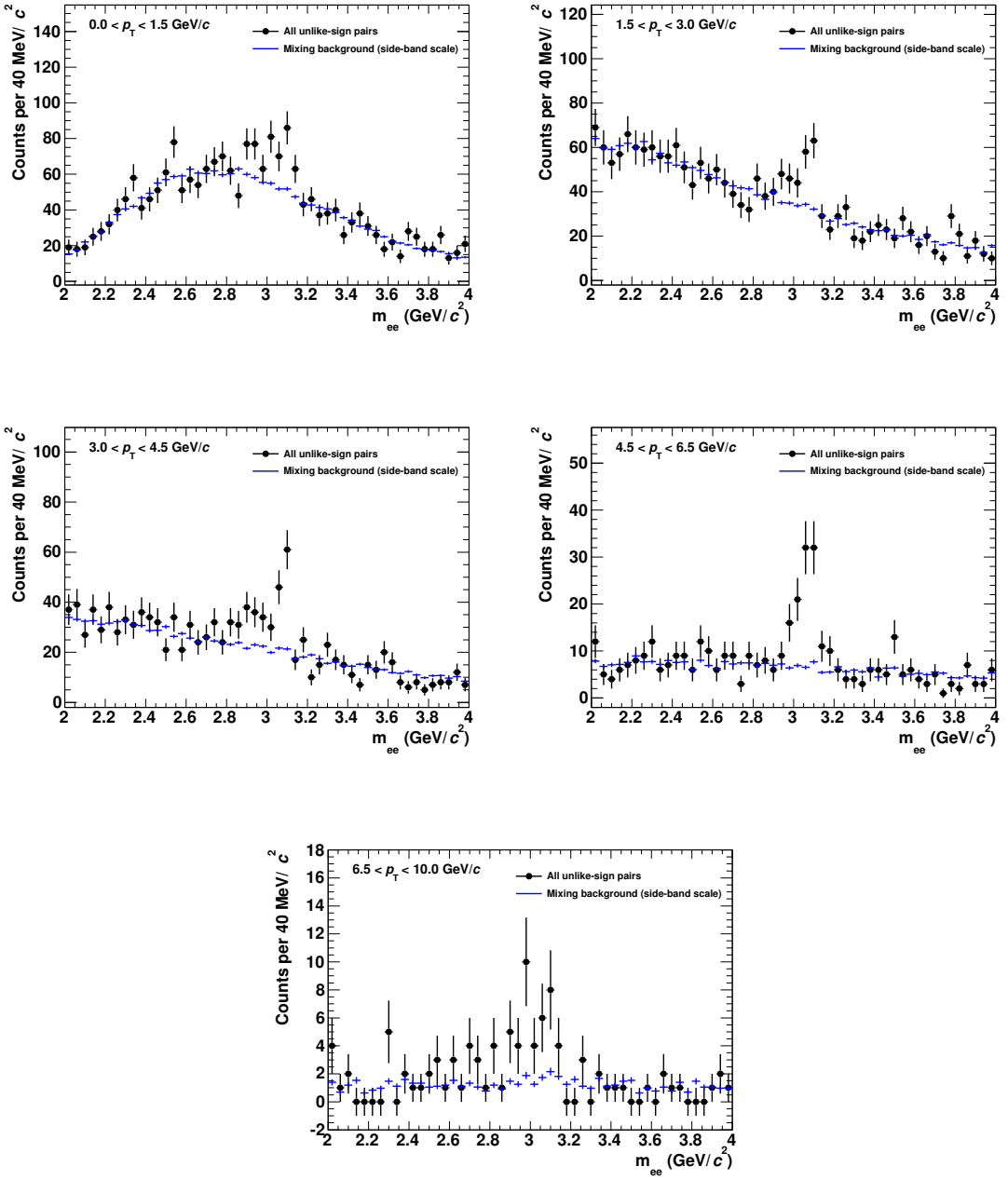

Figure 4.28: Unlike-sign pairs and event mixing pairs normalized by the side-band yields.

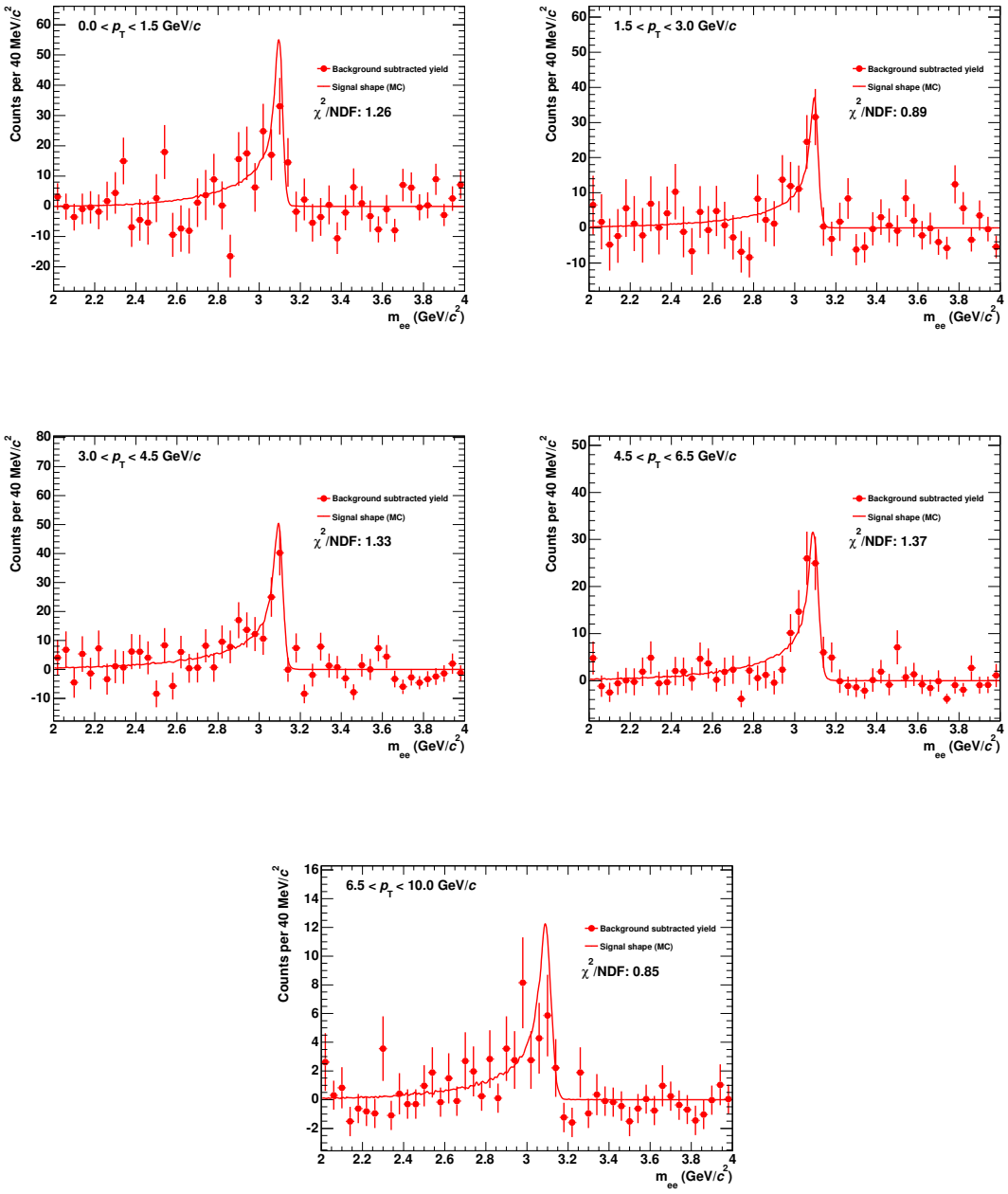

Figure 4.29: Unlike-sign pairs after background subtraction by signal and background fitting and fitting by the line-shape from MC.

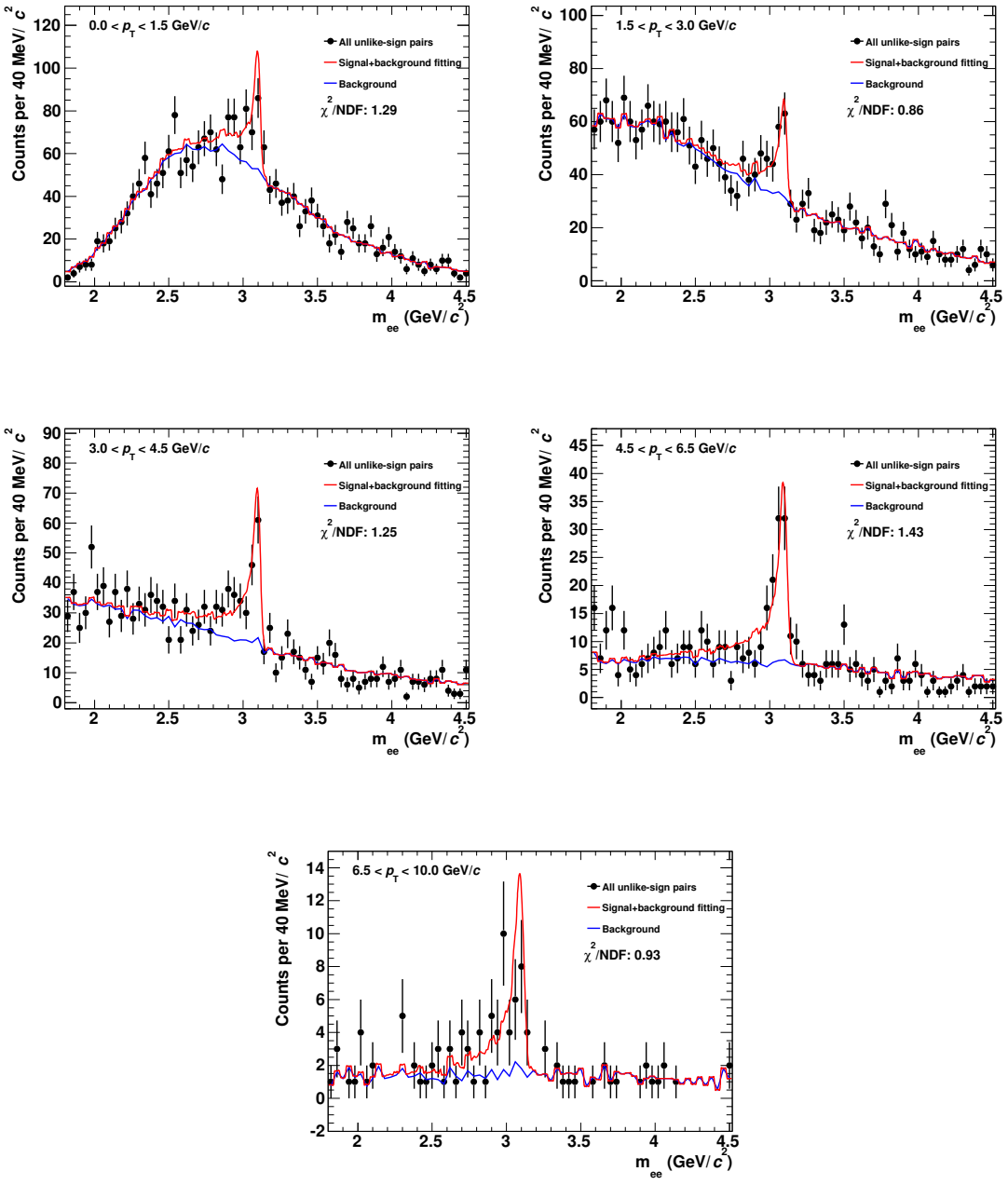

Figure 4.30: Unlike-sign pairs, fitting result of the signal and background. The blue line shows the background composition.

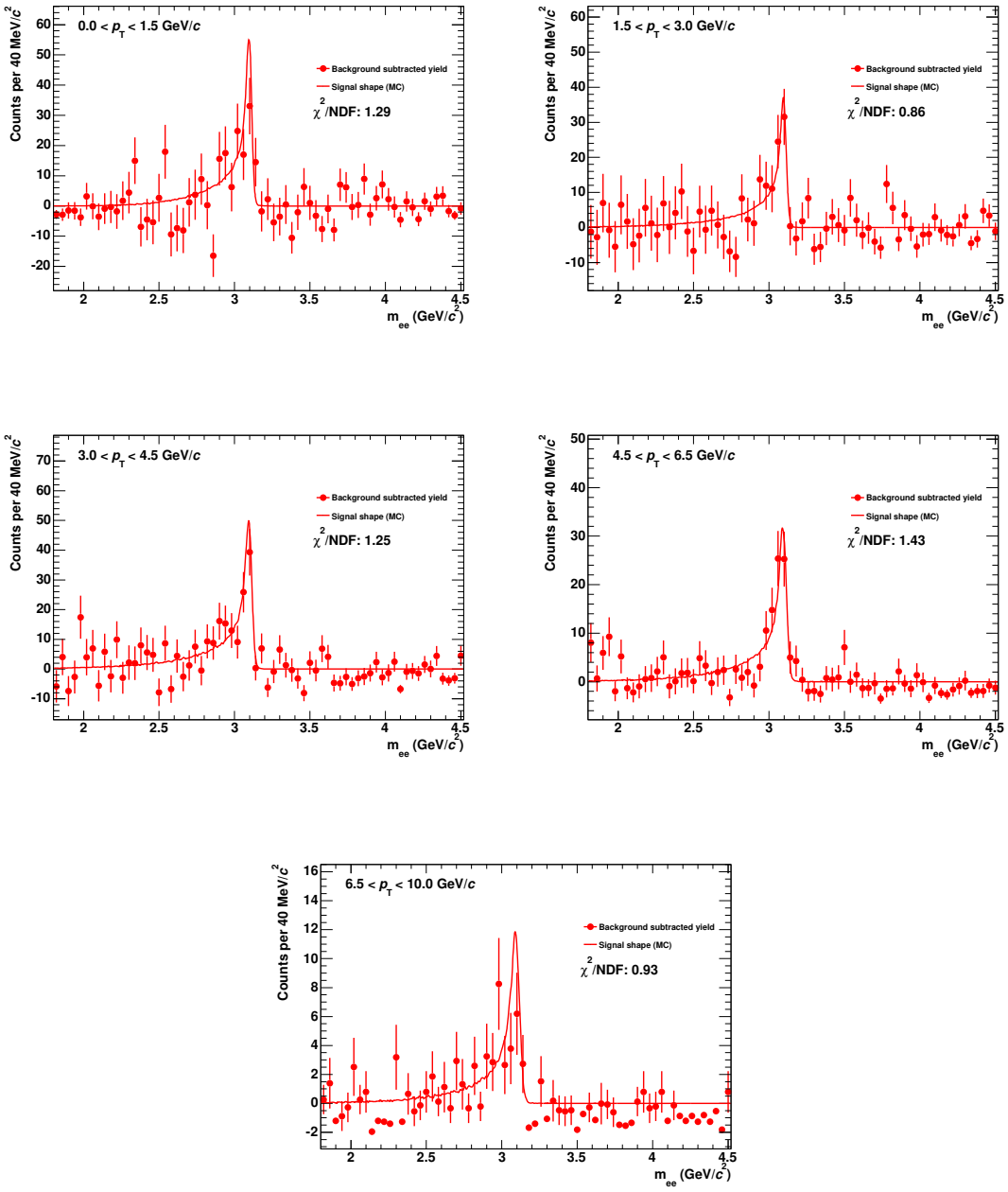

Figure 4.31: Unlike-sign pairs after background subtraction by signal and background fitting and fitting by the line-shape from MC.

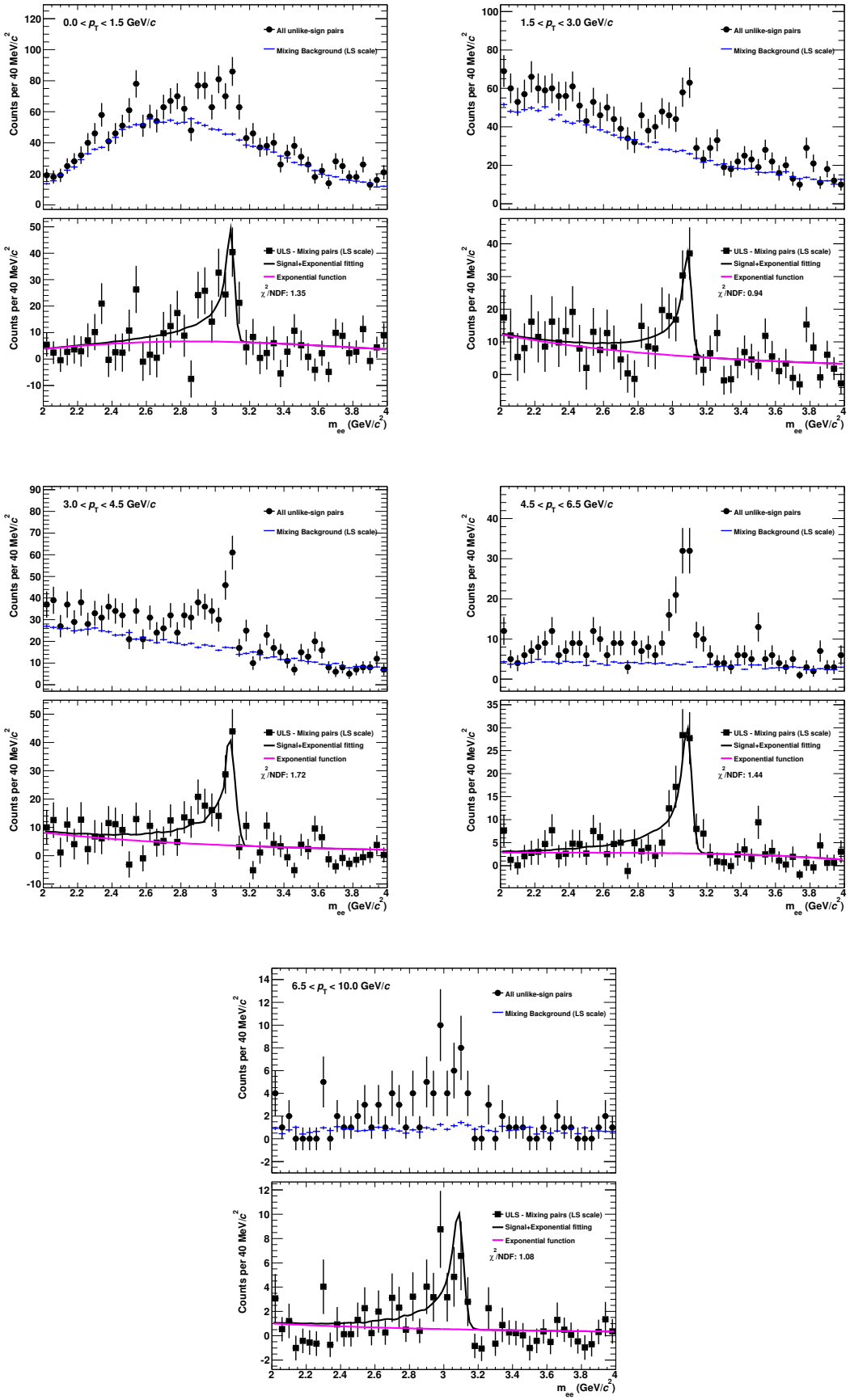

Figure 4.32: Unlike-sign and mixed unlike-sign pairs scaled by the like-sign pairs (top) and unlike-sign pairs after subtraction by mixed unlike-sign pairs (bottom). The black solid curve shows the result of signal and exponential fitting and the magenta curve shows the exponential component of the fitting function.

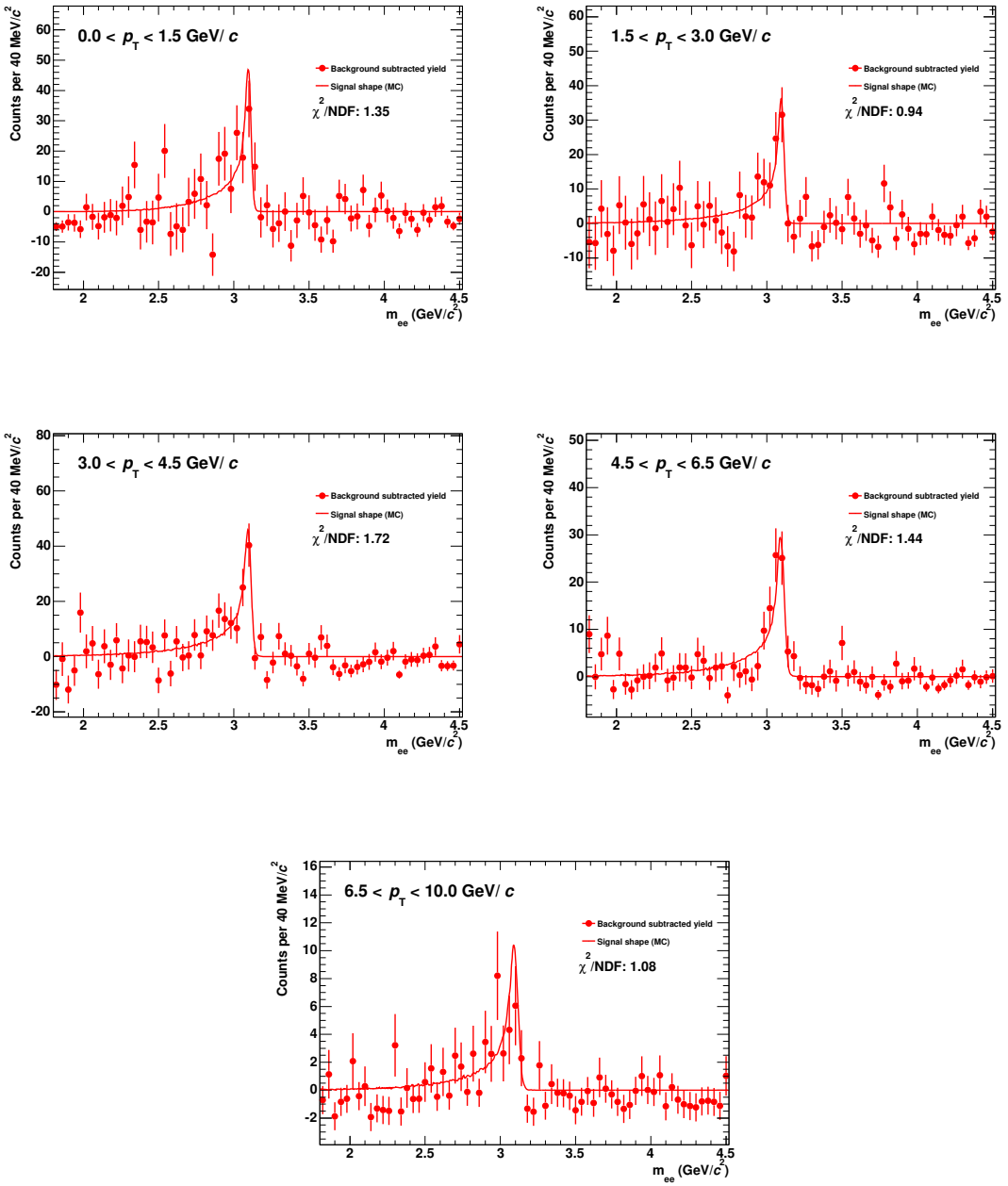

Figure 4.33: Unlike-sign pairs after background subtraction by mixed unlike-sign pairs scaled by the like-sign pairs and exponential fitting and fitting by the line-shape from MC.

4.6.2 Raw Signal Counting

Bin-by-bin counting is performed to extract the number of J/ψ signals. Figure 4.34 shows the lower mass limit dependence of the signal to background ratio and the significance of the J/ψ signals. The significance does not show mass window dependence below 2.9 GeV/c^2, while the signal to background ratio decreases. 2.92 GeV/c^2 is selected as the lower mass limit and the integral of bin contents in $2.92 < m_{ee} < 3.16$ GeV/c^2 is calculated as the number of J/ψ. Figure 4.35 shows the efficiency as a function of lower mass limit. 65–70% of J/ψ is within $2.92 < m_{ee} < 3.16$ GeV/c^2 depending on p_{T} and this is corrected in the extraction of the J/ψ cross section.

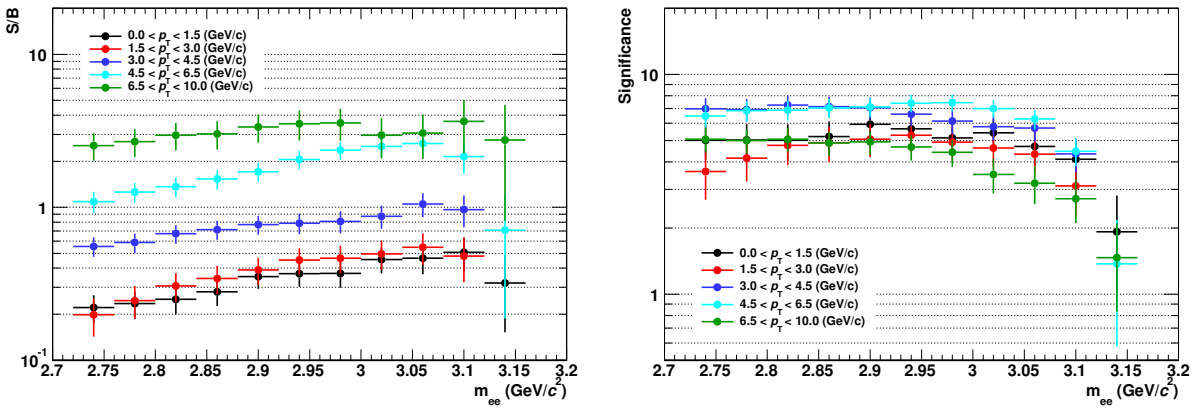

Figure 4.34: Mass window cut dependence of the signal to background and the significance of the J/ψ signals.

Figure 4.36 shows the raw yields of the J/ψ signal by three methods. The central points of the raw yield are from by the simultaneous signal and background fitting method. The RMS from the central points is taken as the systematic uncertainty of the background subtraction. The values of the raw yield, systematic uncertainties, signal to background ratio, significance, and χ^2/NDF are summarized in Table 4.5.

p_{T} bin (GeV/c)	Raw Yield	RMS	Signal/Background	Significance	χ^2/NDF
0–1.5	113 ± 21	2.8	0.34± 0.06	5.4 ± 0.9	1.29
1.5–3.0	93 ± 17	3.5	0.48 ± 0.09	5.5 ± 0.8	0.86
3.0–4.5	101 ± 15	3.2	0.82 ± 0.12	6.8 ± 0.8	1.25
4.5–6.5	84 ± 11	3.5	2.26 ± 0.3	7.6 ± 0.6	1.43
6.5–10.0	26 ± 6	1.7	2.75 ± 0.65	4.4 ± 0.6	0.93

Table 4.5: Summary of the number of reconstructed J/ψ, signal to background ratio, significance, and χ^2/NDF of the signal fitting.

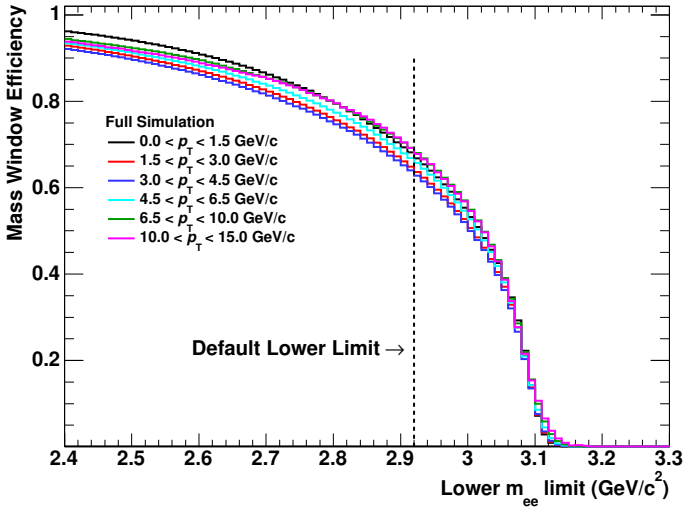

Figure 4.35: Invariant mass window efficiency as a function of the lower mass limit. The higher mass limit is fixed by 3.16 GeV/c^2.

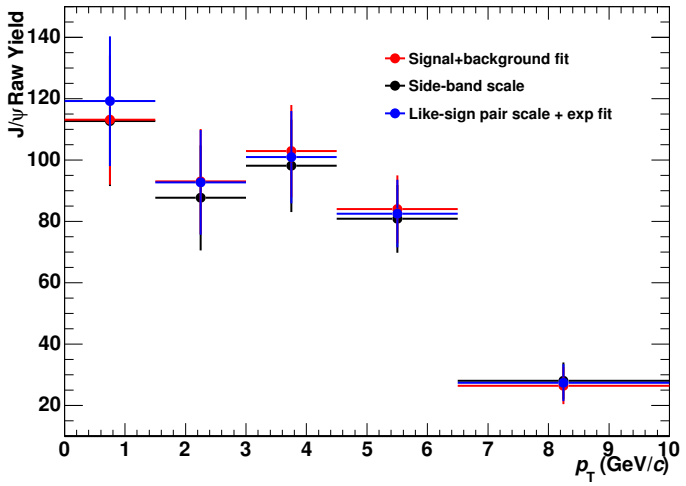

Figure 4.36: Raw counts of the reconstructed J/ψ signals using the three methods of background subtraction.

4.7 Correction Factors

The overall correction factor is

$$\epsilon(p_{\mathrm{T}}) = Acce \times \epsilon_{rec}(p_{\mathrm{T}}) \times C_{corr}(p_{\mathrm{T}}) \times \epsilon_{sel,J/\psi}, \tag{4.12}$$

where $Acce \times \epsilon_{rec}(p_{\mathrm{T}})$ is the acceptance and reconstruction efficiency correction factor described in Section 4.7.2. $C_{corr}(p_{\mathrm{T}})$ is the correction factor for the momentum smearing described in Section 4.7.3.

Since the luminosity is estimated by taking into account the selection of $|Z_{vtx}| < 10$ cm, the efficiency from $|Z_{vtx}| < 10$ cm has to be corrected. Assuming that J/ψ has same Z_{vtx} distribution as primary tracks, the correction factor $\epsilon_{sel,J/\psi}$ is identical to ϵ_{sel} as described in Section 4.1.

4.7.1 Monte-Carlo Simulation

The acceptance and reconstruction efficiency are evaluated using Monte-Carlo simulation. In this analysis, the following Monte-Carlo simulations are performed:

- p–Pb minimum bias production with DPMJet [107].
- Single J/ψ embedded into minimum bias HIJING p–Pb simulations [110].

The input spectrum of J/ψ is the $p_{\rm T}$ distribution as is expected in pp collisions. J/ψ is forced to decay into dielectron channels $J/\psi \rightarrow \gamma e^+e^-$ (radiative decay) using the PYTHIA decayer [108].

Both simulations take into account the material and detector response of the ALICE detectors and are transported in to the GEANT3 simulations [111]. All of the detector calibrations and statistics are anchored by the run condition in the real data set. The latter J/ψ+HIJING production is used for the signal extraction and efficiency calculation. The DPMJet production is used to evaluate the performance of the track quality and electron identification with the conversion electrons which are discussed in Section 4.4.

4.7.2 Acceptance and Efficiency Correction

The detection efficiency including the geometrical acceptance is evaluated as follows:

$$Acce \times \epsilon_{rec} = \frac{\text{The number of reconstructed } J/\psi \text{ in } |y| < 0.9}{\text{The number of generated } J/\psi \text{ in } |y| < 0.9}. \tag{4.13}$$

Figures 4.37 and 4.38 show the kinematic acceptance, track cut efficiency, electron identification efficiency, mass window cut efficiency and overall efficiency of J/ψ as a function of $p_{\rm T}$ and y, respectively. The kinematic acceptance is defined as in Eq. 4.7. The track cut efficiency is defined as the number of J/ψ after the track quality cuts divided by the number of $J/$ after the kinematic acceptance cuts. The PID cut efficiency is defined as the number of J/ψ after the PID cuts divided by the number of $J/$ after the track quality cuts. The mass window cut efficiency is defined as the number of J/ψ after the mass window cuts divided by the number of J/ψ after the PID cuts. The overall efficiency is 5%–20% over the whole $p_{\rm T}$ ranges.

4.7.3 Correction of Momentum Smearing

The reconstructed $p_{\rm T}$ is not the same as the true $p_{\rm T}$ because of detector effects. Therefore, additional correction is needed to extract the invariant spectrum. Figure 4.39 shows the correlation between the reconstructed $p_{\rm T}$ and generated $p_{\rm T}$ of J/ψ using the Monte-Carlo simulation before and after the mass window cut. Before the mass window cut, the

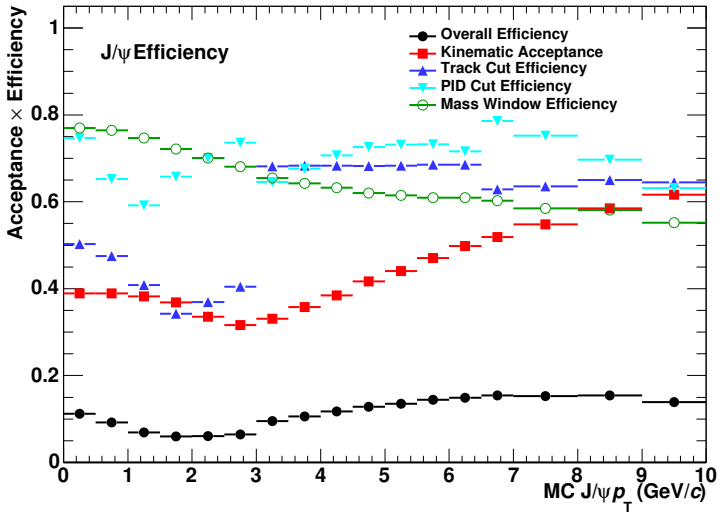

Figure 4.37: Kinematic acceptance, track cut, electron identification, mass window cut, and overall efficiency of J/ψ as a function of p_{T} with the cut sets summarized in Table 4.4. The denominator of every step efficiency, except for the overall efficiency, is the number of J/ψ passing the previous cut stage.

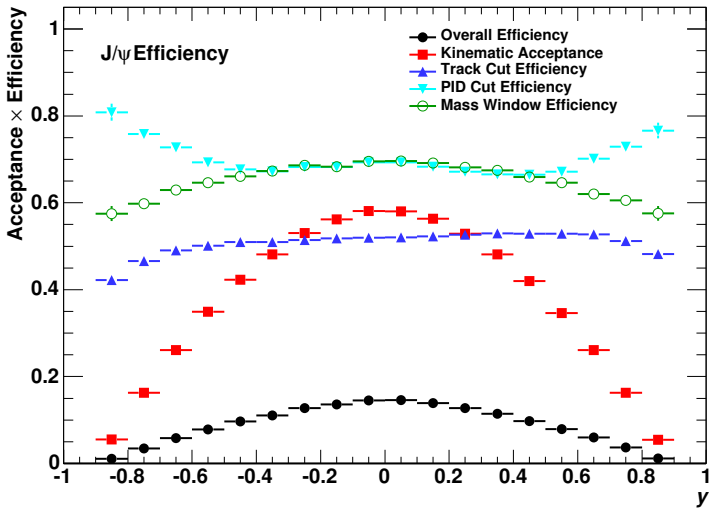

Figure 4.38: Kinematic acceptance, track cut, electron identification, mass window cut, and overall efficiency of J/ψ as a function of y.

correlation is broadened because of the Bremsstrahlung effect. With the mass window cut, the Bremsstrahlung contribution is suppressed and the correlation is dominated by the effect of the momentum resolution. Figure 4.40 shows the comparison between the reconstructed p_{T} and the true p_{T} spectra. The discrepancy is up to 5% at the highest p_{T} bin after the mass window cut. If the input spectrum is close to the true J/ψ spectrum, ratio of the spectrum as a function of reconstructed p_{T} to that as a function of true p_{T} is correction factor, which is due to the momentum smearing effect. The input spectrum

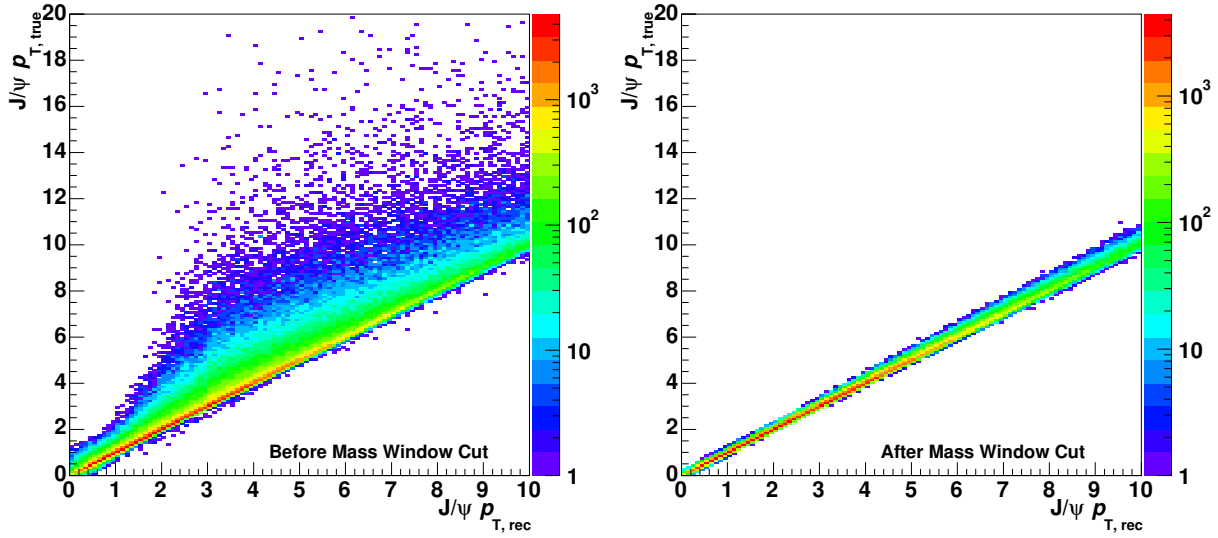

Figure 4.39: Correlation of the p_{T} reconstructed by the detectors and the true p_{T} of J/ψ from the Monte-Carlo simulation.

in the Monte-Carlo simulation is confirmed to show a reasonable agreement with the corrected spectrum (see Fig. 4.41). Therefore the correction factor of the momentum smearing is calculated by

$$C_{corr}(p_{\mathrm{T}}) = \frac{\dfrac{dN_{J/\psi}}{dp_{\mathrm{T,rec}}}}{\dfrac{dN_{J/\psi}}{dp_{\mathrm{T,true}}}}. \tag{4.14}$$

The input J/ψ spectrum affects the reconstruction efficiency and C_{corr}. Following procedure is applied to obtain the true input J/ψ spectrum and related uncertainties. We start using J/ψ spectrum in pp collisions, which is estimated by the interpolation from the several measurements as described in Section 4.9. The $Acce \times \epsilon_{rec}(p_{\mathrm{T}})$ and $C_{corr}(p_{\mathrm{T}})$ are evaluated by using the above interpolated spectrum. After the first correction, the corrected spectrum is fitted with the following function:

$$f(p_{\mathrm{T}}) = C_1 \frac{p_{\mathrm{T}}}{(1 + (\dfrac{p_{\mathrm{T}}}{C_0}^2)^{C_2})}. \tag{4.15}$$

The reconstruction efficiency and C_{corr} are re-evaluated by using new fitted function. The difference between first and second iteration are taken as the systematic uncertainties. The blue line in Fig. 4.41 is the input J/ψ spectrum estimated by the interpolation described in Section 4.9 and the blue markers are the corrected yield by using that input J/ψ spectrum. The red line in Fig. 4.41 shows the fitted J/ψ distribution based on Eq 4.15 and the red markers are obtained if red lines used for reconstruction efficiency and C_{corr} calculations. The lower panel in Fig. 4.41 shows the difference in efficiency$\times$ C_{corr} between the first and second iterations divided by the mean points.

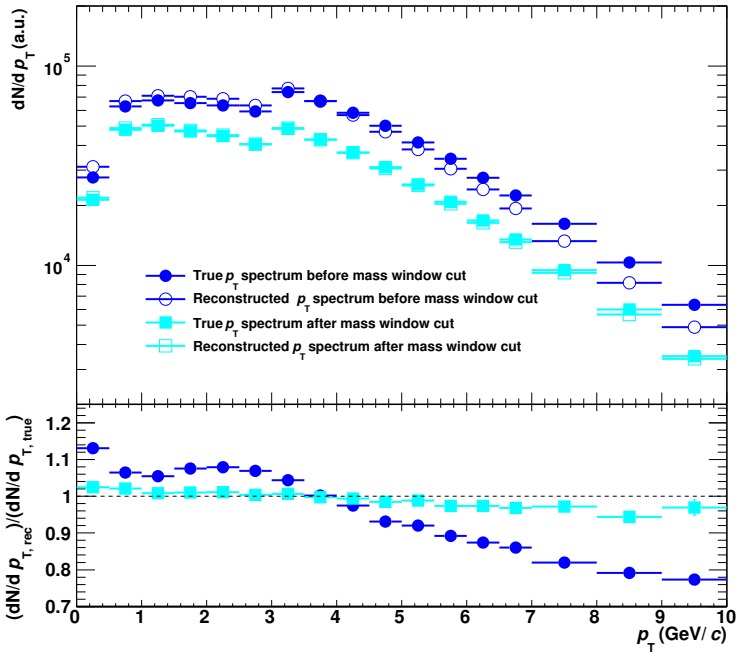

Figure 4.40: Comparison of the reconstructed p_{T} and true p_{T} spectra (upper) and their ratio (lower) in the Monte-Carlo simulation. The blue and cyan markers show the spectra without and with the mass window cut requirement, respectively. The closed markers express the reconstructed p_{T} spectra and the open markers show the true p_{T} spectra.

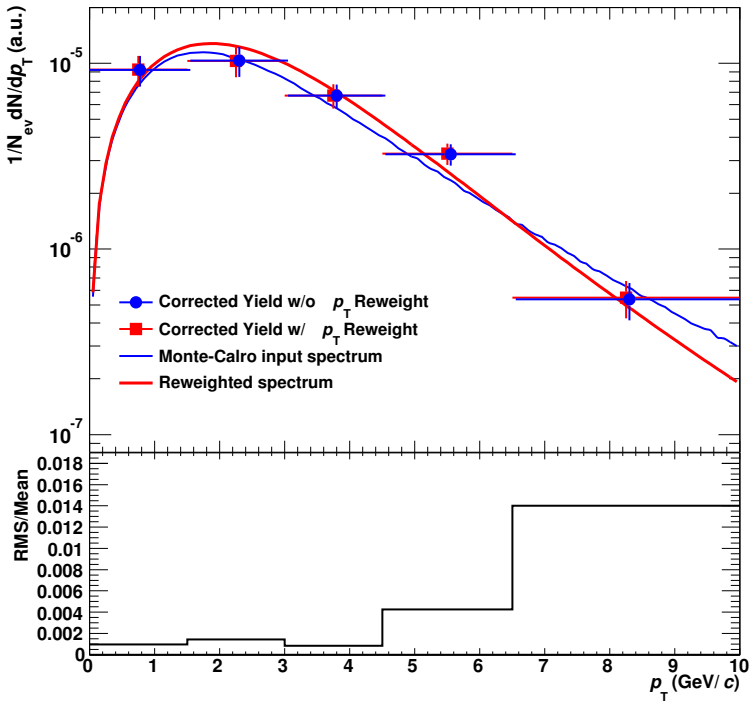

Figure 4.41: Corrected yields, the fitted J/ψ distribution, and the input J/ψ spectra in the Monte-Carlo calculation. The blue line is the input J/ψ spectrum estimated by the interpolation described in Section 4.9 and the blue markers are the corrected yield by using that input J/ψ spectrum. The red line shows the fitted J/ψ distribution based on Eq 4.15 and the red markers are obtained if red lines used for efficiency and C_{corr} calculations. The lower panel shows the difference in efficiency$\times$ C_{corr} between the first and second iterations divided by the mean points.

4.8 Evaluation of Systematic Uncertainties

4.8.1 Track Reconstruction and Electron Identification

The following variations are taken to extract the systematic uncertainties of the track quality cuts:

- The number of TPC clusters: 60, 70 (default), 80, 100.
- TPC χ^2 per number of clusters: 3.5, 4 (default), 4.5.

This study is performed in the p_{T}-integrated bin to reduce the statistical fluctuation. The RMS of these variations is taken as the systematic uncertainty. For electron identification, the following variation is considered and the RMS of these variations is calculated as the systematic uncertainty:

- TPC inclusion cut ($\mathrm{n}\sigma_{\mathrm{ele}}$): 2, 3, 3.5.
- TPC pion exclusion cut ($\mathrm{n}\sigma_{\mathrm{pi}}$): (default cut values in Table 4.4) $\pm$ 0.5.
- TPC proton exclusion cut ($\mathrm{n}\sigma_{\mathrm{pro}}$): (default cut values in Table 4.4) $\pm$ 0.5.

Figure 4.42 shows the efficiency of the track quality and electron identification cut variation. The efficiency variation is large compared to the extracted systematic uncertainties summarized in Table 4.6.

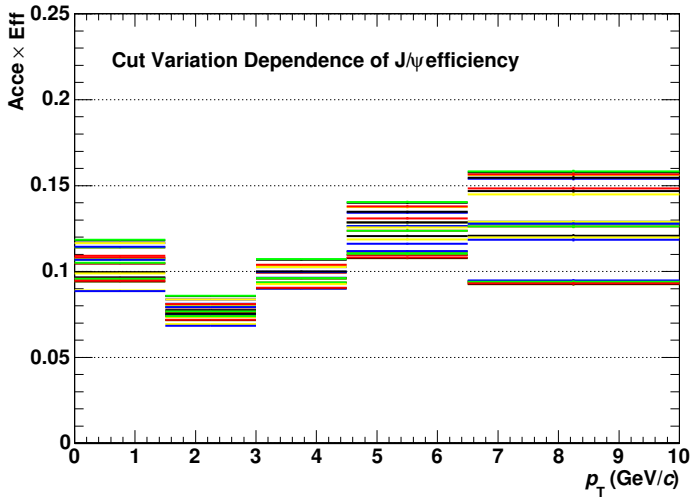

Figure 4.42: The efficiency distribution of the track quality and electron identification cut variations (4 TPC N_{cls} $\times$ 3 TPC χ^2/N_{cls} cut variation and 3 TPC $\mathrm{n}\sigma_{\mathrm{ele}}\times$ 3 TPC $\mathrm{n}\sigma_{\mathrm{pi}}\times$ 3 TPC $\mathrm{n}\sigma_{\mathrm{pro}}$ cuts variation).

4.8.2 Signal Extraction

The three methods are employed in the study of systematic uncertainty, as described in Section. 4.6.1. The RMS of these methods is taken as the systematic uncertainty.

Mass Window Cut

The following cuts are applied and the RMS of all combinations is taken as the systematic uncertainty:

- Lower limit: 2.84, 2.92 (default) , 3.0 (GeV/c^2).

- Higher limit: 3.12, 3.16 (default), 3.2 (GeV/c^2).

In order to suppress statistical fluctuation, 3–10 GeV/c bins are merged to extract the uncertainty. Figure 4.43 shows the corrected spectra of the mass window cut variation. From Fig. 4.35, the efficiency variation with the above cut variation is larger than 8%. This variation is large compared to the systematic uncertainties of the mass window cuts summarized in Table 4.6.

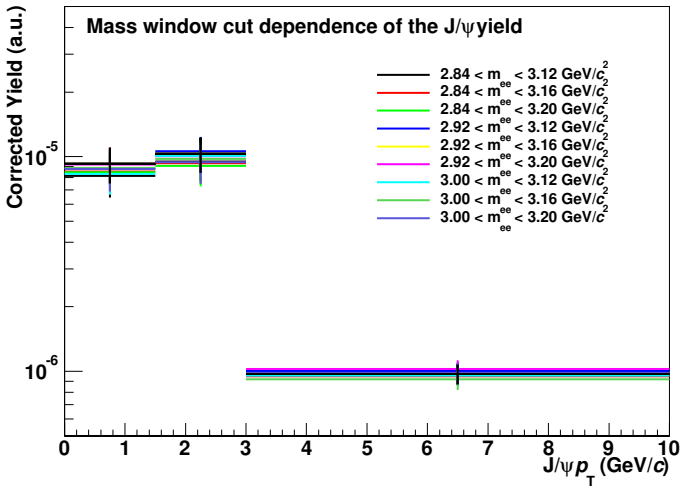

Figure 4.43: Mass window cut dependence on the corrected yields of J/ψ.

4.8.3 Monte-Carlo Weighting

As described in Section 4.7, two p_{T} weighting functions are checked for the efficiency evaluation. The RMS of the efficiency with these input spectra is taken as the systematic uncertainty of the input p_{T} spectrum as shown in Fig. 4.41.

4.8.4 Global Uncertainty

The following normalization uncertainties are considered to extract the cross section and R_{pPb}:

- Trigger efficiency correction for NSD events: 1.037 ± 0.042 [105].

- Minimum bias event cross section (σ_{V0}) in ALICE: 2.09 ± 0.07 b [113].

- Branching ratio of $J/\psi \rightarrow e^+e^-$: 5.94 $\pm$ 0.06 % [1].

- $T_{\rm pPb}$: 0.0983 $\pm$ 0.0035 mb^{-1} [104].

They are fully correlated among all $p_{\rm T}$ bins. The systematic uncertainties of $\sigma_{\rm V0}$ and $T_{\rm pPb}$ are also correlated with respect to the dimuon measurement at forward and backward rapidity in the ALICE [114]. The backward rapidity measurement is performed in opposite colliding mode ('Pb–p') and σ_{V0} is estimated by corresponding van der Meer scan, while forward and mid-rapidity measurements are done in 'p–Pb' mode.

4.8.5 Summary of Systematic Uncertainties

The systematic uncertainties described above are summarized in Table. 4.6.

$p_{\rm T}$ bin (GeV/c)	0-1.5	1.5-3	3-4.5	4.5-6.5	6.5-10
Track cuts	1.3%	1.3%	1.3%	1.3%	1.3%
PID cuts	3.6%	3.6%	4.2%	4.2%	2.4%
Background subtraction	2.4%	3.8%	3.2%	4.2%	6.4%
Mass window cut	3.2%	5.5%	3.9%	3.9%	3.9%
MC weighting	0.4%	0.1%	0.1%	0.5%	1.4%
Total	7%	7%	6%	7%	8%
Normalization					
Trigger efficiency for NSD	3.2 %	3.2%	3.2%	3.2%	3.2%
MB cross section	3.4%	3.4%	3.4%	3.4%	3.4%
Branching ratio	1.0%	1.0%	1.0%	1.0%	1.0%
$T_{\rm pPb}$	3.4%	3.4%	3.4%	3.4%	3.4%

Table 4.6: Summary of the relative systematic uncertainties.

4.9 Extraction of the pp Reference Spectra

It is very important to compare the results with the pp reference data for the study of normal nuclear matter effects. Unfortunately, there is no experimental measurements for pp collisions at $\sqrt{s_{NN}} = 5.02$ TeV. The interpolation procedure used in this analysis is taken from [112]. First, the double differential cross sections ($d^2\sigma_{J/\psi}/dp_{\rm T}dy$) in pp collisions measured by PHENIX, CDF, CMS, LHCb, and ALICE are normalized by the inclusive cross section ($d\sigma_{J/\psi}/dy$) so that the $p_{\rm T}$-integrated cross section is unity. Next, the transformation of $p_{\rm T} \rightarrow p_{\rm T}/\langle p_{\rm T}\rangle$ is performed in order to approach universal behavior. The statistical and systematic uncertainties for all the observables are summed in quadrature. The scaled spectra are fitted with the following empirical function:

$$\frac{\langle p_{\rm T}\rangle}{(d\sigma_{J/\psi}/dy)}\frac{d^2\sigma}{dp_{\rm T}dy} = \frac{2(n-1)B^2 p_{\rm T}/\langle p_{\rm T}\rangle}{(1+B^2(p_{\rm T}/\langle p_{\rm T}\rangle)^2)^n}, \tag{4.16}$$

where B is $\Gamma(3/2)\Gamma(n-3/2)/\Gamma(n-1)$. Figures 4.44 and 4.45 show the results of the fitting based on Eq. 4.16 and the ratio of the fit to the experimental data, respectively. n is determined as 3.79 ± 0.07 with $\chi^2/\mathrm{NDF} = 0.6$. The determination of the systematic uncertainties in the fit procedure is evaluated by excluding the experimental results one by one for a given energy and performing the its.

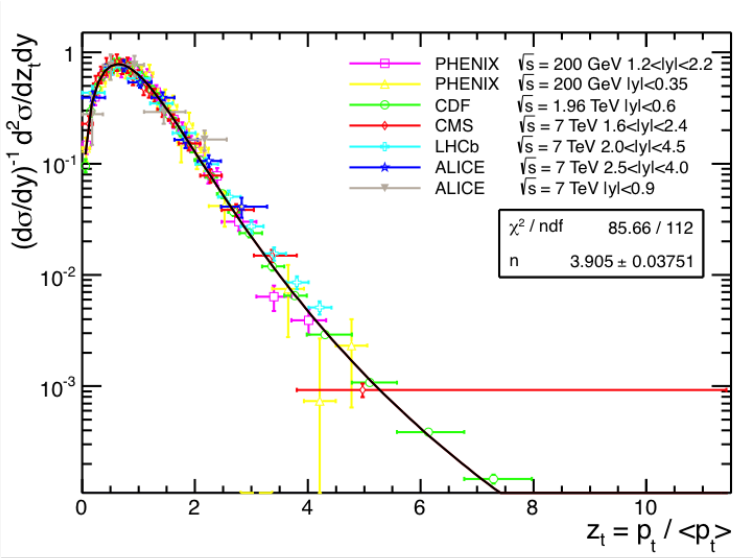

Figure 4.44: Scaled fit of the experimental results to several measured spectra in PHENIX, CDF, MCS, LHCb, and ALICE [112].

In order to interpolate the pp reference spectrum, the estimation of the total cross section and mean $p_{\rm T}$ are needed. The $\sqrt{s}$ dependency of $\langle p_{\rm T}\rangle$ is calculated by fitting with the power-law function to extract $\langle p_{\rm T}\rangle$ at $\sqrt{s} = 5.02$ TeV. The inclusive J/ψ cross section at mid rapidity is extracted by power-law fitting and FONLL prediction approaches, and the prediction based on the leading order color evaporation model. Figure 4.46 shows the energy dependence of the J/ψ cross section and the fitted results based on the FONLL

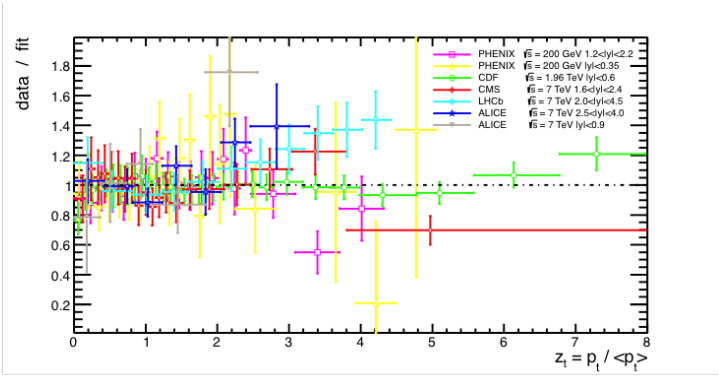

Figure 4.45: Ratio of the data to the scaled fit function [112].

calculation. The interpolated cross section is

$$BR(J/\psi \to ee) \times d\sigma_{J/\psi}/dy_{y\sim 0,\sqrt{s}=5.02TeV} = 368 \pm 36\ (\text{stat}) \pm 49\ (\text{syst})\ \text{nb}. \quad (4.17)$$

The rapidity-dependence is negligible compared to other uncertainties. The interpolated

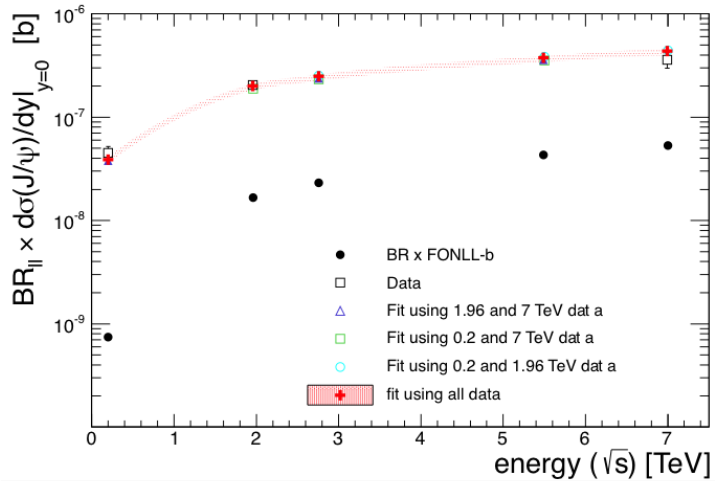

Figure 4.46: Energy dependence of the J/ψ cross section fitted using FONLL calculation [112].

values are summarized in Table. 4.7. Both the statistical and systematic uncertainties are propagated as a systematic uncertainty of the pp reference.

The central points of the p_{T} differential pp reference are calculated using $\langle p_{\mathrm{T}} \rangle = 2.771$ GeV/c and $n = 3.79$. The uncorrelated uncertainty is determined by the spectra calculated with the upper and lower limits of the uncertainties of $\langle p_{\mathrm{T}} \rangle$ and n as shown in Fig. 4.47. The systematic uncertainties are evaluated as the RMS of these variations.

The systematic uncertainties of the pp reference are summarized in Table 4.8. The global uncertainty is defined as the uncertainty of the interpolated total J/ψ cross section. Figure 4.48 compares the interpolated pp reference J/ψ spectrum at $\sqrt{s} = 5.02$ TeV and

Rapidity	$d\sigma_{J/\psi}/dy(\mu\mathrm{b})$	$\langle p_{\mathrm{T}}\rangle$
$\lvert y\rvert$ <0.9	6.192±0.613±0.824	2.771±0.095±0.106
2.5< y <4	5.272±0.363±0.105	2.424±0.029±0.024

Table 4.7: Interpolated $d\sigma_{J/\psi}/dy$ and $\langle p_{\mathrm{T}}\rangle$ in the pp collisions at $\sqrt{s}$ =5.02 TeV.

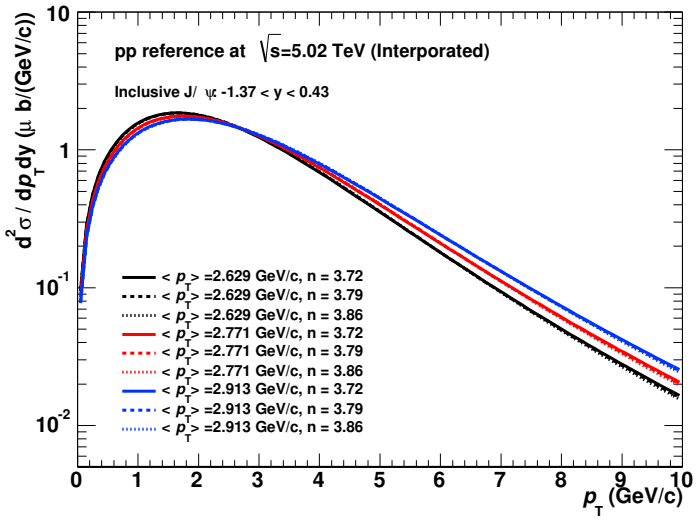

Figure 4.47: Systematic study of the $\langle p_T\rangle$ and n variation dependence of the interpolated pp reference spectrum at $\sqrt{s}$ =5.02 TeV.

p_{T} bin (GeV/c)	0-1.5	1.5-3	3.0-4.5	4.5-6.5	6.5 -10
Uncorr. syst.	6.8%	2.1%	4.2%	9.9%	15.1%
Global syst.	16.5%	16.5%	16.5%	16.5%	16.5%

Table 4.8: Summary of the systematic uncertainties of the pp reference data. The global uncertainty is from the determination of $d\sigma_{J/\psi}/dy$.

$\sqrt{s}$ = 2.76 TeV to the measured spectra at different energies. The bands of the spectra include both correlated and uncorrelated uncertainties.

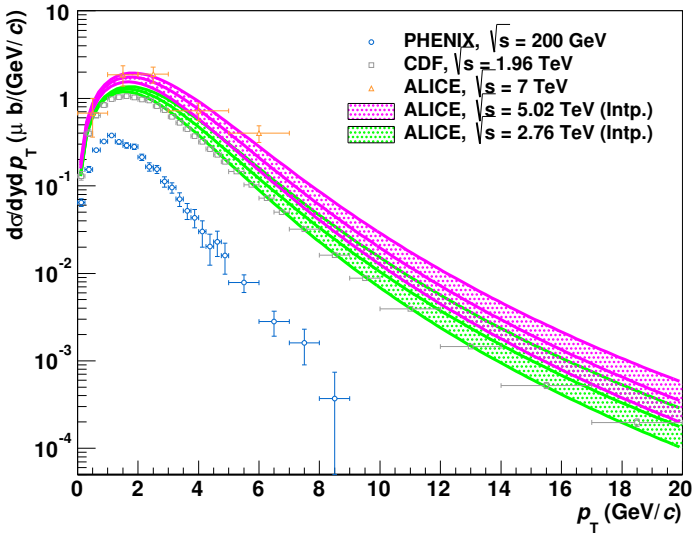

Figure 4.48: Experimental and interpolated spectra in pp collisions [112]. The magenta and green bands shows the interpolated J/ψ spectra in the pp collisions at $\sqrt{s_{NN}} = 5.02$ TeV and $\sqrt{s_{NN}} = 2.76$ TeV, respectively.

Chapter 5

Results and Discussion

5.1 Results

5.1.1 Cross Section of J/ψ production in p–Pb collisions

The measured production cross section of the inclusive J/ψ at mid-rapidity (-1.37 $< y_{\rm CMS}$ < 0.43), shown in Fig. 5.1, is

$$\frac{d\sigma_{J/\psi}}{dy} = 930 \ \pm 83 \ (\text{stat}) \ \pm \ 59 \ (\text{uncorr.syst}) \ \pm \ 45 \ (\text{corr.syst}) \ \mu\text{b}. \qquad (5.1)$$

The latter 2 components are the uncorrelated and correlated systematic uncertainties with respect to the uncertainties of the dimuon ($\mu^+\mu^-$) decay measurements at forward rapidity, respectively [114]. The shaded boxes represent the sum in quadrature of the partially correlated and fully correlated uncertainties. In the dimuon measurements, the sources of the partially correlated and correlated uncertainties are as follows:

- Partially correlated uncertainty: Cross section of the minimum bias trigger

- Correlated uncertainty: Branching ratio

Since the forward and backward rapidity measurements via the dimuon decay are performed in the 'p–Pb' and 'Pb–p' modes[1], respectively. The minimum bias triggered cross sections for p–Pb and Pb–p collisions are determined via corresponding van der Meer scans. The systematic uncertainties of σ_{V0} in p–Pb and Pb–p collisions are partially correlated because the same detectors (V0A and V0C) are used for the minimum bias trigger decision. In the dielectron analysis, the systematic uncertainties of the minimum bias trigger cross section and the branching ratio are correlated with respect to the uncertainties of the dimuon measurements.

Figure 5.2 shows the invariant production cross section of the inclusive J/ψ as a function of $p_{\rm T}$. The open and shaded boxes represent the uncorrelated and correlated systematic uncertainties, respectively. The values of the cross section, the statistical uncertainty, and the systematic uncertainties are summarized in Table. 5.1. From the $p_{\rm T}$ spectrum,

[1]Defined in Section 3.9

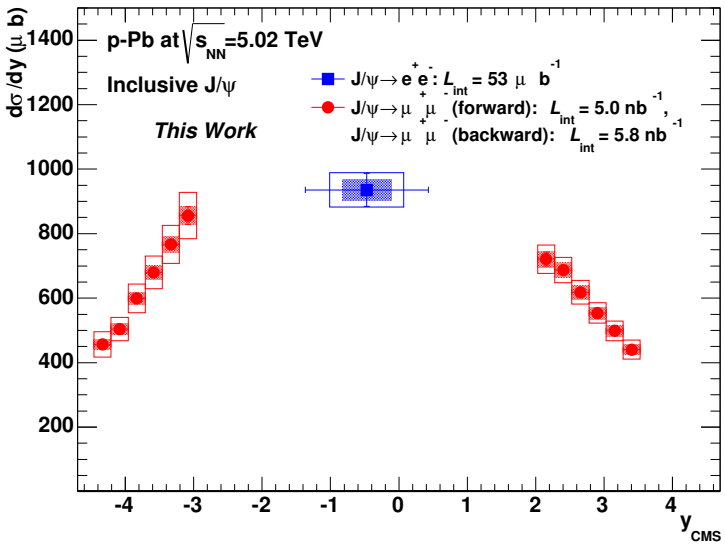

Figure 5.1: The inclusive J/ψ cross section as a function of y in p–Pb collisions at $\sqrt{s_{NN}} = 5.02$ TeV. The blue marker shows the results at mid-rapidity. The red markers show the measured cross sections via the dimuon decay channel in ALICE. The open boxes show the uncorrelated systematic uncertainty and the shaded boxes show the sum in quadrature of the partially and fully correlated systematic uncertainties.

the mean p_{T} of the inclusive J/ψ is calculated as 2.815 $\pm$ 0.095 (stat) $\pm$ 0.03 (syst) GeV/c. It is consistent with the interpolated mean p_{T} in pp collisions at the different collision energies in Table. 4.7.

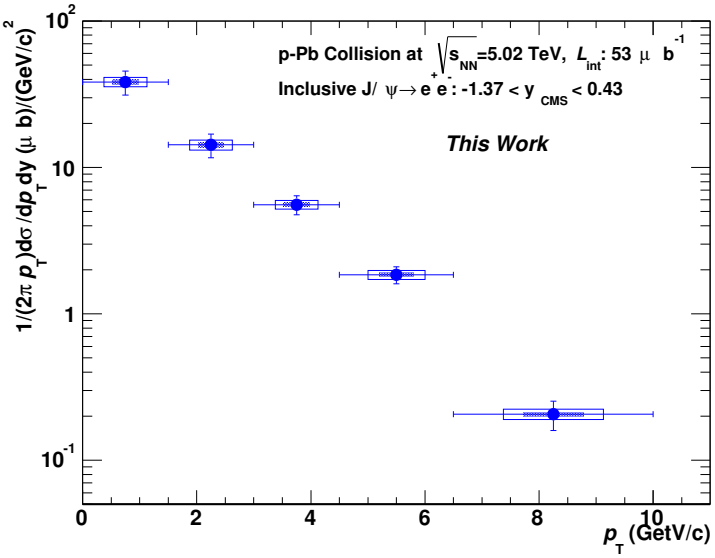

Figure 5.2: Invariant cross section as a function of p_{T} in p–Pb collisions at $\sqrt{s_{NN}} = 5.02$ TeV. The open square shows the uncorrelated systematic uncertainty and the shaded band shows the correlated systematic uncertainties.

p_{T} (GeV/c) bin	$d\sigma_{J/\psi}/dp_{\mathrm{T}}dy$ ± stat ± uncorr. syst ± corr.syst (μb)
0.0 – 1.5	154 ± 30 ± 11 ± 7
1.5 – 3.0	223 ± 40 ± 17 ± 10
3.0 – 4.5	162 ± 21 ± 11 ± 7.3
4.5 – 6.5	47 ± 7 ± 3 ± 2
6.5 – 10.0	7.0 ± 2.0 ± 0.6 ± 0.3

Table 5.1: Summary of the inclusive J/ψ cross section and their uncertainties in p–Pb collisions at $\sqrt{s_{NN}}$ =5.02 TeV.

5.1.2 R_{pPb} of Inclusive J/ψ production in p–Pb Collisions

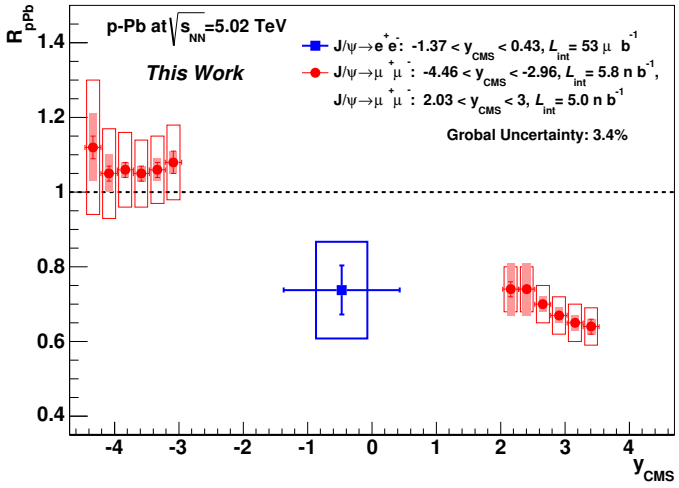

Figure 5.3: R_{pPb} as a function of y in p–Pb collisions at $\sqrt{s_{NN}}$ = 5.02 TeV.

The nuclear modification factor R_{pPb} is calculated based on Eq. 4.2, where interpolated pp spectrum as discussed in Section 4.9. Figure 5.3 shows the measured inclusive J/ψ R_{pPb} as a function of y at $\sqrt{s_{NN}}$ = 5.02 TeV. The inclusive J/ψ R_{pPb} at mid-rapidity ($-1.37 < y < 0.43$) is

$$R_{\mathrm{pPb}} = 0.74 \pm 0.07\ (\mathrm{stat}) \pm 0.13\ (\mathrm{uncorr.\ syst}) \pm 0.03\ (\mathrm{corr.\ syst}). \quad (5.2)$$

The latter 2 components are the uncorrelated and correlated systematic uncertainties with respect to those of the dimuon decay measurements, respectively. Significant suppression of the J/ψ yield is observed relative to the J/ψ yield in pp collisions. In the dimuon measurement, the partially correlated and the fully correlated systematic uncertainties are defined as follows:

- Partially correlated uncertainty: Interpolation of the rapidity differential pp reference cross section.

- Correlated uncertainty: Thickness function (T_{pPb}), Interpolation of the rapidity-integrated pp reference cross section at forward rapidity ($2.5 < y < 4$) from the measured data.

The integrated forward rapidity ($2.03 < y < 3.53$) and backward rapidity ($-4.46 < y < -2.96$) J/ψ $R_{\rm pPb}$ are 0.70 $\pm$ 0.01 (stat) $\pm$ 0.06 (uncorr. syst) $\pm$ 0.03 (part. corr. syst) $\pm$ 0.03 (corr. syst) and 1.08 $\pm$ 0.01 (stat) $\pm$ 0.09 (uncorr. syst) $\pm$ 0.03 (part. corr. syst) $\pm$ 0.04 (corr. syst), respectively. The mid-rapidity result shows the same magnitude of the suppression as the forward rapidity where gluon shadowing is expected to be stronger than mid-rapidity.

Figure 5.4 shows the inclusive J/ψ $R_{\rm pPb}$ as a function of $p_{\rm T}$ at mid-rapidity. The black box represents the global uncertainty, which is composed of the uncertainties from $T_{\rm pPb}$ and interpolated $d\sigma_{J/\psi}/y$ in pp collisions. The suppression at the level $\sim 2.4\sigma$ is seen at the low $p_{\rm T}$ bin ($p_{\rm T}$ = 1.5–3 GeV/c). Above 4.5 GeV/c, no modification is observed within the uncertainties. The values of the inclusive J/ψ $R_{\rm pPb}$ and the uncertainties are summarized in Table 5.2.

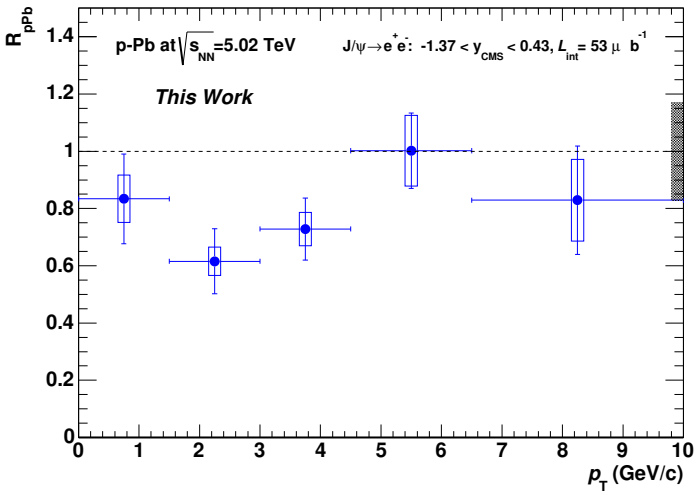

Figure 5.4: Inclusive J/ψ $R_{\rm pPb}$ as a function of $p_{\rm T}$ in p–Pb collisions at $\sqrt{s_{NN}}$ = 5.02 TeV.

$p_{\rm T}$ bin (GeV/c)	$R_{\rm pPb}$ $\pm$ stat $\pm$ uncorr. syst $\pm$ corr. syst
0.0 – 1.5	0.83 $\pm$ 0.15 $\pm$ 0.08 $\pm$ 0.14
1.5 – 3.0	0.62 $\pm$ 0.11 $\pm$ 0.05 $\pm$ 0.11
3.0 – 4.5	0.72 $\pm$ 0.11 $\pm$ 0.06 $\pm$ 0.13
4.5 – 6.5	1.00 $\pm$ 0.13 $\pm$ 0.12 $\pm$ 0.17
6.5 – 10.0	0.83 $\pm$ 0.18 $\pm$ 0.14 $\pm$ 0.14

Table 5.2: Summary of the inclusive J/ψ $R_{\rm pPb}$ and the uncertainties in p–Pb collisions at $\sqrt{s_{NN}}$ =5.02 TeV.

5.2 Discussion

5.2.1 Comparison with the Model Calculations

The results are compared to the several models including different nuclear matter effects such as gluon shadowing, coherent energy loss, and gluon saturation. The theoretical models discussed in this thesis are as follows:

NLO color evaporation model with EPS09 nPDF (EPS09 NLO) [118]
: This calculation includes the modification of the nPDF expected by EPS09 parametrization. The main uncertainty of EPS09 is the shadowing parametrization. Since Deep Inelastic Scatterings (DIS) do not probe directly to gluon PDF, nPDF parametrization in EPS09 uses the inclusive pion production in d–Au at RHIC [116]. However the EPS09 still has a sizable uncertainty at small and intermediate Q^2 as shown in Fig. 2.8. The J/ψ production from $c\bar{c}$ is described by the NLO color evaporation model (CEM) in this calculation.

Leading-order calculation with EPS09 nPDF (EPS09 LO) [119]
: This calculation includes the modification of the nPDF expected by EPS09 parametrization. This calculation is based on the $2 \to 2$ process like $g + g \to J/\psi + g$. The motivation of this calculation comes from the leading order calculation of the color singlet model (CSM) which predicts $2 \to 2$ process is dominant in low p_{T} J/ψ production. Relatively small absorption cross sections ($\sigma_{abs} = 1.5$ mb, 2.8 mb) are considered based on R_{dAu} of J/ψ at RHIC [73]. The result with the central set of the EPS09 LO calculation have the scale uncertainty as shown in Fig. 5.5.

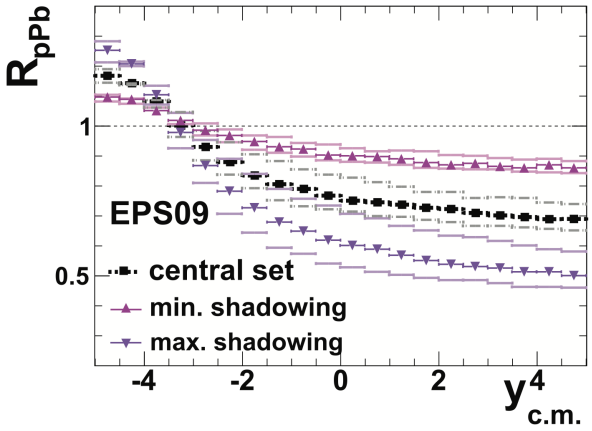

Figure 5.5: Scale uncertainty of the EPS09 LO calculation [119].

Parton energy loss in the normal nuclear matter [42]
: This calculation takes into account the coherent energy loss in nuclei. The detail of this calculation is described in Section 2.5.3. The transport coefficient includes the effect of the gluon density evolution with $\hat{q}(x) \sim \hat{q}_0(\frac{10^{-2}}{x})^{0.3}$. $\hat{q}_0$ is the only

parameter in this calculation. The calculations are performed with two sets of the $\hat{q}$ parametrization ($\hat{q}_0$ = 0.055 GeV^2/fm and 0.075 GeV^2/fm) in four nPDF assumptions (pp parametrization, DSSZ, EPS09, and Gluon Saturation) as shown in Fig. 2.11.

Color-Glass-Condensate (CGC) framework calculation [37, 121, 122]

At forward rapidity, calculations of J/ψ production are performed using CGC framework. In Ref [37], the nPDF is calculated with the Balitsky-Kovchegov (BK) equation including the running coupling corrections (rcBK equation). CEM is adopted in the J/ψ formation. The main systematic uncertainties of the calculation are the uncertainties of Q_s^2 and charm quark mass. Other calculations adopting CEM and NRQCD models are also performed in Refs. [121, 122].

Figure 5.6 shows the comparison of the y dependence of J/ψ $R_{\rm pPb}$ to those of the shadowing model calculations. At mid-rapidity, both of EPS09 NLO and EPS09 LO calculations are consistent with the data. Although EPS09 LO has a large scale uncertainty, it describes the y dependence of the data. Data with weak y dependence is qualitatively described by the shadowing model calculations.

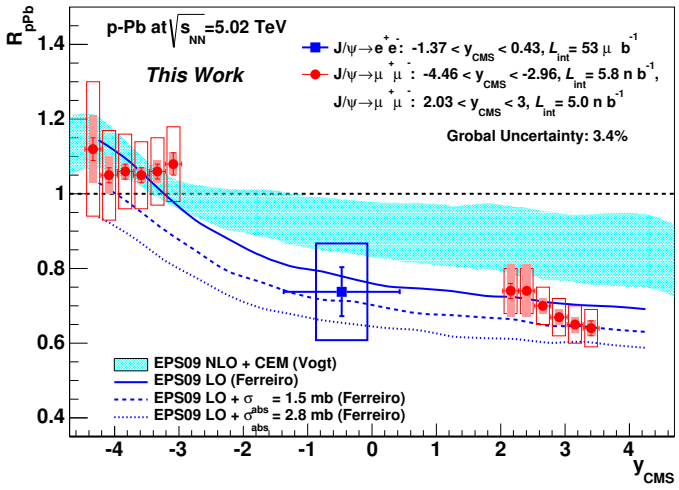

Figure 5.6: Comparison of the y dependence of J/ψ $R_{\rm pPb}$ with the shadowing model calculation of J/ψ $R_{\rm pPb}$ in p–Pb collisions at $\sqrt{s_{NN}}$ = 5.02 TeV [118, 119].

The recent calculation with the nCTEQ15 parametrization that is obtained by the global fit to the experimental data with the CTEQ PDF shows the similar x dependence of $R_g^{\rm Pb}$ compared to EPS09 as shown in Fig. 5.7 [123–125]. The weak x dependence of $R_g^{\rm Pb}$ at small x is qualitatively consistent with weak y dependence of $R_{\rm pPb}$ at mid-rapidity and forward rapidity. Because of stronger suppression of $R_g^{\rm Pb}$, J/ψ $R_{\rm pPb}$ calculations based on nCTEQ15 might give a better description of the experimental results than the EPS09 NLO calculation.

Under the assumption that the $2 \rightarrow 1$ ($g + g \rightarrow J/\psi$) process is dominant, the predictions of $R_{\rm pPb}$ based on the nPDF approaches are almost identical with $R_g^{\rm Pb}$ at

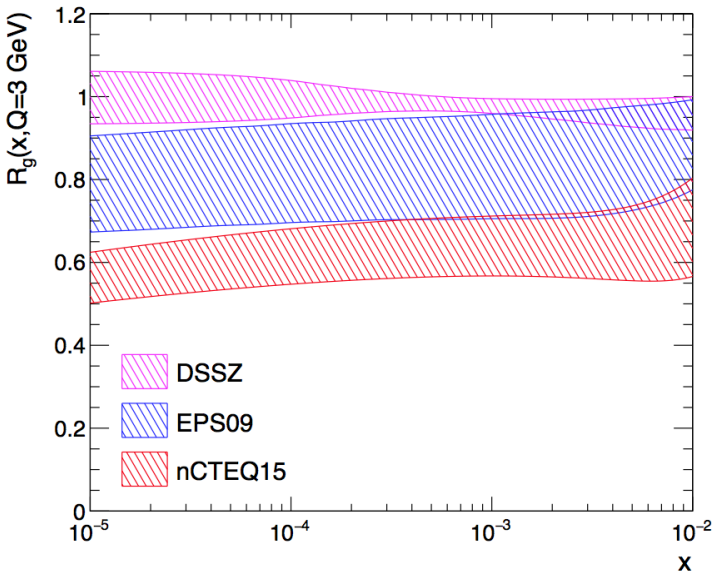

Figure 5.7: $R_g^{Pb}(x, Q = 3\mathrm{GeV})$ for DSSZ, EPS09, and nCTEQ15 nPDFs [125].

$x = \frac{\sqrt{\langle p_{\mathrm{T}}\rangle^2 + m^2_{J/\psi}}}{\sqrt{s}} e^{-y}$ and $Q = \sqrt{\langle p_{\mathrm{T}}\rangle^2 + m^2_{J/\psi}}$. The $2 \to 2$ case is also discussed in Ref. [120]. When we take the measured mean p_{T} described in Section 5.1.1, the expected R_g^{Pb} is $\sim 0.74 \pm 0.15$. The nuclear absorption in the EPS09 LO calculation suppress the yield by a factor 15% at $y \sim 0$. The coherent energy loss also expects to suppress the yield by a factor 20% even even if no modification of nPDF is assumed. Therefore, other normal nuclear matter effects expect that R_g^{Pb} is 0.87–0.92. Figure 5.8 shows the x coverage of the partons in Pb for the $2 \to 1$ process as a function of J/ψ p_T in p–Pb collisions and Pb–Pb collisions at LHC. Since the probing Q^2 is expressed as $p^2_{\mathrm{T},J/\psi} + m^2_{J/\psi}$, the mean Q^2 in the 0–1.5 GeV/c bin of J/ψ p_{T} is $\sim$ 10.1 GeV^2 and the expected R_g^{Pb} is 0.84 $\pm$ 0.22. It is compatible to the result of the EPS09 calculation at $Q^2 = 10$ GeV^2 in Fig. 2.8.

Figure 5.9 shows the comparison of the y dependence of J/ψ R_{pPb} to that of the coherent energy loss calculation [42]. The solid and dashed curves show the coherent energy loss calculations with the EPS09 nPDF and the proton PDF, respectively. Taking the shadowing parametrization leads to the decrease of the initial number of $c\bar{c}$ pairs compared to the case of proton PDF. The calculated results describe the y dependence of the data. In particular, the calculation without any gluon shadowing shows the better agreement with the data.

Figure 5.10 shows the comparison of the y dependence of J/ψ R_{pPb} with the CGC calculations [37, 121, 122]. The calculation with CEM introduces the impact parameter dependence of collisions and shows the better agreement with the data within 2σ. The CGC+NRQCD calculation shows the agreement with the data within the uncertainties.

Figure 5.11 shows the comparison of the p_{T} dependent R_{pPb} to EPS09 NLO at mid-rapidity. The measured R_{pPb} is consistent with EPS09 NLO model within the global uncertainty of the data. Figure 5.12 shows the comparison of the p_{T} dependence of J/ψ

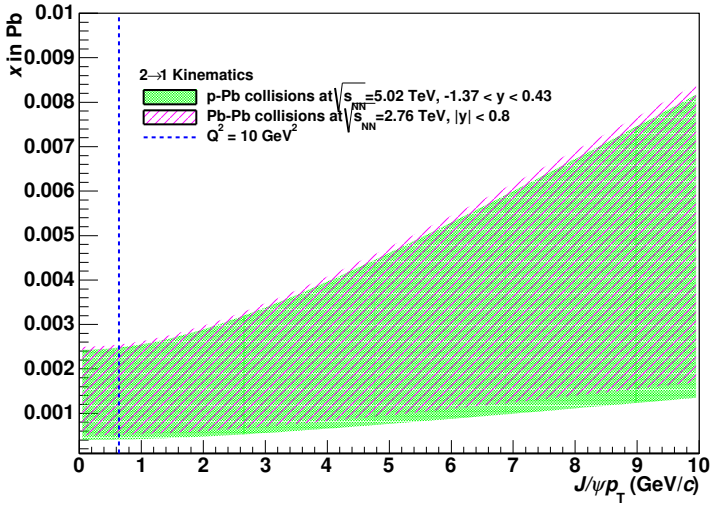

Figure 5.8: x coverage in Pb of the J/ψ measurement at mid-rapidity in p–Pb collision at $\sqrt{s_{NN}} = 5.02$ TeV and Pb–Pb collisions at $\sqrt{s_{NN}} = 2.76$ TeV in case of $2 \rightarrow 1$ kinematics.

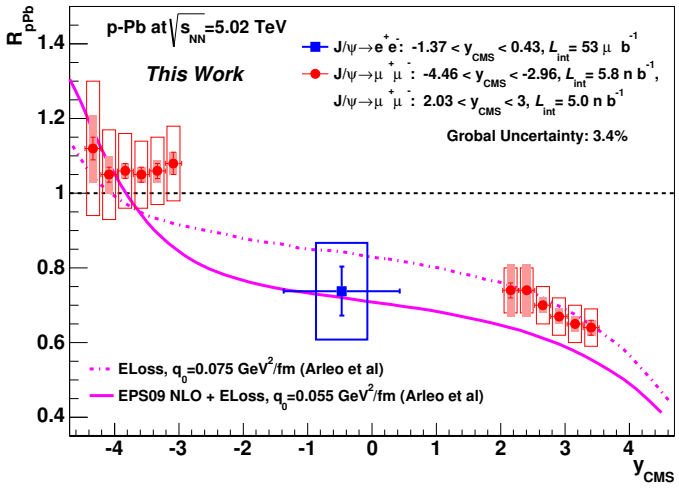

Figure 5.9: Comparison of the y dependence J/ψ R_{pPb} with the coherent energy loss calculation of J/ψ R_{pPb} in p–Pb collisions at $\sqrt{s_{NN}} = 5.02$ TeV [42].

R_{pPb} with the coherent energy loss model and the CGC frameworks. The coherent energy loss calculation shows the reasonable agreement with the data within the uncertainty.

As a summary of the model comparison to the data, the coherent energy loss model shows the reasonable description of the both of y and p_{T} dependence. R_g^{Pb} calculated with several nPDFs shows the weak x dependence at small x and it is qualitatively consistent with the rapidity dependence of the data. CGC calculations describe the data at forward J/ψ production. However the uncertainties are still large for both data and model calculation. The main sources of the uncertainties of the experimental data are the statistical uncertainty and the uncertainty of the interpolated pp reference spectra.

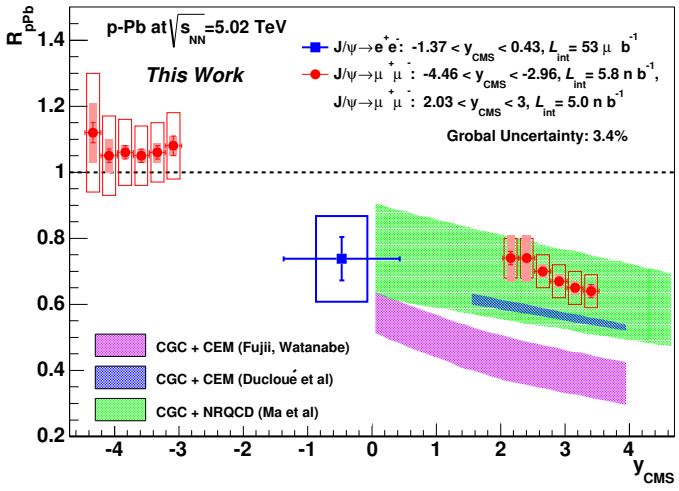

Figure 5.10: Comparison of the y dependence of J/ψ R_{pPb} with the CGC calculation of J/ψ R_{pPb} in p–Pb collisions at $\sqrt{s_{NN}} = 5.02$ TeV [37, 121, 122].

To achieve high precision, the reduction of these uncertainties are needed.

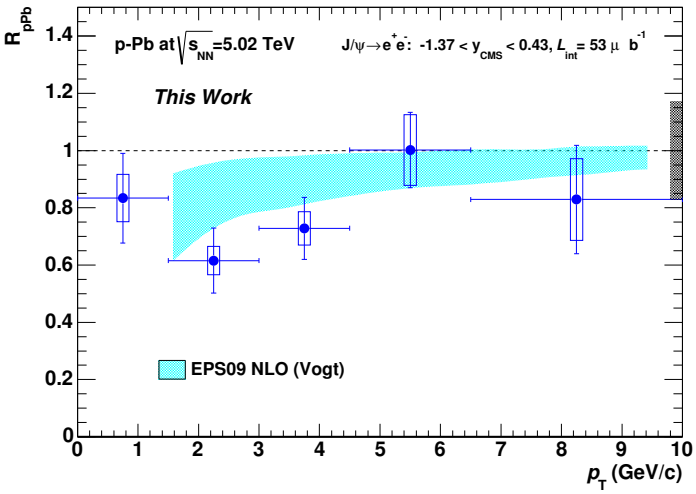

Figure 5.11: Comparison of the p_{T} dependence of the measured R_{pPb} to the color evaporation model with EPS09 nPDF in p–Pb collisions at $\sqrt{s_{NN}} = 5.02$ TeV.

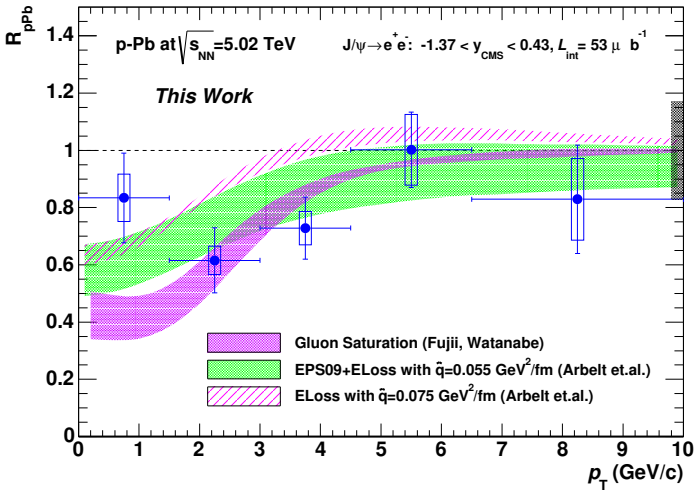

Figure 5.12: Comparison of the p_{T} dependence of J/ψ R_{pPb} and the model calculations in p–Pb collisions at $\sqrt{s_{NN}} = 5.02$ TeV. The red, green, and magenta bands show the calculation based on gluon saturation with CGC framework, coherent energy loss with EPS09 nPDF parametrization, and coherent energy loss with pp PDF parametrization.

5.2.2 Comparison to A–A collisions

J/ψ production in the initial parton-parton scattering ($gg \to J/\psi + X$) is denoted as

$$\sigma_{\mathrm{PbPb}\to \mathrm{J}/\psi \mathrm{X}} = \Sigma_{i,j,k_{cc}} f_i^{\mathrm{Pb}}(x_i) \ \times \ \sigma_{i+j\to k_{cc}} \ \times \ f_j^{\mathrm{Pb}}(x_j) \ \times \ \sigma_{k_{cc}\to J/\psi X}, \tag{5.3}$$

where f_i^{Pb} is the parton distribution function inside Pb and $\sigma_{i+j\to k_{cc}}$ is the c production cross section with the momentum transfer k_{cc}. $\sigma_{k_{cc}\to J/\psi X}$ is the J/ψ production cross section from $c\bar{c}$. To discuss normal nuclear matter effects in Pb–Pb collisions from the experimental results, we consider the following assumption,

- $2 \to 1$ process is dominant.

- The effect of nPDF modification is dominant.

In this case, the difference of the x coverage between p–Pb collisions at $\sqrt{s_{NN}} = 5.02$ TeV and Pb–Pb collisions at $\sqrt{s_{NN}} = 2.76$ TeV is only 6% as shown in Fig. 5.8. Since the R_g^{Pb} calculations with different nPDFs suggest the weak x dependence of R_g^{Pb} at small x ($x < 10^{-2}$), R_g^{Pb} for Pb–Pb collisions is similar to that for p–Pb collisions. To estimate the magnitude of initial normal nuclear matter effects in Pb–Pb collisions, R_{AA} due to normal nuclear matter effects is parametrized by using R_{pPb} as follows [120]:

$$R_{AA,\mathrm{init}} = \ R_{\mathrm{pPb}}(y, b_1) \times R_{\mathrm{pPb}}(-y, b_2), \tag{5.4}$$

where b_1 and b_2 is the impact parameters of incident nucleons with respect to target nuclei. The similar calculation in $2 \to 2$ process is discussed in Ref. [120]. It is noted that the y dependence of $R_{AA,\mathrm{init}}$ between the $2 \to 1$ and $2 \to 2$ calculations is different but two calculations give the same $R_{AA,\mathrm{init}}$ at the mid-rapidity region.

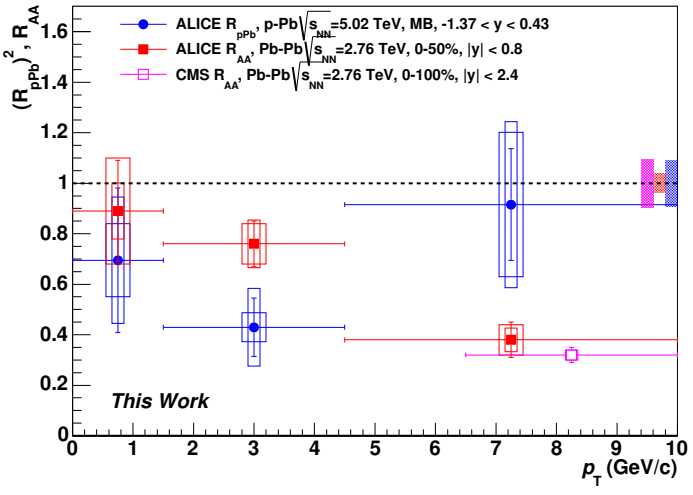

Figure 5.13: Comparison of R_{AA} and $(R_{\mathrm{pPb}})^2$ in ALICE. The data points of Pb–Pb collisions are take from [79].

Figure 5.13 shows the comparison of R_{AA} in 0–50% and 0–100% centrality with $R_{AA,\mathrm{init}}$ at mid-rapidity. The Pb–Pb data shows the stronger suppression with respect to J/ψ p_{T}.

The direct comparison to $(R_{\rm pPb})^2$ indicates two features of J/ψ production in Pb–Pb collisions. Since the clear suppression of the J/ψ yield above $p_{\rm T} > 4.5$ GeV/c in Pb–Pb collisions is seen compared to $R_{AA,\rm init}$, the suppression at high $p_{\rm T}$ in Pb–Pb collisions is thought as QGP effects. The second point is the significant enhancement of J/ψ R_{AA} at lower $p_{\rm T}$ in Pb–Pb collisions from $R_{AA,\rm init}$. According to model calculations, regeneration J/ψ is dominant below 5 GeV/c at mid-rapidity [77]. It is consistent with the enhancement of R_{AA} compared to $R_{AA,\rm init}$, As a next step, survival fraction S_{AA} is extracted as follows:

$$S_{AA} = \frac{R_{AA}}{R_{AA,\rm init}}. \tag{5.5}$$

Figure 5.14 shows J/ψ S_{AA} in Pb–Pb collisions at LHC. The measured values of S_{AA}

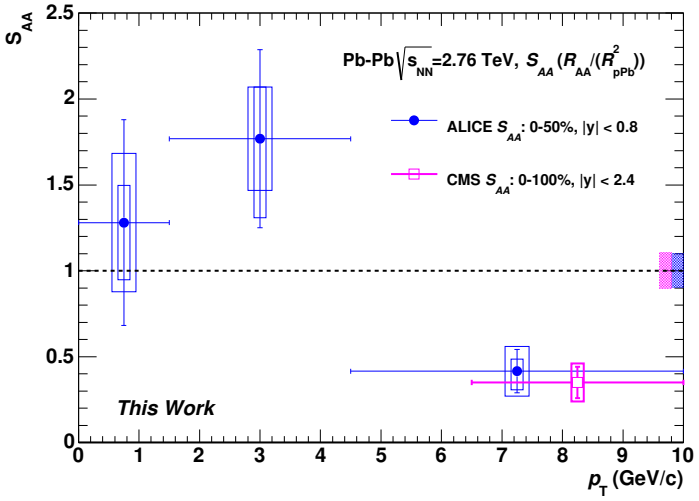

Figure 5.14: Survival fraction (S_{AA}) of J/ψ production in Pb–Pb collisions.

are 1.77 ± 0.52 (stat) ± 0.30 (uncorr. syst) $\pm^{0.45}_{0.30}$ (corr. syst) and 0.41 ± 0.12 (stat)± 0.14 (uncorr. syst) $\pm\,^{0.1}_{0.07}$ (corr. syst) at low $p_{\rm T}$ ($1.5 < p_{\rm T} < 4.5$ GeV/c) and high $p_{\rm T}$ ($4.5 < p_{\rm T} < 10$ GeV/c), respectively. The global uncertainties for both ALICE and CMS results are 10%. The values of S_{AA} are qualitatively consistent with the color screening of J/ψ at high $p_{\rm T}$ and regeneration of J/ψ at low $p_{\rm T}$.

Chapter 6

Conclusion

J/ψ suppression is one of the strong evidences for QGP formation in relativistic heavy ion collisions. Previous J/ψ measurements at RHIC show the strong suppression of J/ψ production in relativistic Au–Au collisions. Suppression of the J/ψ yield is also observed in Pb–Pb collisions at the LHC. The measured J/ψ $R_{\rm AA}$ is influenced not only by QGP effects but also by other nuclear matter effects such as gluon shadowing.

To investigate normal nuclear matter effects experimentally, inclusive J/ψ production was measured in p–Pb collisions at $\sqrt{s_{NN}} = 5.02$ TeV with the ALICE detectors in 2013. J/ψ yields were measured via the dielectron decay channel in the mid-rapidity region $-1.37 < y < 0.43$. Electrons are reconstructed using information of ITS and TPC in the ALICE central barrel.

The production cross section of inclusive J/ψ in p–Pb collisions at $\sqrt{s_{NN}} = 5.02$ TeV is determined by

$$\frac{d\sigma_{J/\psi}}{dy} = 930 \ \pm 83 \ (\text{stat}) \ \pm \ 59 \ (\text{uncorr. syst}) \ \pm \ 45(\text{corr. syst}) \ \mu\text{b}. \tag{6.1}$$

The nuclear modification factor in p–Pb collisions ($R_{\rm pPb}$) is extracted by dividing the J/ψ spectrum in p–Pb collisions by the interpolated pp spectrum. The inclusive J/ψ $R_{\rm pPb}$ at mid-rapidity is extracted as

$$R_{\rm pPb} = 0.74 \ \pm \ 0.07 \ (\text{stat}) \ \pm \ 0.13 \ (\text{uncorr. syst}) \ \pm \ 0.03 \ (\text{corr. syst}). \tag{6.2}$$

Non-negligible suppression was observed. Compared with the forward rapidity measurement via the dimuon decay channel, the magnitude of $R_{\rm pPb}$ at mid-rapidity is compatible within the uncertainties.

Several models including modification of nPDFs, coherent energy loss, and gluon saturation with CGC frameworks are compared to the measured J/ψ $R_{\rm pPb}$. The coherent energy loss model describes both the y and $p_{\rm T}$ dependence of the data within the uncertainties. Weak rapidity dependence of $R_{\rm pPb}$ is explained by fact that $R_g^{\rm Pb}$ from the shadowing model calculations show weak x dependence at small x. The expected R_g^{Pb} from measured $R_{\rm pPb}$ is compatible with the values calculated with EPS09 shadowing parametrization within the uncertainty. CGC calculations describe the data at forward J/ψ production. However, the uncertainty is still large for both data and model calculations to obtain the conclusive explanation of normal nuclear matter effects in p–Pb

collisions at the LHC. The main sources of the uncertainties of the experimental results are the statistical uncertainty and the uncertainty of the interpolated pp reference spectra.

Under simple assumptions, we approximated the nuclear modification factor from the normal nuclear matter effects as the convolution of R_{pPb}. Compared between $(R_{\mathrm{pPb}})^2$ at $\sqrt{s_{NN}} = 5.02$ TeV and R_{AA} in Pb–Pb collisions at $\sqrt{s_{NN}} = 2.76$ TeV, the suppression is seen at high p_T above 4.5 GeV/c. This suppression is qualitatively consistent with the color screening pictures. On the other hand, the enhancement of the J/ψ yield is observed at lower p_{T}, which is due to the regeneration of J/ψ in Pb–Pb collisions

Run2 of LHC started in 2015 and it gives us the opportunity to investigate new collision energies in pp collisions at $\sqrt{s} = 13$, 14 TeV, p–Pb collisions at $\sqrt{s_{NN}} = 8$ TeV, and Pb–Pb collisions at $\sqrt{s_{NN}} = 5.02$ TeV with improved statistics. Furthermore, data taking of pp collisions at $\sqrt{s} = 5.02$ TeV is also scheduled as the reference measurement of p–Pb and Pb–Pb. These data will reduce the systematic uncertainties in R_{pPb} measurements, which is crucial for quantitative understanding of J/ψ production in relativistic heavy ion collisions.

Acknowledgement

First of all, I have to express my gratitude to my supervisor, Prof. Hideki Hamagaki, for his appropriate advice and profound comments on my analysis and physics. His rich knowledge and entire support guided me to the completion of this thesis. I am deeply grateful to my supervisor, Prof. Kentaro Yako for his great support in the last year of my Ph.D. I would like to acknowledge Dr. Taku Gunji for his wealth of knowledge about physics and analysis techniques. His words are strict, instructive and then kind. Without his guidance and strong encouragement, this thesis wouldn't have been possible. I could not have wished for better supervisors.

I wish to thank Prof. Ken Oyama for his great help and support on TRD work at CERN. His keen insight and great knowledge provided me a lot of lessons of the accomplishment of research.

I would like to express my appreciations to Dr. Yorito Yamaguchi and Dr. Yosuke Watanabe for many wonderful discussions and brilliant and empathic advice. Discussions with them have been illuminating. I thank Dr. Yoki Aramaki, Dr. Satoshi Sano, Dr. Akihisa Takahara, Dr. Yasuto Hori, and Dr. Ryoji Akimoto for providing various knowledge and interesting discussions. I was blessed with superb seniors during my Ph.D. Thank you to Mr. Tomoya Tsuji, Mr. Atsushi Nukariya, Ms. Yuko Sekiguchi, Mr. Kohei Terasaki, Mr. Kentaro Yukawa and, Ms. Hikari Murakami for their suggestions, encouragement, and warm friendship. I'm very happy to spent a lot of time with you in my master and Ph.D courses. Chatting with you always made me laugh and it is very important and necessary for a change.

I thank Prof. Hideto En'yo and RIKEN Rad. Lab. Group for their great help. They also supported me financially and it was essential to continue the work. I would like to thank Dr. Sanshiro. Mizuno for his friendships and many discussions as my contemporary of Ph.D.

I thank Prof. Johhana Stachel and the members of ALICE TRD group for giving an amazing opportunity of the excellent work. I had a valuable experience and absorbed many skills on high energy experiments with their great help. In particular, I really appreciate Dr. Jochen Klein, Dr. Yvonne Patchmayer, Dr. Chilo. G. Cuadrado, and Dr. Michael Winn for their great knowledge and help. The friendship of Dr. Jorge Mercado and Dr. Goran Simatovic is my treasure.

I wish to thank PWGDQ people for many discussion and suggestive advice of the dielectron analysis. They are very helpful of me to summarize the thesis.

I thank all members of ALICE-J group for many discussion and kind supports. I never forget the wonderful experience and journey in my CERN life with Mr. Satoshi Yano and Dr. Daisuke Watanabe.

I appreciate the members of the Center for Nuclear Study, University of Tokyo for their generous support and kindness, especially I cannot thank enough to the CNS secretaries, Ms. Midori Hirano, Ms. Takako Endo, Ms. Ikuko Yamamoto, Ms. Yuko Soma, Ms. Yukino Kishi, Mr. Hiroshi Yoshimura, and Mr. Mikio Oki.

I am much obliged to Prof. Hiroaki Miyatake, Prof. Akira Ejiri, Prof. Kenji Fukushima, Prof. Ryugo Hayano, Prof. Nobuaki Imai and for their valuable comments and important advice. I would like to express my appreciation to Prof. Hiroaki Miyatake for his truly relevant advice and proof-readings.

I thank Mr. Jion Suzuki and Dr. Tomoko Kuwahara for their great help in proofreading of this thesis.

Finally, my warmest thanks go to my parents Kazuya and Naoko, my sisters Misako and Mayumi and the rest of my family for their deep love, understanding, and support.

Appendix A

Collision Geometry in Relativistic Heavy Ion Collisions

Figure A.1 shows the schematic view of the high energy nucleus-nucleus collisions with the impact parameter b. The geometrical features of the nucleus-nucleus collisions are described by the Glauber model calculation [115]. It is widely used to obtain the variables such as N_{part}, N_{coll}, path length L, and the nuclear thickness function $T_{\rm AA}$.

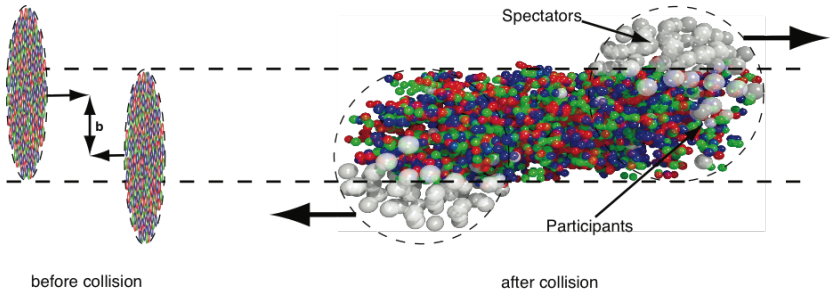

Figure A.1: Schematic view of the high energy nucleus-nucleus collisions. The figure is taken from [127].

A.1 Glauber Model

In the Glauber model calculation, the density distribution of heavy nuclei is considered by the Woods-Saxon form expressed as

$$\rho(r) = \frac{\rho_0}{1 + e^{(r-R)/d}} \tag{A.1}$$

where R is the radius of nucleus, d is called as the skin depth.

The basic Glauber model requires the following assumption,

- Nucleons travel to the straight lines.

- Binary nucleon-nucleon collisions are independent each other.

- The inelastic cross section of nucleon-nucleon collisions is same as that in vacuum.

If we consider the relativistic nucleus-nucleus collisions between A and B with the impact parameter b, the participants and the spectators can be defined. The participants are nucleons which exist in the overlap region of A and B. The spectators are defined as the nucleons outside the overlap region of A and B.

The probability at the transverse position s in A is

$$T_A(s) = \int \rho_A(s, z_A) dz_A \tag{A.2}$$

By integrating over the joint probability in small unit d^s is $T_A(s)T_B(s-b)$, the effective overlap region is obtained,

$$T_{AB}(b) = \int T_A(s)T_B(s-b)ds^2. \tag{A.3}$$

$T_{AB}(b)$ is defined as the thickness function. The probability of occurance of a nucleon-nucleon collision between A and B is expressed by

$$T_{AB}(b)\sigma_{NN} = \int db_A dz_A \rho_A(b_A, z_A) db_B dz_B \rho_B(b_B, z_B) t(b - b_A - b_B)\sigma_{NN}, \tag{A.4}$$

where $t(b)$ is the probability of a nucleon-nucleon collision within the transverse element db.

The probability of having n nucleon-nucleon collisions can be described by the binominal distribution,

$$P(n, b) =_{AB} C_n[T_{AB}(b)\sigma_{NN}]^n[1 - T_{AB}(b\sigma_{NN})]^{AB-n} \tag{A.5}$$

Therefore the number of nucleon-nucleon collision (N_{coll}) is obtained by

$$N_{coll}(b) = \langle n(b) \rangle = \Sigma_{n=1}^{AB} nP(n, b) = ABT_{AB}(b)\sigma_{NN} \tag{A.6}$$

The number of participants is expressed by,

$$N_{part}(b) = A \int T_A(s)\{1 - [1 - T_B(s-b)\sigma_{NN}]^B\}ds^2 + B \int T_B(s)\{1 - [1 - T_A(s)\sigma_{NN}]^A\}ds^2 \tag{A.7}$$

Appendix B

Cut Index for the Cut Optimization of TPC PID and SPD Hit Requirement

Cut index	leg p_T(GeV/c)	SPD hit	TPC nσ_{pion}	TPC nσ_{proton}
0	0.8	Any	2.5	3
1	1.0	Any	2.5	3
2	1.1	Any	2.5	3
3	0.8	First	2.5	3
4	1.0	First	2.5	3
5	1.1	First	2.5	3
6	0.8	Any	3	3
7	1.0	Any	3	3
8	1.1	Any	3	3
9	0.8	First	3	3
10	1.0	First	3	3
11	1.1	First	3	3
12	0.8	Any	3.5	3
13	1.0	Any	3.5	3
14	1.1	Any	3.5	3
15	0.8	First	3.5	3
16	1.0	First	3.5	3
17	1.1	First	3.5	3
18	0.8	Any	4	3
19	1.0	Any	4	3
20	1.1	Any	4	3
21	0.8	First	4	3
22	1.0	First	4	3
23	1.1	First	4	3
24	0.8	Any	2.5	3.5
25	1.0	Any	2.5	3.5
26	1.1	Any	2.5	3.5
27	0.8	First	2.5	3.5
28	1.0	First	2.5	3.5
29	1.1	First	2.5	3.5
30	0.8	Any	3	3.5
31	1.0	Any	3	3.5
32	1.1	Any	3	3.5
33	0.8	First	3	3.5
34	1.0	First	3	3.5
35	1.1	First	3	3.5
36	0.8	Any	3.5	3.5
37	1.0	Any	3.5	3.5
38	1.1	Any	3.5	3.5
39	0.8	First	3.5	3.5
40	1.0	First	3.5	3.5
41	1.1	First	3.5	3.5
42	0.8	Any	4	3.5
43	1.0	Any	4	3.5
44	1.1	Any	4	3.5
45	0.8	First	4	3.5
46	1.0	First	4	3.5
47	1.1	First	4	3.5
48	0.8	Any	2.5	4
49	1.0	Any	2.5	4
50	1.1	Any	2.5	4
51	0.8	First	2.5	4
52	1.0	First	2.5	4
53	1.1	First	2.5	4
54	0.8	Any	3	4
55	1.0	Any	3	4
56	1.1	Any	3	4
57	0.8	First	3	4
58	1.0	First	3	4
59	1.1	First	3	4
60	0.8	Any	3.5	4
61	1.0	Any	3.5	4
62	1.1	Any	3.5	4
63	0.8	First	3.5	4
64	1.0	First	3.5	4
65	1.1	First	3.5	4
66	0.8	Any	4	4
67	1.0	Any	4	4
68	1.1	Any	4	4
69	0.8	First	4	4
70	1.0	First	4	4
71	1.1	First	4	4

Table B.1: Cut index for the cut optimization.

Bibliography

[1] Particle Data Group Collaboration, K. A. Olive *et al*, Chin. Phys. C 38 090001 (and 2015 update).

[2] Y. Aoki, *et al*. Nature 443 675 [hep-lat/0611014] (2006).

[3] Hot QCD Collaboration, Phys. Rev. D 90 094503, arXiv:1407.6387 (2014).

[4] K. Aamodt *et al*, ALICE Collaboration, Phys. Rev. C 94 034903 (2016).

[5] Michael Kliemant *et al*, Lect. Notes Phys. 785 23-103, arXiv:0809.2482 (2010).

[6] T. Lappi and L. McLerran, Nucl. Phys. A 772 200 (2006), arXiv:hep-ph/0602189.

[7] C. Shen *et al*, Phys. Rev. C 84 044903 (2011).

[8] PHENIX Collaboration, A. Adare *et al*, Phys. Rev. Lett. 98 232301 (2007).

[9] J.J. Aubert *et al*, Phys. Rev. Lett. 33 1404 (1974).

[10] J. E. Augusti *et al*, Phys. Rev. Lett 33 1406 (1974).

[11] E. Norrbin, T. Sjostrand Eur, Phys. J. C 17 137-161 (2000).

[12] C.H. Chang, Nucl. Phys. B 172 425 (1980).

[13] E.L. Berger *et al*, Phys. Rev. D 23 1521 (1981).

[14] H. Fritzsch, Phys. Lett. B 67 217 (1977).

[15] M. Glc *et al*, Phys. Rev. D , 2324 (1978).

[16] T. Matsui and H. Satz, Phys. Lett. B 178 416 (1986).

[17] P. Petreczky, J. Phys. G 37 094009, arXiv:1001.5284 (2010), arXiv:0906.0502 (2009).

[18] P. Bicudo, Phys. Rev. D 82 034507 (2010).

[19] H. Satz, J. Phys. G 32 R25 (2006).

[20] P. Braun-Munzinger and J. Stachel, Nature, 448 302–309 (2007).

[21] M. Bedjidian *et al*, hep-ph/0311048 (CERN yellow rpt).

[22] E. Perez and E. Rezvi, Rep. Prog. Phys. 76 046201, arXiv:1208.1178 (2013).

[23] H1 and ZEUS Collaboration, JHEP 1001:109 (2010), arXiv:0911.0884 (2010), H1 Collaboration, Eur. Phys. J. C 64 561-587 (2009).

[24] L. N. Lipatov, J. Nucl. Phys. 23 338 (1976), E. A. Kuraev *et al*, Zh. Eksp. Teor. Fiz 72, 3 (1977), Ya. Ya. Balitsky *et al*, Sov. J. Nucl. Phys. 28 (1978) 822.

[25] L. D. McLerran and R. Venugopalan, Phys. Rev. D 49 2233 (1994), Edmond Iancu, Andrei Leonidov, Larry McLerran, arXiv:hep-ph/0202270 (2002).

[26] L. Gribov *et al*, Phys. Rept. 1001 (1983).

[27] A.M. Stasto *et al*, Phys. Rev. Ltt. .68.596(2001).

[28] D. N. Triantafyllopoulos, Nucl. Phys. B 648 293 (2003).

[29] F. Gelis Phys. Lett. B 647 376 (2007).

[30] J.J. Aubert *et al*, Phys. Lett. B 31, 275 (1983).

[31] D. de Florian *et al*, Phys. Rev. D 69 074028 (2004).

[32] H. Paukkunen, J. Nucl. Phys A 04 001, arXiv:1401.2345 (2014).

[33] ALICE Collaboration, J. Phys. G: Nucl. Part. Phys. 32 1295 (2004).

[34] M. Hirai *et al*, Phys. Rev. C 76 065207, arXiv:0709.3038 (2007).

[35] K. J. Eskola *et al*, JHEP 0904 065, arXiv:0902.4154 (2009).

[36] D. de Florian, *et al*, Phys. Rev. D 85 074028, arXiv:1112.6324 (2012).

[37] H. Fujii and K. Watanabe, J. Nucl. Phys. A. 2013 06 011, arXiv:1304.2221 (2013).

[38] J. W. Cronin et al. Phys. Rev. D 11 3105 (1975).

[39] ALICE Collaboration, Phys. Lett. B 760 720, arXiv:1601.03658 (2016).

[40] S. Peigné *et al*, Phys. Rev. D 93 014006 (2016).

[41] F.Arleo *et al*, Phys. Rev. Lett. 109 122301, arXiv:1204.4609 (2012).

[42] F. Arleo *et al*, JHEP03 122, JHEP05 155, arXiv:1212.0434 (2013).

[43] FNAL E866/NuSea collaboration, M. Leitch *et al*, Phys. Rev. Lett. 84 3256 (2000).

[44] D. McGlinchey, Phys. Rev. C 87, 054910 (2013).

[45] C. Baglin, *et al*, Phys. Lett. B 255 459 (1991).

[46] C. Baglin, *et al*, Phys. Lett. B 262 362 (1991).

[47] C. Baglin, *et al*, Phys. Lett. B 268 453 (1991).

[48] C. Baglin, *et al*, Phys. Lett. B 345 617 (1995).

[49] M. C. Abreu *et al*, Phys. Lett. B 444 516 (1998).

[50] C. Baglin, *et al*, Phys. Lett. B 220 471 (1989).

[51] C. Baglin, *et al*, Phys. Lett. B 251 465 (1990).

[52] M. C. Abreu *et al*, Phys. Lett. B 423 207 (1998).

[53] M. C. Abreu *et al*, Phys. Lett. B 449 128 (1999).

[54] M. C. Abreu *et al*, Phys. Lett. B 466 408 (1999).

[55] B. Alessandro *et al*, Eur. Phys. J. C 33 31 (2004).

[56] B. Alessandro *et al*, Eur. Phys. J. C 48 329 (2006).

[57] M. C. Abreu *et al*, Phys. Lett. B 410 327 (1997).

[58] M. C. Abreu *et al*, Phys. Lett. B 410 337 (1997).

[59] M. C. Abreu *et al*, Phys. Lett. B 450 456 (1999).

[60] M. C. Abreu *et al*, Phys. Lett. B 521 195 (2001).

[61] M. C. Abreu *et al*, Phys. Lett. B 499 85 (2001).

[62] B. Alessandro *et al*., Eur. Phys. J. C 39 335 (2005).

[63] B. Alessandro *et al*, Eur. Phys. J. C 49 559 (2007).

[64] R. Arnaldi *et al*, Phys. Rev. Lett. 99 132302 (2007).

[65] B. Alessandro *et al*, Eur. Phys. J. C 49 559 (2007).

[66] R. Arnaldi *et al*, Phys. Rev. Lett. 99 132302 (2007).

[67] B. Alessandro *et al*., Eur. Phys. J. C 48 329 (2006).

[68] M. C. Abreu *et al*, Phys. Lett. B 499 85 (2001).

[69] A. Adare *et al*, Phys. Rev. Lett. 107 142301 (2011).

[70] A. Adare *et al*, Phys. Rev. C 87 034904 (2013), arXiv:1204.0777 (2013).

[71] A. Adare *et al*, Phys. Rev. C 84 054912 (2011).

[72] M. J Leitch *et al*, Phys. Rev. C 76 051901 (2007).

[73] R. Vogt, Acta Phys. Hung. A 25 97-103 (2006).

[74] N. Brambilla *et al*, Eur. Phys. J. C 71 1534, arXiv:1010.5827 (2011).

[75] R. Vogt, Phys. Rev. C 81 044903, arXiv:1003.3497 (2010).

[76] T. Gunji, Phys. Rev. C 76 051901 (2007).

[77] A. Andronic *et al*, Phys. Lett. B 652 259–261 (2007).

[78] ALICE Collaboration, Phys. Lett. B 734 314-327 (2014).

[79] ALICE Collaboration, JHEP07 051, arXiv:1504.07151 (2015).

[80] Zhou *et al*, PRC89 054911 (2014), Zhao *et al*, Nucl. Phys. A 859 114 (2011).

[81] A. Andronic, J. Nucl. Phys. A 10 009, arXiv:1409.5778 (2014).

[82] CMS Collaboration, JHEP05 063, arXiv:1201.5069 (2012).

[83] ALICE Collaboration, J. Phys. G: Nucl. Part. Phys. 30 1517 (2004).

[84] ALICE Collaboration, arXiv:1402.4476 (2014).

[85] The CERN accelerator complex, URL http://cds.cern.ch/record/2119882.

[86] ALICE Collaboration, Phys. Rev. C 91 6, 064905, arXiv:1412.6828 (2015).

[87] R. Glauber, ed WE Brittin and LG Dunham 1 315 (1959).

[88] R. Glauber, Phys. Rev. 100 242 (1955).

[89] R. Glauber, Nucl. Phys. A 774 3 (2006).

[90] A. Shor and R. Longacre, Phys. Lett. B 218 100 (1989).

[91] ALICE Collaboration, ALICE ITS Technical Design Report (2000).

[92] ALICE Collaboration, arXiv: 0911.5430 (2009).

[93] ALICE Collaboration, ALICE TPC Technical Design Report (2000).

[94] ALICE Collaboration, ALICE TRD Technical Design Report (2001).

[95] H. K. Soltveit *et al*, Nucl. Instrum. Meth. A 676 106–119 (2012).

[96] ALICE Collaboration, ALICE TOF Technical Design Report (2000).

[97] K. Aamodt *et al*, JINST, 3 S08002, (2008).

[98] J. Alme *et al*, Nucl. Instrum. Meth. A 622 316-367, arXiv:1001.1950 (2010).

[99] Track reconstruction principle in ALICE for LHC runI and runII, URL http://cds.cern.ch/record/1984041.

[100] Ashton, M. Humphries *et al*, Timing, Trigger and Control Systems for LHC Detectors, Status Report on the RD-12 Project, CERN/LHCC 97-29, 1997 (2000). Timing Trigger and Control Systems (TTC) for LHC URL http://ttc.web.cern.ch/TTC/.

[101] ALICE Central Trigger Processor, URL http://epweb2.ph.bham.ac.uk/user/krivda/alice/.

[102] ALICE Central Trigger Processor Preliminary Design Review, URL http://epweb2.ph.bham.ac.uk/user/krivda/alice/.

[103] J. Klein for the ALICE Collaboration, arXiv:1112.5110 (2011).

[104] ALICE Collaboration, Phys. Rev. Lett. 110 082302 (2013).

[105] B. Abelev *et al*, ALICE Collaboration, Phys. Rev. Lett. 110 032301 (2013).

[106] W. Blum and L. Rolandi, Particle Detection with Drift Chambers. Springer, Berlin, 1998.

[107] S. Roesler, arXiv:hep-ph/0012252 (2000).

[108] T. Sjostrand *et al*, JHEP 0605 026 (2006).

[109] P. Skands, Phys. Rev. D 82 074018 (2010).

[110] X.-N. Wang and M. Gyulassy, Phys. Rev. D 44 3501 (1991).

[111] R. Brun *et al*, GEANT: Detector Description and Simulation Tool; Oct 1994, CERN Program Library, CERN, URL https://cds.cern.ch/record/1082634.

[112] F. Bossu *et al*, arXiv:1103.2394 (2011).

[113] The ALICE Collaboration, JINST 9 1100 (2014).

[114] ALICE Collaboration, JHEP 02 073, arXiv:1308.6726 (2014).

[115] M. Miller *et al*, Annurev. Nucl. 57. 090506. 123020, arXiv:nucl-ex/0701025 (2007).

[116] B. I. Abelev *et al*, STAR Collaboration, Phys. Rev. C 81 064904, arXiv:0912.3838 (2010).

[117] S. S. Adler *et al*, PHENIX Collaboration, Phys. Rev. Lett. 98 172302 (2007).

[118] R. Vogt, Phys. Rev. C 81 044903 (2010).

[119] E. Ferreiro *et al*, Phys. Rev. C 88 4 047901 (2013).

[120] E. Ferreiro, *et al*, Phys. Lett. B680 50-55(2009).

[121] B. Ducloé *et al*, Phys. Rev. D 1 11400 5 (2015).

[122] Y. Q. Ma *et al*, Phys. Rev. D 92 071901 (2015).

[123] K. Kovarik *et al*, Phys. Rev. D 93 085037, arXiv:1509.00792 (2016).

[124] P. M. Nadolsky *et al*, Phys. Rev. D 78 013004 (2008).

[125] F. Arleo *et al*, arXiv:1512.01794 (2015).

[126] K. Aamodt *et al*, ALICE Collaboration, Phys. Rev. Lett. 106, 032301 (2011).

[127] R. Snellings, New J. Phys.13 055008, arXiv:1102.3010 (2011).